

UNIVERSITY OF KENT

**Designing High-Spin Organic Radicals for Spintronics: A  
Computational Exploration of Substituent and Structural  
Effects in Blatter Tri-Radicals**

by

**Jacob Sands**

A thesis submitted in partial fulfilment for the  
degree of Master of Science

in the  
School of Natural Sciences

**May 2025**

*I dedicate this thesis to my  
Godfather who recently passed away*

# Table of Contents

<b>Declaration of Authorship</b> .....	iv
<b>Acknowledgements</b> .....	v
<b>Abstract</b> .....	vi
<b>Abbreviations</b> .....	vii
<b>List of Figures</b> .....	ix
<b>List of Equations</b> .....	xiv
<b>1. Introduction</b> .....	1
1.1 Background Theory of Spintronics .....	1
1.1.1 Introduction to Spintronics .....	1
1.1.2 Principles of Spintronics in Electronic Devices .....	5
1.2 Organic Radicals in Spintronics .....	8
1.2.1 Overview of Organic Spintronics .....	8
1.2.2 Role of Organic Molecules in Spintronics .....	10
1.2.3 Characteristics of Polyradicals in Organic Spintronics .....	11
1.3 Blatter-Type Radicals .....	13
1.3.1 Definition and Structure of Blatter-Type Tri-Radicals .....	13
1.3.2 Stability and Electronic Properties of Blatter-Type Tri-Radicals .....	21
1.3.3 Magnetism and Spin Properties of Blatter-Type Tri-Radicals .....	22
1.4 Significance of Blatter-Type Tri-Radicals in Spintronics .....	23
1.4.1 Potential Applications in Spintronics .....	23
1.4.2 Advantages Over Conventional Spin Carriers .....	27
1.4.3 Additional Systems Relevant to this Thesis .....	28
1.5 Relevant Computational Work .....	29
1.6 Objectives of the Thesis .....	30
<b>2. Theoretical Framework and Methodology</b> .....	32
2.1 Density Functional Theory (DFT) Calculations .....	32
2.1.1 Fundamentals of Density Functional Theory .....	32
2.1.2 The Gaussian 16 Software .....	44
2.2 Post-Hartree–Fock Calculations .....	45
2.2.1 Fundamentals of Post-Hartree–Fock Methods .....	45
2.2.2 Complete Active Space Self-Consistent Field (CASSCF) Calculations .....	48
2.2.3 The Orca 5 Software .....	50
2.3 Computational Details .....	51
2.3.1 Selection of Molecules .....	53
2.3.2 Selection of Functionals .....	54

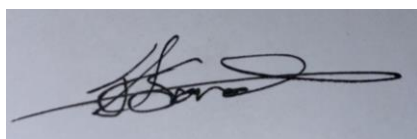
2.3.3 Basis Sets .....	56
2.3.4 Custom Basis Sets for Selenium and Sulphur Systems .....	57
2.3.5 Inclusion of Empirical Dispersion .....	57
2.3.6 Spin Contamination .....	58
2.3.7 Criteria for Geometry Benchmarking .....	59
<b>3. Results and Discussion.....</b>	<b>61</b>
3.1 Blatter Tri-Radicals: Structural Analysis .....	62
3.1.1 Structural Benchmark.....	62
3.1.2 Structural Analysis of Outer-Substituted Systems .....	64
3.1.3 Structural Analysis of the Inner-Substituted Systems.....	70
3.1.4 Outer EDG/EWGs.....	75
3.1.5 Inner EWG/EDGs .....	77
3.2 Blatter Tri-Radicals: Doublet-Quartet Gaps .....	80
3.2.1 Benchmark of D–G gaps.....	80
3.2.1 D–Q Gaps of Outer-Substituted Systems.....	83
3.2.2 D–Q Gaps of Inner-Substituted Systems .....	89
3.3 Energy Gaps in Additional Systems.....	94
<b>4. Conclusions and Future Work .....</b>	<b>98</b>
<b>5. References.....</b>	<b>103</b>

## Declaration of Authorship

I, Jacob Sands, declare that this thesis titled **Designing High-Spin Organic Materials for Spintronic Applications: Structural and Substituent Optimisation in Blatter Tri-Radicals and Triazines** and the work presented in it are my own. I confirm that:

- This work was done wholly or mainly while in candidature for a research degree at this University.
- Where any part of this thesis has previously been submitted for a degree or any other qualification at this University or any other institution, this has been clearly stated.
- Where I have consulted the published work of others, this is always clearly attributed.
- Where I have quoted from the work of others, the source is always given. With the exception of such quotations, this thesis is entirely my own work.
- I have acknowledged all main sources of help.
- Where the thesis is based on work done by myself jointly with others, I have made clear exactly what was done by others and what I have contributed myself.

Signed:

A handwritten signature in black ink, appearing to read 'Jacob Sands', is written over a light blue rectangular background.

Date: 27/05/2025

## Acknowledgements

I would like to express my sincere gratitude to the University of Kent for the opportunity to undertake this Master's research programme and for providing essential resources, including access to computational facilities and the laptop that enabled my research. I am deeply appreciative of the university's support.

I am especially grateful to my supervisors, Dr Felipe Fantuzzi and Dr Tim Kinnear, whose mentorship has been phenomenal. Their encouragement, expertise and patience have not only guided me through my research but have also inspired growth as a scientist. I would also like to thank Dr Maria Alfredsson for her supervision as the chair supervisor and for the perspectives and encouragement in the meetings we had.

I would like to extend my thanks to the University of Cyprus, particularly to Prof Panayiotis Koutentis and his team, for the collaborative experience and warm hospitality during my time in Cyprus. Having the chance to present my research internationally and share insights with their group was an invaluable opportunity that broadened my perspective and allowed me to gain experience in scientific communication.

Additionally, I am grateful to the SISC and KAIROS research teams for making this year more than just research, fostering a collaborative environment where friendships were formed. Working alongside them has given me a meaningful sense of what it means to be part of an active research group. I am particularly thankful to Cauê Souza, whose friendship and support throughout this year helped me overcome obstacles with a sense of resilience and optimism.

Lastly, to each of you who has been part of this journey: thank you, and may God bless you. You have made the experience of undertaking this research Master's more meaningful than words can express.

## Abstract

High-spin Blatter-type tri-radicals represent a unique class of polyradicals with promising applications in materials science, electronics, and spintronics, attributed to their stability, antiferromagnetic behaviour, and  $\pi$ -spin delocalisation. However, broader application of these compounds has been hindered by limited understanding of how structural variations, including geometry and substituent effects, influence their electronic properties and stability, particularly the doublet-quartet (D–Q) energy gap. This thesis addresses these gaps by examining how geometry and substituent modifications affect the electronic structure, ground-state multiplicity, and excited-state topology of Blatter-type tri-radicals and additional triazine biradicals using DFT benchmarks against high-level multireference calculations. The findings demonstrate that substituents play a pivotal role: F, as an electron-withdrawing substituent, shortens bond lengths, while Cl and Br induce rotational distortions due to steric hindrance, especially in inner substituent positions. Electron-donating and electron-withdrawing groups also exhibit unique behaviours, with  $\text{NH}_2$  groups introducing deviations and hydrogen bonding, while  $\text{COOH}$  and  $\text{CHO}$  groups maintain planarity yet contribute out-of-plane distortions. Analysis of D–Q gaps reveals that inner substitutions generally reduce gaps due to steric effects, while outer substitutions tend to favour quartet ground states, irrespective of the substituent tested. Further analysis of fused dithiazole-triazine derivatives reveals that, while ring heteroatoms and functional groups influence singlet-triplet energy gaps, all these systems consistently exhibit closed-shell singlet ground states. This thesis provides deeper insights into the electronic properties of Blatter-type tri-radicals and biradical triazines, establishing key design principles for creating stable, high-performance organic polyradicals and advancing the potential of high-spin systems in magnetic and spintronic devices.

## Abbreviations

<b>ACOH</b>	Acetic Acid
<b>AFM</b>	Atomic force microscopy
<b>AILFT</b>	Ab initio ligand field theory
<b>BJ</b>	Becke-Johnson damping function
<b>BS</b>	Broken symmetry
<b>CASPT2</b>	Complete active space second-order perturbation theory
<b>CASSCF</b>	Complete active space self-consistent field
<b>CC</b>	Coupled cluster
<b>CCDC</b>	Cambridge Crystallographic Data Centre
<b>CCS</b>	Coupled cluster with single excitations
<b>CCSD</b>	Coupled cluster with single and double excitations
<b>CCSD(T)</b>	Coupled cluster with singles, doubles, and perturbative triple excitations
<b>CCSDT</b>	Coupled cluster with single, double and triple excitations
<b>CI</b>	Configuration interaction
<b>CID</b>	Configuration interaction with double excitations
<b>CISD</b>	Configuration interaction with single and double excitations
<b>D-Q</b>	Doublet-quartet energy gap
<b>DCM</b>	Dichloromethane
<b>DFT</b>	Density functional theory
<b>DH</b>	Double hybrid
<b>DPLNO</b>	Domain-based local pair natural orbital
<b>EDG</b>	Electron donating group
<b>ESP</b>	Electrostatic potential map
<b>EWG</b>	Electron withdrawing group
<b>FM</b>	Ferromagnetic
<b>FMR</b>	Ferromagnetic resonance
<b>GGA</b>	Generalized gradient approximation
<b>GMR</b>	Giant magnetoresistance
<b>HF</b>	Hartree–Fock
<b>ICE</b>	Iterative configuration expansion
<b>ICF</b>	Inhomogeneity correction factor
<b>ISHE</b>	Inverse spin Hall effect
<b>KS-DFT</b>	Kohn–Sham DFT
<b>LDA</b>	Local-density approximation
<b>LSDA</b>	Local-spin density approximation
<b>LYP</b>	Lee–Yang–Parr
<b>M</b>	Magnetization
<b>MAD</b>	Mean absolute deviation
<b>META-GGA</b>	Meta-generalised gradient approximation
<b>MP</b>	Møller–Plesset
<b>MP2</b>	Second-order Møller–Plesset perturbation theory
<b>MP3</b>	Third-order Møller–Plesset perturbation theory
<b>MP4</b>	Fourth-order Møller–Plesset perturbation theory
<b>MRAM</b>	Magnetic random-access memory
<b>NEVPT2</b>	N-electron valance state second-order perturbation theory



<b>NIR</b>	Near infrared
<b>NM</b>	Non-magnetic
<b>ODMR</b>	Optically detected magnetic resonance
<b>OF-DFT</b>	Orbital-free DFT
<b>OFET</b>	Organic field transistors
<b>OLEDs</b>	Organic light emitting diodes
<b>OMBD</b>	Organic molecular beam deposition
<b>PBE</b>	Perdew–Burke–Ernzerhof
<b>Pn</b>	Pnictogen
<b>RAM</b>	Random-access memory
<b>RIJCOSX</b>	Resolution of the identity for Coulomb and chain of spheres for exchange
<b>RMSD</b>	Root-mean-square deviation
<b>SCRF</b>	Self-consistent reaction field
<b>SF-DFT</b>	Spin-flip DFT
<b>SMD</b>	Solvent model based on density
<b>SOMO</b>	Singly occupied molecular orbital
<b>S-T</b>	Singlet-Triplet
<b>STM</b>	Scanning tunnelling microscopy
<b>SVP</b>	Spin valance polarised
<b>TMR</b>	Tunnelling magnetoresistance
<b>TPPE</b>	Two-photon photoemission
<b>UHF</b>	Unrestricted Hartree–Fock
<b>UEG</b>	Uniform electron gas
<b>μSR</b>	Low energy muon spin rotation
<b>vdW</b>	van der Waals

## List of Figures

<b>Figure 1.1</b> Three key processes in spintronics: spin injection, spin transport, and spin detection. <sup>5</sup>	2
<b>Figure 1.2</b> (a): Illustration of Giant Magnetoresistance (GMR) technology, the pioneering commercial application in the field of spintronics, used for reading data on hard drives. (b) The iPod Classic, a notable example of GMR's application, utilising this innovation for efficient music data storage and access. <sup>25</sup>	6
<b>Figure 1.3</b> Structure of a polychlorinated trityl-radical. <sup>35</sup>	9
<b>Figure 1.4</b> Structures of (A) 2,2,6,6-tetramethylpiperidin-N-oxyl (TEMPO) and (B) $\alpha$ -nitronyl nitroxide (R: substituent). <sup>39,40</sup>	9
<b>Figure 1.5</b> (A) Structure of the Blatter radical with aromatic sites labelled. (B) Highlighted regions showing spin delocalisation in green and spin isolation in red. <sup>56,61</sup>	13
<b>Figure 1.6</b> Synthetic route 1 of Blatter radicals ( $R_1$ = aryl; $R_2$ = aryl/heterocyclic aryl, $CF_3$ , SMe, Cl, Br, I; $R_3$ = aryl, $CF_3$ , tBu). <sup>61</sup>	15
<b>Figure 1.7</b> Synthetic route 2 of Blatter radicals ( $R_1$ = aryl; $R_2$ = aryl/heterocyclic aryl, $CF_3$ , SMe, Cl, Br, I; $R_3$ = aryl, $CF_3$ , tBu). <sup>61</sup>	<b>Error! Bookmark not defined.</b>
<b>Figure 1.8</b> Synthetic route 3 of Blatter radicals ( $R_1$ = aryl; $R_2$ = aryl/heterocyclic aryl, $CF_3$ , SMe, Cl, Br, I; $R_3$ = aryl, $CF_3$ , tBu). <sup>61</sup>	17
<b>Figure 1.9</b> Synthetic routes 4 of Blatter radicals ( $R_1$ = aryl; $R_2$ = aryl/heterocyclic aryl, $CF_3$ , SMe, Cl, Br, I; $R_3$ = aryl, $CF_3$ , tBu). <sup>61</sup>	18
<b>Figure 1.10</b> Synthesis of 3,3',3''-(benzene-1,3,5-triyl)tris(1-phenyl-1H-benzo[e][1,2,4]triazin-4-yl) (13). <sup>74</sup>	19
<b>Figure 1.11</b> Electrostatic surface potential map of the Blatter mono-radical 1 and tri-radical 13. <sup>75</sup>	23
<b>Figure 1.12</b> Structure of Blatter-type radicals 14–16. <sup>61</sup>	24

<b>Figure 1.13</b> Structure of Blatter-type radicals <b>17–22</b> and oxidation products <b>23</b> and <b>24</b> . <sup>61</sup> ...	25
<b>Figure 1.14</b> Structure of Blatter-type radical <b>25</b> . <sup>61</sup> .....	26
<b>Figure 1.15</b> Proposed diradical structures of the fused dithiazole-triazine systems <b>26–28</b> ....	28
<b>Figure 2.1</b> Perdew’s metaphorical Jacob’s ladder highlights the five stages of exchange-correlation models in DFT, with each rung providing new physical depth and a step closer to better accuracy. ....	36
<b>Figure 3.1</b> RMSD values for five DFT functionals compared against the crystal structure of Blatter mono-radical <b>1</b> .....	62
<b>Figure 3.2</b> RMSD values for five DFT functionals compared against the crystal structure of Blatter tri-radical <b>13</b> . ....	63
<b>Figure 3.3</b> Selected optimised outer-substituted structures (quartet state) of the Blatter tri-radical at the PBE0-D3(BJ)/def2-SVP level of theory. Top-left shows CH <sub>3</sub> , top-right depicts CH <sub>2</sub> F, bottom-left illustrates CHF <sub>2</sub> , and bottom-right presents CF <sub>3</sub> .....	65
<b>Figure 3.4</b> Selected optimised outer-substituted structures (quartet state) of the Blatter tri-radical at the PBE0-D3(BJ)/def2-SVP level of theory. Top-left shows CH <sub>3</sub> , top-right depicts CH <sub>2</sub> Cl, bottom-left illustrates CHCl <sub>2</sub> , and bottom-right presents CCl <sub>3</sub> .....	67
<b>Figure 3.5</b> Selected optimised outer-substituted structures (quartet state) of the Blatter tri-radical at the PBE0-D3(BJ)/def2-SVP level of theory. Top-left shows CH <sub>3</sub> , top-right depicts CH <sub>2</sub> Br, bottom-left illustrates CHBr <sub>2</sub> , and bottom-right presents CBr <sub>3</sub> .....	69
<b>Figure 3.6</b> Selected optimised inner-substituted structures (quartet state) of the Blatter tri-radical at the PBE0-D3(BJ)/def2-SVP level of theory. Top-left shows CH <sub>3</sub> , top-right depicts CH <sub>2</sub> F, bottom-left illustrates CHF <sub>2</sub> , and bottom-right presents CF <sub>3</sub> .....	71
<b>Figure 3.7</b> Selected optimised inner-substituted structures (quartet state) of the Blatter tri-radical at the PBE0-D3(BJ)/def2-SVP level of theory. Top-left shows CH <sub>3</sub> , top-right depicts CH <sub>2</sub> Cl, bottom-left illustrates CHCl <sub>2</sub> , and bottom-right presents CCl <sub>3</sub> .....	73

<b>Figure 3.8</b> Selected optimised inner-substituted structures (quartet state) of the Blatter tri-radical at the PBE0-D3(BJ)/def2-SVP level of theory. Top-left shows CH <sub>3</sub> , top-right depicts CH <sub>2</sub> Br, bottom-left illustrates CHBr <sub>2</sub> , and bottom-right presents CBr <sub>3</sub> .....	74
<b>Figure 3.9</b> Selected optimised outer-substituted structures (quartet state) of the Blatter tri-radical at the PBE0-D3(BJ)/def2-SVP level of theory. From top-left to bottom-right: NO <sub>2</sub> , COOH, H, Ph, NH <sub>2</sub> , and CH <sub>3</sub> .....	76
<b>Figure 3.10</b> Selected optimised outer-substituted structures (quartet state) of the Blatter tri-radical at the PBE0-D3(BJ)/def2-SVP level of theory. From top-left to bottom-right: NH <sub>2</sub> , CH <sub>3</sub> , COOH, CHO.....	78
<b>Figure 3.11</b> Representation of the Blatter tri-radical: the left-hand side displays the calculated doublet-quartet gaps using the PBE0-D3(BJ)/def2-SVP method, while the right-hand side features the electrostatic potential map alongside a literature-reported doublet-quartet gap value using B3LYP. ....	80
<b>Figure 3.12</b> Comparison of multireference calculations with PBE0 data for doublet-quartet energy gaps (cm <sup>-1</sup> ) for the Blatter tri-radical <b>13</b> . Data includes calculations with dynamic correlation (NEVPT2/CASSCF) and without (CASSCF), for active spaces ranging from (3,3) to (11,11). Green bars represent post-HF calculations, while the red bar corresponds to the DFT (PBE0-D3(BJ)/def2-SVP) value. Results for NEVPT2/CASSCF(9,9) are excluded due to convergence issues. ....	82
<b>Figure 3.13</b> Calculated doublet-quartet energy gaps (cm <sup>-1</sup> ) for the Blatter tri-radical <b>13</b> . Energies for selected functionals are compared to reference values. Each bar represents a different functional, with reference values from NEVPT2/CASSCF(11,11) and PBE0-D3(BJ) shown in red, and results from other functionals displayed in green.....	82
<b>Figure 3.14</b> Optimized energies for the doublet-quartet gaps for all of the outer substituted systems, calculated at the PBE0-D3(BJ)/def2-SVP level of theory. Each bar represents a	

different system within the outer series, with halide-containing groups shown in red and the electron-withdrawing and electron-donating groups displayed in green. .... 84

**Figure 3.15** Single-point energies for the doublet-quartet gaps across all outer-substituted systems, calculated at the B3PW91-D3(BJ)/def2-TZVPP//PBE0-D3(BJ)/def2-SVP level of theory. Each bar represents a unique system within the outer series, with halide-containing groups highlighted in red, and electron-withdrawing and electron-donating groups shown in green. Notably, two outer systems exhibit anomalously high values, suggesting significant error; these points are displayed on the right-hand side of the figure for completeness. .... 85

**Figure 3.16** Comparison of single-point energies for the doublet-quartet gap in the outer systems, focusing on three groups: N(Me)<sub>2</sub>, NO<sub>2</sub>, and Ph. Calculations for B3PW91 were performed at the B3PW91-D3(BJ)/def2-TZVPP//B3PW91-D3(BJ)/def2-SVP level, while PBE0 calculations used the PBE0-D3(BJ)/def2-TZVPP//PBE0-D3(BJ)/def2-SVP level of theory. Data is colour-coded, with B3PW91 results in green and PBE0 results in red. One B3PW91 value shows an anomalously high result, included for completeness. .... 88

**Figure 3.17** D–Q energy gaps for all of the inner substituted systems, calculated at the PBE0-D3(BJ)/def2-SVP level of theory. Each bar represents a different system within the inner series, with halide-containing groups shown in red and the remaining electron-withdrawing and electron-donating groups displayed in green. .... 90

**Figure 3.18** D–Q energy gap data for inner systems containing halide groups, compared to a reference methyl group, calculated at the B3PW91-D3(BJ)/def2-TZVPP//PBE0-D3(BJ)/def2-SVP of theory. Halide-containing groups are displayed in red, while the methyl group is shown in green as the reference point. The halide data are symmetrically distributed around the methyl group with four above and below the reference point, with chlorine- containing groups exhibiting the highest and lowest energy values. .... 91

**Figure 3.19** D–Q energy gap data for inner systems with both electron withdrawing and electron-donating groups, calculated using the B3PW91-D3(BJ)/def2-TZVPP//PBE0-D3(BJ)/def2-SVP level of theory. This comparison highlights the influence of electron withdrawing and electron-donating groups on energy values within the inner system. .... 92

**Figure 3.20** Comparison of D–Q energy gaps in the inner bromine-containing systems, calculated using both B3PW91 and PBE0 methods. Calculations for the B3PW91 method were performed at the B3PW91-D3(BJ)/def2-TZVPP//B3PW91-D3(BJ)/def2-SVP level, while the PBE0 calculations used the PBE0-D3(BJ)/def2-TZVPP//PBE0-D3(BJ)/def2-SVP level of theory. The data is colour-coded, with B3PW91 systems shown in green and PBE0 systems in red. Notably, B3PW91 exhibits two instances where the energy gap exceeds  $7000\text{ cm}^{-1}$ , displayed as errors due to exceedingly high values. .... 93

**Figure 3.21** Energy gaps for fused dithiazole-triazine derivatives, the aza-acene tri-radical and the Blatter-type Schatz diradical, optimized at the PBE0-D3(BJ)/def2-SVP level of theory. Systems are colour-coded to illustrate structural variations: yellow for dithiazole-triazine systems **26a–28a**, navy for **29** and **30**, orange for phosphorus-containing systems **26–28b**, grey for selenium-containing systems **26c–28c**, dark blue for CN group additions to **26a–28a**, and red for the corresponding OCH<sub>3</sub> group additions. .... 95

## List of Equations

Equation 1.....	32
Equation 2.....	33
Equation 3.....	33
Equation 4.....	33
Equation 5.....	34
Equation 6.....	34
Equation 7.....	36
Equation 8.....	37
Equation 9.....	38
Equation 10.....	38
Equation 11.....	38
Equation 12.....	39
Equation 13.....	40
Equation 14.....	40
Equation 15.....	41
Equation 16.....	41
Equation 17.....	42
Equation 18.....	42
Equation 19.....	43
Equation 20.....	43
Equation 21.....	44
Equation 22.....	46
Equation 23.....	54
Equation 24.....	55

Equation 25.....	55
Equation 26.....	58
Equation 27.....	59



# Chapter

## 1. Introduction

### 1.1 Background Theory of Spintronics

#### 1.1.1 Introduction to Spintronics

Spintronics is an interdisciplinary field that sits at the crossroads of quantum mechanics and electronics, opening up exciting new possibilities for information storage and processing. While traditional electronics rely solely on the electron's charge to enable functionality, spintronics takes into account both charge and the intrinsic quantum property of electron spin—whether in an "up" or "down" state—to add a new dimension to device operation.<sup>1</sup> This dual use of charge and spin promises to transform device performance, offering greater speed, efficiency, and scalability that could reshape the future of technology.

The origins of spintronics trace back to Mott's model in 1936, which explained electrical conduction in magnetic materials as driven by two types of electrons with opposite spins.<sup>2</sup> Since then, the field has evolved to encompass a range of foundational processes (**Figure 1.1**), which includes spin injection, spin transport, and spin detection, all contributing to the unique and powerful capabilities of spintronic devices.<sup>1,3</sup>

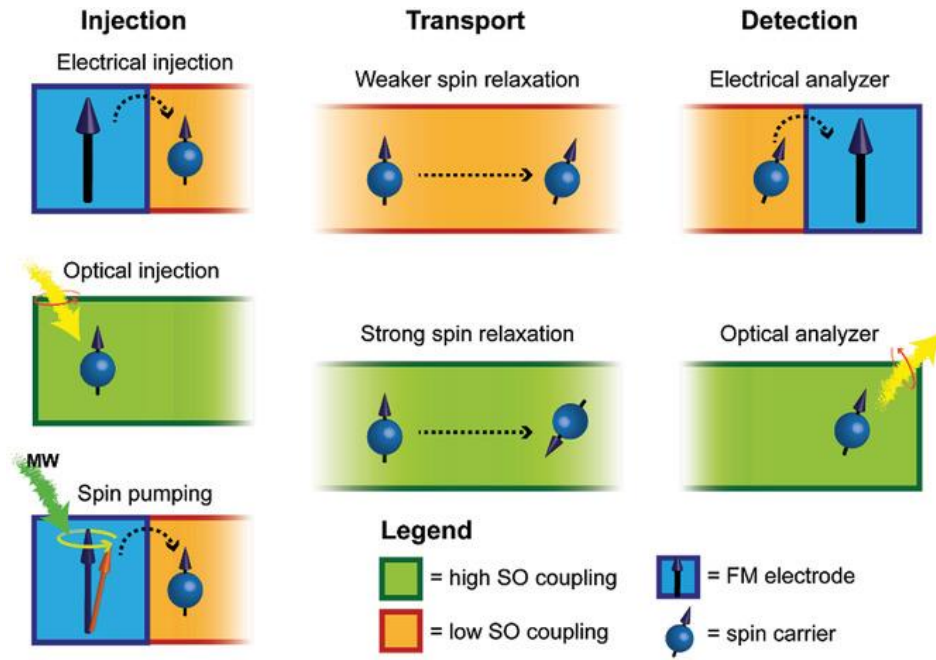


**Figure 1.1** Three key processes in spintronics: spin injection, spin transport, and spin detection. Figure taken from Privitera et al. (2021).<sup>4</sup>

The first step in spintronic devices is to inject spin-polarised electrons into a non-magnetic (NM) semiconductor. This can be achieved through three main techniques: electrical injection,<sup>1</sup> optical injection, and spin pumping. In electrical injection, a ferromagnetic (FM) material serves as a spin injector, where the magnetisation (M) creates an imbalance between the concentrations of majority and minority spins. When a current flows from the FM to the NM material, it carries the spin polarisation. However, achieving efficient spin injection is often hindered by the conductivity mismatch problem, in which the ohmic contacts<sup>5</sup> between the FM and NM materials lead to poor spin injection due to the differences in conductivity of spin-up and spin-down electrons. This issue has partially been resolved due to the use of dilute magnetic semiconductors or half metallic ferromagnets and by incorporating tunnel barriers, which enhance spin injection efficiency through spin-dependent tunnelling.<sup>6</sup>

An alternative approach to spin injection is known as optical injection, where circularly polarised photons transfer angular momentum to the electron's orbital momenta. This angular

momentum is then converted into electron spin through spin-orbit (SO) coupling (*vide infra*), a process particularly effective in materials featuring heavy elements. Lastly, spin pumping<sup>7</sup> involves generating a pure spin current through the excitation of spin waves (magnons)<sup>8</sup> in FM materials via ferromagnetic resonance (FMR). This method allows for spin transfer into an adjacent NM layer without any associated charge flow, creating a highly efficient means of spin injection.

Once the spin-polarised electrons are injected, they must travel across the NM semiconductor while maintaining their polarisation. However, various spin relaxation mechanisms—such as SO coupling, exchange interaction, and hyperfine interaction—can disrupt spin polarisation during the transport. Materials with high SO coupling, such as inorganic semiconductors and certain hybrid organic-inorganic perovskites, typically exhibit rapid spin relaxation, which reduces their suitability for effective spin transport.<sup>4</sup> Conversely, materials with low SO coupling, such as organic semiconductors, display longer spin relaxation times, which provides better spin transport properties. However, these materials are generally less efficient at generating spin polarisation via optical means.<sup>4</sup>

The final stage in a spintronic device is detecting that the spin state of electrons, which can be achieved through both electrical and optical methods.<sup>9</sup> Electrical detection typically employs FM electrodes as spin detectors, exploiting phenomena such as giant magnetoresistance (GMR, *see below*)<sup>10,11</sup> and tunnelling magnetoresistance (TMR). In GMR, the electrical resistance of the device varies depending on the relative alignment (parallel or antiparallel) of the magnetisations of the FM injector and detector, allowing for the detection of spin-polarised carriers tunnelling through a thin spacer layer. The efficiency of this process is controlled by the spin polarisation of the density of states at the Fermi level—the energy level at which electrons are likely to occupy states at absolute zero temperature—of the FM electrodes.<sup>4</sup>

Another technique for spin detection relies on the inverse spin Hall effect (ISHE),<sup>3,12</sup> where a pure spin current is converted into a charge current, generating an electromotive force within the FM layer. In this process, spin-polarised electrons moving within a non-magnetic material experience a deflection due to SO interactions, creating a transverse charge current that can be measured as an indicator of spin polarisation. ISHE is particularly valuable for detecting spin currents without disrupting the spin system.<sup>13</sup>

Optical detection,<sup>9</sup> on the other hand, is especially effective in materials with strong SO coupling, as it can non-invasively probe spin dynamics. Techniques such as optically detected magnetic resonance (ODMR)<sup>14</sup> allow for the detection of spin states by measuring changes in fluorescence as a response to microwave-induced transitions between spin states. This technique is highly sensitive and useful in studying spin coherence and relaxation times.

Two-photon photoemission (TPPE)<sup>15</sup> is another optical technique, which involves exciting electrons to higher energy states using two photons. The excited electrons can be ejected from the materials and analysed, bringing insights into the electronic structure and spin polarisation near the surface. TPPE is beneficial in materials where surface spin properties play a crucial role in device performance.

Finally, low energy muon spin rotation ( $\mu$ SR) spectroscopy<sup>16,17</sup> is yet another alternative method for probing spin polarisation in these materials.<sup>18</sup> In this case, spin-polarised muons are implanted into the material, acting as local magnetic probes. The precession of the muon spin within the magnetic field of the material brings information about the internal magnetic environment and spin interactions within the sample. This method finds advantage in the study of spin properties in bulk materials and offers a unique perspective on magnetic and electronic structures in materials with complex spin behaviours.

To summarise, spintronics represents a promising path for developing new types of electronic devices that are faster, more efficient, and capable of storing more information than their traditional counterparts. The intricate interplay of spin injection, transport and detection underpins the functionality of spintronic devices and drives current and future works to overcome challenges and improve performance.

### 1.1.2 Principles of Spintronics in Electronic Devices

The late 1980s marked a significant turning point in spintronics with the discovery of GMR. This effect was first reported by Baibich et al. in 1988 and 1989,<sup>19,20</sup> who found that electrical resistance in specific materials could vary depending on their magnetic arrangement. GMR occurs in multilayered materials composed of alternating magnetic and non-magnetic layers, where the relative alignment of the magnetisation in these layers—either parallel or antiparallel—results in a significant change in resistance.<sup>19,20</sup> Mathematically the resistance  $R$  in such materials can be expressed as either  $R = R_{\text{parallel}}$  or  $R = R_{\text{antiparallel}}$ , where:

$$R_{\text{antiparallel}} > R_{\text{parallel}} \quad (1.1)$$

illustrating that resistance is higher when the magnetic layers are aligned antiparallel compared to parallel.

These finding led to major advancements in data storage technology, especially in the design of read heads for hard disk drives, which achieved much higher data storage capacities as a result of the sensitivity of GMR-based sensors to magnetic fields.<sup>21</sup> This innovation facilitated a new era of miniaturised data storage devices with significantly increased capacities. Enhanced read head designs also enabled faster data access and more efficient hard disk performance, contributing to the reliability and performance essential for modern computing.<sup>22</sup>

Over the years, the impact of GMR has extended from consumer electronics to enterprise-level data centres, reflecting its crucial role in the evolution of digital storage solutions and solidifying its status as a foundation for modern information technology infrastructures.

In hard disk drives, binary data is encoded using two magnetic states, which are represented by one (1) and zero (0), and stored on rotating circular platters (**Figure 1.2**). Small components known as disk heads, which resemble needles,<sup>23</sup> move over these platters to read and write data. During the reading process, the disk heads convert magnetic fields on the platters into electrical currents, while writing involves converting electrical currents back into magnetic fields.

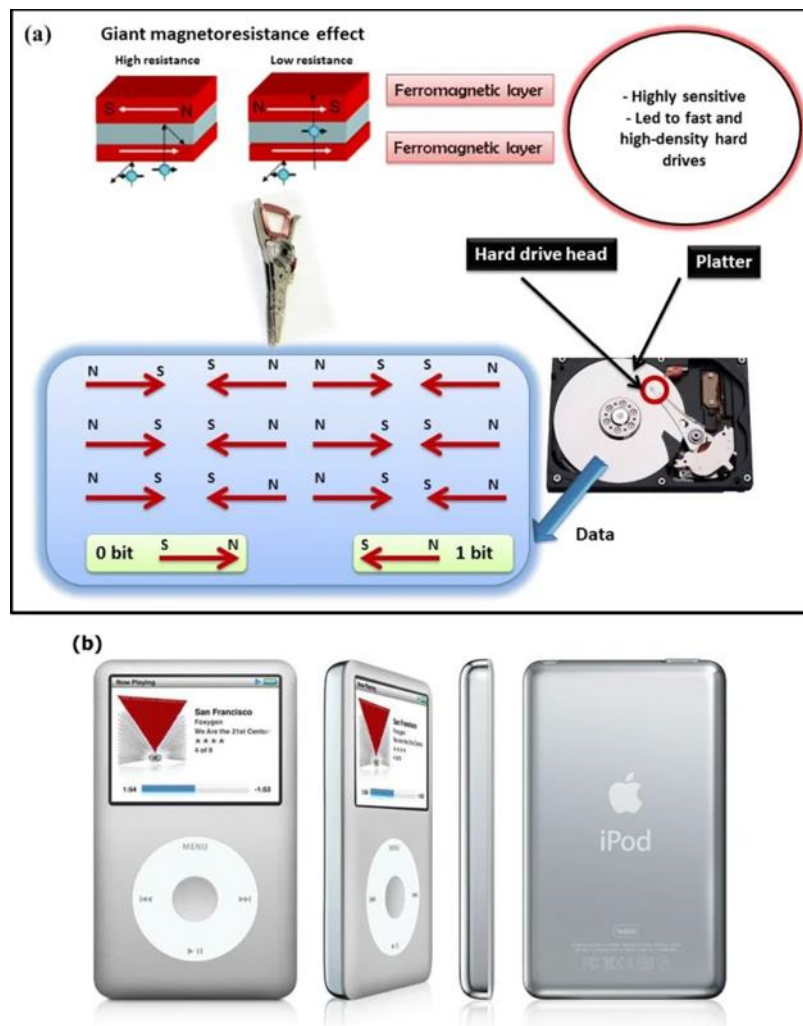


**Figure 1.2 (a):** Illustration of Giant Magnetoresistance (GMR) technology, the pioneering commercial application in the field of spintronics, used for reading data on hard drives. **(b)** The iPod Classic, a notable example of GMR's application, utilising this innovation for efficient music data storage and access. *J Supercond Nov Magn* (2020).<sup>24</sup>

A GMR system consists of two magnetic layers separated by a non-magnetic layer,<sup>25</sup> which exhibits a significant resistance change—20%—<sup>26</sup> when exposed to a magnetic field shift, in contrast to early magnetic sensors that only showed a few percent change. As mentioned before, when the two magnetic layers are aligned in parallel, the system experiences low resistance; however, when they are aligned antiparallel, the resistance is high. This change in resistance enables efficient detection of magnetic data stored on the hard drive platters, enabling the development of faster, high-capacity drives, such as modern 500-gigabyte hard drives.

A successful application of GMR technology in disk heads can be seen in devices like iPod, developed by Apple. This achievement inspired further research on the potential of replacing traditional semiconductor components—such as random-access memory (RAM), microprocessors, and transistors—with their magnetic counterparts, namely magnetic RAM (MRAM), magnetic microprocessors, and spin transistors. A key advantage of MRAM is its ability to retain information even when power is lost, unlike conventional RAM, which loses unsaved data when powered off.<sup>22</sup> Furthermore, MRAM-powered devices eliminate the need for a boot-up waiting period upon powering on,<sup>27</sup> providing a faster and more efficient user experience.

MRAM employs electron spin for data storage, with the first MRAM chip released by Freescale in July 2006.<sup>28</sup> Everspin later introduced a 256-Mb MRAM model in 2016.<sup>29</sup> These developments highlight the expanding impact of GMR, which not only transformed hard disk drive technology but also laid the groundwork for further advancements in magnetic materials and data storage technologies. GMR continues to be a cornerstone of modern electronics, driving ongoing innovations in data storage.

## 1.2 Organic Radicals in Spintronics

### 1.2.1 Overview of Organic Spintronics

Organic radicals are open-shell molecules primarily composed of light elements, such as hydrogen, carbon, nitrogen, oxygen and sulphur. Due to their electron configuration, these molecules are highly reactive, characterised by an unpaired electron occupying the highest molecular orbital. This unpaired electron can easily engage in reactions like hydrogen abstraction, dimerization, or recombination, leading to the loss of the open-shell character. However, it is possible to achieve persistent organic radicals by shielding the paramagnetic centre with bulky substituents, protecting it from undesired interactions.<sup>30,31</sup>

The development of persistent organic radicals has opened new avenues for applications across various fields, including organic spintronics, in which the control of the electron spin is crucial. As mentioned before, spintronics involves using the spin of electrons, rather than just their charge, for information processing and storage, which can lead to faster and more efficient electronic devices. Organic radicals are particularly appealing in this context due to their ability to maintain stable, unpaired electrons over extended periods.<sup>32,33</sup>

Polychlorinated trityl-radicals<sup>34</sup> exemplify this approach (**Figure 1.3**), wherein steric protection stabilises the central  $sp^2$  carbon atom carrying the unpaired electron.<sup>35</sup> Since the discovery of the triphenylmethyl radical by Gomberg in 1900,<sup>36</sup> the unique physical properties of neutral radicals have sparked extensive research into molecule-based functional materials, including those designed for spintronics.



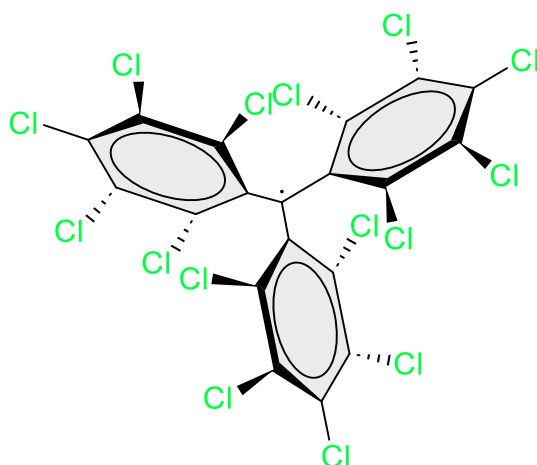


**Figure 1.3** Structure of a polychlorinated trityl-radical. Ratera et al (2021).<sup>34</sup>

Magnetism, resulting from interactions between unpaired electrons, is one of the key features that make these radicals suitable for spintronics applications. In the solid state, proper alignment of spins through  $\pi$  electrons or lone pairs from heteroatoms can lead to the formation of molecule-based magnetic materials. For example, compounds like 2,2,6,6-tetramethylpiperidin-N-oxyl (TEMPO) and  $\alpha$ -nitronyl nitroxides (**Figure 1.4**), synthesised over fifty years ago,<sup>37</sup> have been important in advancing the fields of molecule-based magnetism and spin science.

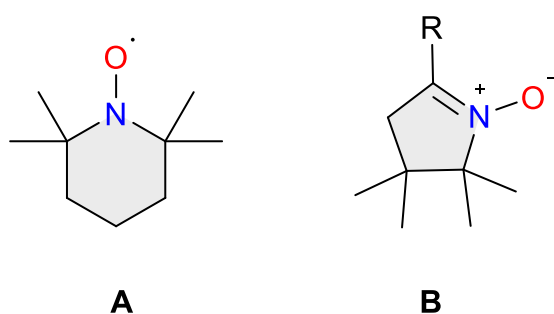


**Figure 1.4** Structures of (A) 2,2,6,6-tetramethylpiperidin-N-oxyl (TEMPO) and (B)  $\alpha$ -nitronyl nitroxide (R: substituent). Zhou et al. (2014), Deumal et al. (2001).<sup>38,39</sup>

Advancing spintronics relies heavily on the design and synthesis of stable neutral radicals with innovative molecular structures. Organic spintronics utilises organic radicals as active components, offering a promising approach to developing next-generation spintronic devices. These organic systems provide unique advantages, such as tuneable electronic properties, low-cost fabrication, and flexibility—characteristics that are challenging to achieve with conventional inorganic materials.<sup>37,40</sup> Through the careful exploration of the structural diversity of organic molecules, spin stabilisation can be optimised, and electronic structures finely controlled. Both are essential for managing the intramolecular interactions that determine the performance and efficiency of the spintronic materials.<sup>41</sup>

### 1.2.2 Role of Organic Molecules in Spintronics

Organic molecules play a pivotal role in advancing spintronics, particularly through their use as organic semiconductors. These materials have gained attention in spintronics due to their unique spin-related properties, resulting from their composition of light atoms (C, H, N, and O) that inherently provide longer spin relaxation times by minimising spin-scattering mechanisms.<sup>9,42</sup> This feature enables organic semiconductors to hold promise for spintronic applications that demand extended spin coherence and efficient spin transport. The two principal types of organic semiconductors are small organic molecules and semiconducting polymers, which offer flexibility in material design, processing, and integration with conventional electronic systems.<sup>43,44</sup>

A distinguishing feature of organic semiconductors in spintronics is their localised charge carriers, or polarons, which arise from the limited overlap between  $\pi$ -conjugated electronic states and the strong coupling between these states and molecular vibrations.<sup>45</sup> Unlike inorganic materials, where charge carriers are typically delocalised and described by Bloch

wavefunctions, organic semiconductors often depend on hopping mechanisms—a process in which charge carriers move between localised sites via thermal activation or tunnelling rather than travelling through continuous, delocalised states—for charge and spin transport.<sup>46–48</sup> This localisation enables enhanced spin relaxation times but simultaneously challenges the traditional band-structure approaches.

### 1.2.3 Characteristics of Polyradicals in Organic Spintronics

Polyradicals, with their inherent magnetic properties, have emerged as promising materials in organic spintronics. Their multiple unpaired electrons provide a unique platform for achieving high spin densities and facilitating magnetic interactions, which are crucial for efficient spin transport. In organic semiconductors, spin transport is influenced by two primary mechanisms: hopping and exchange coupling.<sup>49</sup>

At low charge carrier concentrations, the hopping mechanism links spin and charge transport. It involves the discrete movement of charge carriers (electrons or holes) between localised molecular sites, driven by thermal activation or quantum tunnelling. During hopping, spins are carried along with charges, leading to a coupling between spin and charge transport. This mechanism is especially relevant in organic systems due to their inherent structural disorder, which creates localised electronic states.

In turn, at higher charge densities, exchange coupling—a process in which spin interactions are facilitated through overlapping molecular orbitals, allowing spins on neighbouring sites to align and transfer more efficiently—enables faster, decoupled spin diffusion.<sup>50,51</sup> This makes polyradicals particularly effective in enhancing spin coherence and spin diffusion lengths in organic semiconductor devices.

Spin relaxation mechanisms, which are key to spintronic functionality, include SO coupling, hyperfine interactions, and exchange interactions.<sup>51</sup> SO coupling, a relativistic effect, arises from the interaction between an electron's intrinsic spin angular momentum and its orbital angular momentum around the nucleus. The strength of this interaction increases in atoms with higher atomic numbers. In organic materials, composed mostly of lighter atoms, SO coupling is weak, which makes the hyperfine interactions the primary driver of spin relaxation.<sup>51</sup> Hyperfine interactions arise from the coupling between an electron's spin and the magnetic field generated by nuclear spins within a molecule. The strength of hyperfine interactions is influenced by factors such as the distance between the electron and nucleus, the type of nucleus, and the specific molecular structure.

In organic spintronic applications, the dominance of hyperfine interactions presents a valuable opportunity for optimisation, as these interactions can be modulated through molecular engineering. For instance, substituting hydrogen with deuterium can reduce hyperfine interactions, thereby extending spin coherence times and improving device performance.<sup>52</sup> Lastly, exchange interactions, involving direct interactions between the spins of neighbouring electrons, facilitate alignment or anti-alignment of spin states. In materials with higher charge densities, such as polyradicals, exchange interactions enable faster, decoupled spin diffusion, essential for creating materials with extended spin diffusion lengths and robust spin retention. The combination of weak SO coupling, tuneable hyperfine interactions, and effective exchange interactions in organic semiconductors with polyradicals positions them as ideal candidates for spintronic devices, offering enhanced spin coherence and stability in transport processes.

## 1.3 Blatter-Type Radicals

### 1.3.1 Definition and Structure of Blatter-Type Tri-Radicals

Blatter-type radicals are a category of persistent organic radicals, first reported in 1968 by Herbert Blatter.<sup>53</sup> These compounds are based on a 1,2,4-benzotriazin-4-yl core, which allows them to remain stable under normal conditions. Interest in these molecules has grown significantly due to their unique properties, including their ability to exhibit both antiferromagnetic and ferromagnetic interactions,<sup>54,55</sup> spin  $\pi$ -delocalisation, and low excitation energies.<sup>56,57</sup> These attributes make Blatter-type radicals highly versatile and promising for the applications in fields such as spintronics and molecular electronics, where stable, tuneable spin properties are crucial.

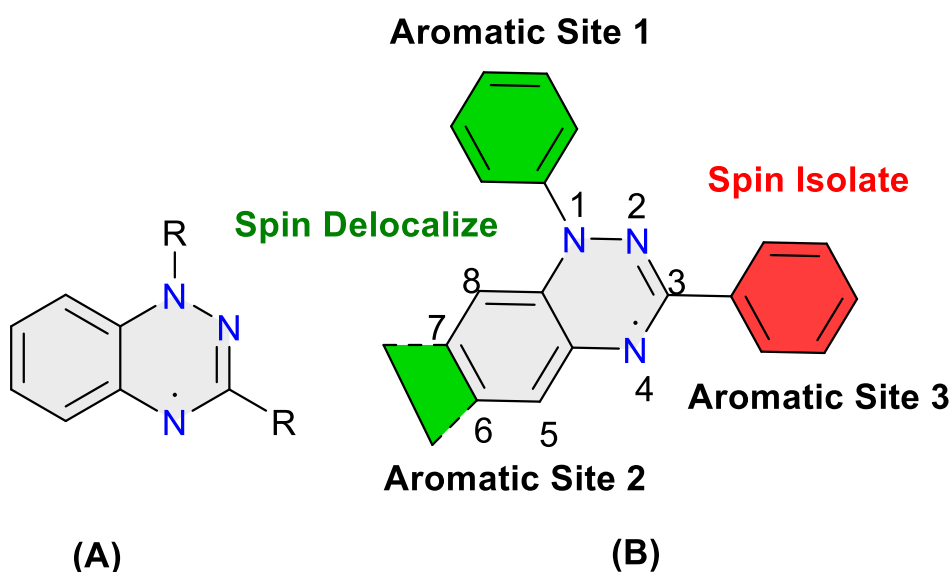


**Figure 1.5** (A) Structure of the Blatter radical with aromatic sites labelled. (B) Highlighted regions showing spin delocalisation in green and spin isolation in red. Zheng et al. (2020).<sup>53,58</sup>

The fundamental structure of the Blatter-type radicals features three functional aromatic sites, with each contributing differently to the molecules' overall properties as shown in **Figure 1.5**. The unpaired electron on the radical is partially delocalised to the aryl group attached at the N1

position, a process influenced by steric interactions between the aryl substituents and the radical core. This delocalisation impacts the electronic characteristics of the molecule. A significant role in the radical's stability and behaviour arises from the resonance of the unpaired electron at the second aromatic site, particularly at C7, which is prone to oxidation without adequate protection.<sup>59</sup> To address this, Koutentis and his group introduced trifluoromethyl groups, effectively shielding C7 from oxidative degradation and enhancing the radical's longevity.<sup>60</sup> Additionally, bridging C6 and C7 with aromatic groups facilitates further spin delocalisation, enabling the formation of high spin states and improving the material's semiconducting properties.<sup>54,55</sup>

Aromatic site 3 remains the most spin isolated, due to the unpaired electron in the Blatter radical core not resonating to this position. Although substituents at C3 do not influence the spin properties, they can still influence the overall electronic structure of the molecule. This allows for fine-tuning and molecular engineering of the radical without affecting its fundamental behaviour. Together, these features highlight the versatility of Blatter-type radicals in material design and their potential for tailored applications.<sup>61,62</sup>

Since their initial synthesis in 1968,<sup>53</sup> significant efforts have been devoted to improve the yield and streamline the preparation process for these stable N- and N/S- rich heterocyclic radicals. Koutentis and colleagues provided a comprehensive review in 2016, summarising advancements in the chemistry and applications of these radicals, particularly focusing on developments in synthetic approaches and outlining four potential preparation routes.<sup>63</sup>

Route 1 (**Figure 1.6**) represents a classical approach to synthesising Blatter radicals via amidrazones, involving ring closure at the N1 position of amidrazones (**2a**) to form 1,3-diphenyl-1,4-dihydro-1,2,4-benzotriazin-4-yl (**4**).<sup>64,65</sup> This process generally proceeds through a two-electron oxidation of **2a** to form 1,2,4-triazabutadienenes (**3a**), followed by cyclisation

to benzotriazines and further oxidation to yield the final Blatter radicals. Alternatively, a one-electron oxidation of the amidrazone to form a hydrazonyl radical (**3b**) can be performed, which ultimately leads to the same product.

#### Route 1

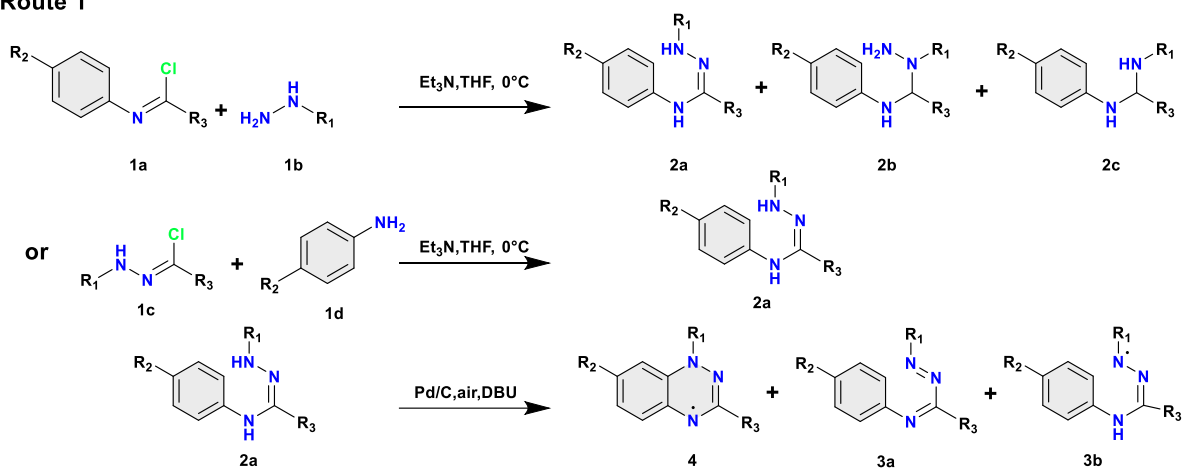


**Figure 1.6** Synthetic route 1 of Blatter radicals ( $R_1$  = aryl;  $R_2$  = aryl/heterocyclic aryl,  $\text{CF}_3$ ,  $\text{SMe}$ ,  $\text{Cl}$ ,  $\text{Br}$ ,  $\text{I}$ ;  $R_3$  = aryl,  $\text{CF}_3$ ,  $t\text{Bu}$ ). Zheng et al. (2020).<sup>58</sup>

Earlier synthesis methods had several drawbacks, primarily due to the use of toxic and expensive oxidants such as mercury oxide and silver oxide, which often resulted in moderate yields and limited derivative exploration.<sup>66,67</sup> However, significant improvements have been made with alternative oxidants, such as  $\text{Pd/C}$  in combination with air and DBU,<sup>64</sup> ruthenium(III) chloride, and potassium ferricyanide. Notably, the use of  $\text{Pd/C}$  with DBU and air has proven particularly efficient, achieving yields between 87–95%. This optimisation highlights the importance of both synthesising pure amidrazones (**2a**) and facilitating efficient ring closure, making this route more practical and environmentally friendly.<sup>41</sup>

Route 2 ([Error! Reference source not found.](#)) involves the formation of the Blatter radical utilising hydrazines (**5a**) as precursors and thereby avoiding intermediates like amidrazones. In this approach, developed by Koutentis and his team, hydrazines undergo cyclodehydration to directly produce the desired Blatter radicals (**4**). The synthesis begins with the substitution of





Route 3 (**Figure 1.8**) employs post-cyclisation and N-acylation as an alternative route to the Blatter radical. A key drawback of Routes 1 and 2 is their relatively low overall yields and the challenges associated with the low reactivity and regioselectivity of N-acylation. Route 3 addresses these issues by introducing functional groups specifically at the N1 position through a post-cyclisation substitution. The main advantage of this method is the extensive range of substituents it enables, allowing for precise control over the spin distribution, electrochemical properties, and intermolecular spin exchange interactions of the radicals. This flexibility makes Route 3 particularly advantageous for tailoring the Blatter radical's properties for specific applications.

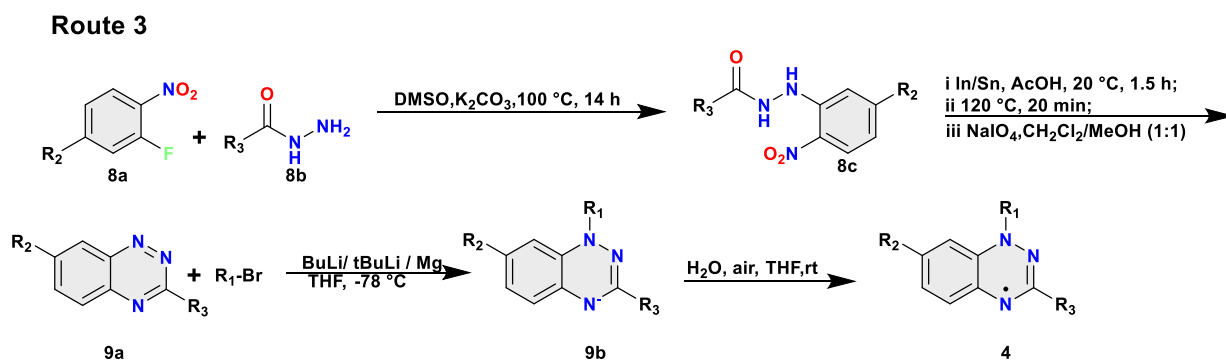


**Figure 1.8** Synthetic route 3 of Blatter radicals ( $R_1$  = aryl;  $R_2$  = aryl/heterocyclic aryl,  $CF_3$ ,  $SMe$ ,  $Cl$ ,  $Br$ ,  $I$ ;  $R_3$  = aryl,  $CF_3$ ,  $tBu$ ).<sup>58</sup>

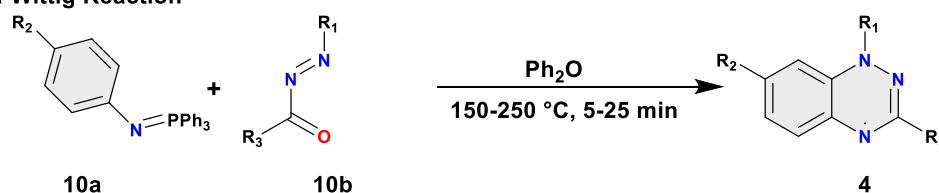
This route involves the use of organometallic reagents (such as  $tBuLi$ ,  $Mg$ , or  $nBuLi$ ) to generate anion intermediates (**9b**), which are then oxidized in air to form the radicals (**4**). The benzo-1,2,4-triazenes (**9a**) used as starting materials are synthesised in a three-step process from benzhydrazides, involving N-arylation followed by reductive ring closure.<sup>69</sup> However, this route does require careful handling under inert conditions and has limitations and functionalities that are incompatible with aryl or alkyl lithium reagents.

In addition to the three main strategies for synthesising the Blatter radical, other methods have been explored to overcome the limitations associated with amidrazones and hydrazides.

Notable alternative approaches (route 4, **Figure 1.9**) include the aza-Wittig reaction, copper-catalysed coupling, and Pschorr-type cyclization, which provide new synthetic pathways. For instance, the reaction between N-aryliminophosphoranes and 1-(het)aryl-2-aryldiazenes yields Blatter radicals directly, with moderate efficiency.<sup>70</sup> This aza-Wittig approach circumvents issues with moisture-sensitive intermediates and costly reagents, allowing for the introduction of a wide range of substituents. These alternative methods offer interesting options for synthesising Blatter radicals that may be difficult to produce through traditional routes, thereby expanding the scope and applicability of these stable heterocyclic compounds.

#### Route 4

##### aza-Wittig Reaction



##### Copper-catalysed coupling reaction

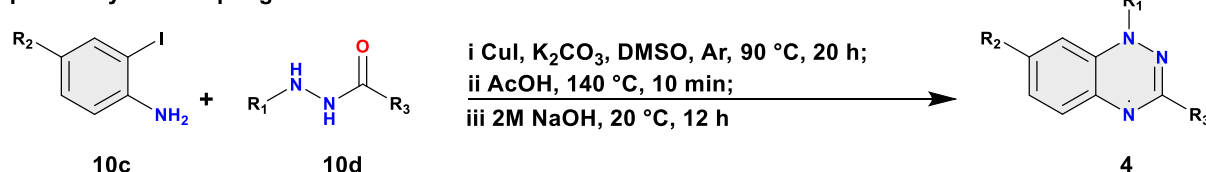


**Figure 1.9** Synthetic routes 4 of Blatter radicals ( $R_1$  = aryl;  $R_2$  = aryl/heterocyclic aryl,  $\text{CF}_3$ ,  $\text{SMe}$ ,  $\text{Cl}$ ,  $\text{Br}$ ,  $\text{I}$ ;  $R_3$  = aryl,  $\text{CF}_3$ ,  $t\text{Bu}$ ) Zheng *et al.* (2020).<sup>58</sup>

Building on the established chemistry of mono-radical Blatter derivatives, attention has shifted toward the synthesis of tri-radicals. Recent research into more complex multi-radical systems, particularly tri-radical Blatter derivatives, opens up new possibilities for spintronic applications. These compounds offer enhanced magnetic interactions and the ability to integrate multiple spin centres within a single molecule, significantly advancing the potential for more robust spin transport and storage functionalities in molecular spintronics.

The synthesis of the tri-radical Blatter compound, 3,3',3''-(benzene-1,3,5-triyl)tris(1-phenyl-1H-benzo[e][1,2,4]triazin-4-yl), is illustrated in **Figure 1.10**. This compound is obtained through a multi-step procedure, beginning with 1-(2-nitrophenyl)-1-phenylhydrazine (**10**) as the starting material. Each step in the process is carefully designed to introduce and stabilise the three radical centres, ultimately yielding a tri-radical structure suitable for advanced spintronic applications.

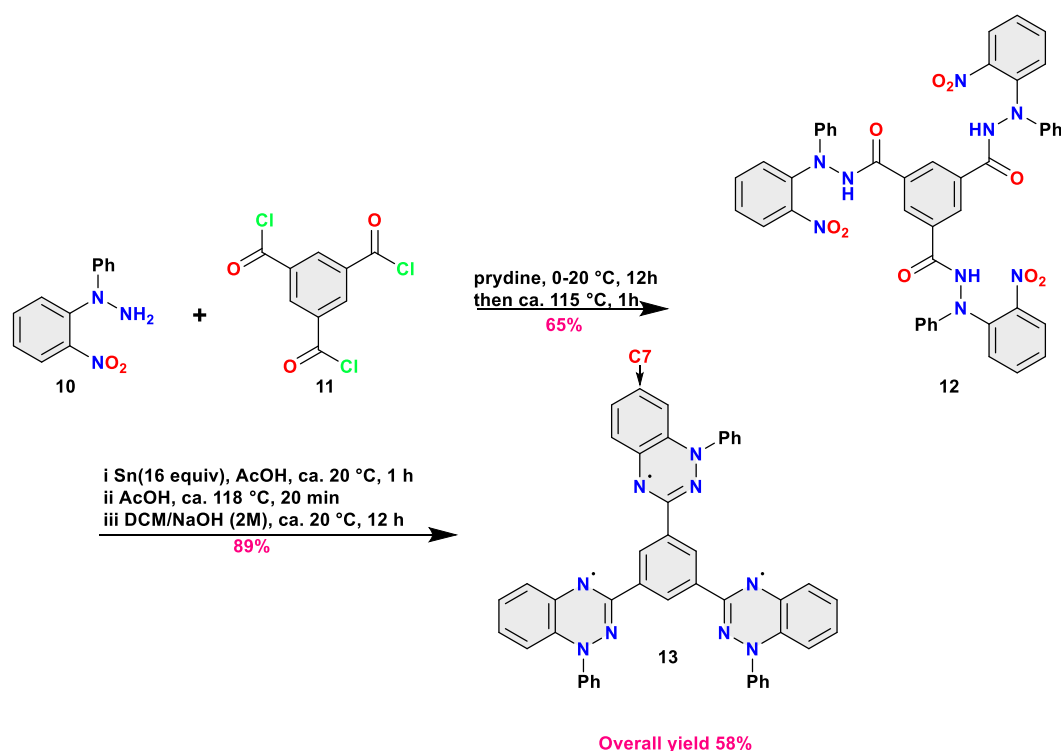


**Figure 1.10** Synthesis of 3,3',3''-(benzene-1,3,5-triyl)tris(1-phenyl-1H-benzo[e][1,2,4]triazin-4-yl) (**13**). The C7 carbon of **13** is highlighted. Adapted from Zissimou et al. (2020).<sup>71</sup>

To synthesise the tricarbonylhydrazide precursor (**12**), a solution of 1-(2-nitrophenyl)-1-phenylhydrazine (**10**) in pyridine was first cooled to 0–5 °C using an ice bath. Then, 0.3 equivalents of 1,3,5-benzenetricarbonyl trichloride (**11**) were added. The mixture was allowed to gradually warm to room temperature (~20 °C) over 12 hours with continuous stirring,

followed by heating to reflux ( $\sim 115^{\circ}\text{C}$ ) for one hour. After treatment with 15%  $\text{H}_2\text{SO}_4$ , the resulting compound, N1,N3,N5-tris(2-nitrophenyl)-N1,N3,N5-triphenylbenzene-1,3,5- tricarbohydrazide (**12**), was isolated as orange prisms in 65% yield, exhibiting a decomposition point above  $171^{\circ}\text{C}$ .<sup>71</sup>

To convert compound **12** to the Blatter tri-radical **13**, reduction, cyclodehydration, and oxidation of the intermediate were necessary. This process began with the reduction of precursor **12** using 16 equivalents of Sn in glacial acetic acid (AcOH) at room temperature for one hour, leading to complete consumption of the starting material, confirmed by thin layer chromatography (TLC) analysis.<sup>72</sup> This reduction yielded the intermediate, N1,N3,N5-tris(2-aminophenyl)-N1,N3,N5-triphenylbenzene-1,3,5-tricarbohydrazide. The intermediate then underwent cyclodehydration by heating to reflux ( $\sim 118^{\circ}\text{C}$ ) for 20 minutes, forming a leuco triazine. This crude leuco triazine was subsequently treated overnight with 2M NaOH in the presence of air, promoting oxidation. The final product was purified via chromatography on neutral  $\text{Al}_2\text{O}_3$  using dichloromethane (DCM) as the eluent ( $R_f$  0.68) and was then recrystallised. The resulting tri-radical compound (**13**) was obtained as black needles, with a decomposition point above  $312^{\circ}\text{C}$ , in an impressive yield of 89%.<sup>71</sup>

The synthesis of the star-shaped Blatter-type tri-radical **13**, featuring three decoupled 1,2,4-benzotriazinyl units, each containing a delocalised electron, represents a significant advancement. This tri-radical exhibits enhanced thermal stability compared to the original Blatter radical, along with unique optical and electrochemical properties, making it a promising candidate for applications in spintronics and molecular electronics.<sup>71</sup>

### 1.3.2 Stability and Electronic Properties of Blatter-Type Tri-Radicals

One of the defining features of Blatter radicals is their stability. These radicals can remain stable for up to 30 years under normal conditions,<sup>73</sup> which makes them one of the most persistent organic radicals identified so far. This stability comes from the efficient delocalisation of the unpaired electron across the aromatic core, forming many resonance structures. This delocalisation reduces the reactivity of the unpaired electron, and in turn enhances the radical's resistance to degradation even in the presence of air and water. To improve stability further, Koutentis et al. added a trifluoromethyl group at the C7 position, creating a derivative that maintains stability even under strong oxidative conditions.<sup>59</sup> When classic Blatter radicals and this modified radical were exposed to oxidants like  $\text{MnO}_2$  or  $\text{KMnO}_4$ , the classic radicals converted to benzotriazinone over time, while the modified version retained its original structure. This modification highlights how structural adjustments can dramatically enhance the chemical stability of the Blatter radical and, because of that, the authors have given the name super stable. It is important to note that there was one case in which oxidative dimerization did occur and produced a new dimeric mono-radical.<sup>59</sup>

The electronic properties of the Blatter-type tri-radicals make them versatile for various technological applications. The conjugated structure of these radicals allows for easy tuning of their electronic and optical properties through structural modifications. An example is Kaszyński et al.,<sup>74</sup> who developed planarized Blatter radicals by incorporating sulphur or oxygen at the C8 position and a phenyl at the N1 position. These adjustments lead to an expansion of the  $\pi$ -conjugation, increasing the spin density of the benzene ring at the N1 position and, in turn, shifting the absorption to the near infrared region. These modifications allow for precise control over the electronic properties of Blatter radicals, making them suitable for use in devices such as photodetectors, molecular electronics and spintronic applications.<sup>75</sup>

Interestingly, unlike many radicals that typically do not emit light, certain Blatter radicals have demonstrated unexpected fluorescent properties. This unique feature, along with their great chemical stability and adjustable electronic characteristics, does allow them to be promising candidates for optoelectronic devices, where durable light-emitting materials are essential. The combination of these attributes highlights the potential for advanced applications in areas such as semiconductors, organic light-emitting diodes (OLEDs), and sensors.

### 1.3.3 Magnetism and Spin Properties of Blatter-Type Tri-Radicals

Blatter-type tri-radicals exhibit diverse magnetic properties that stem from the interactions between their unpaired electrons. Depending on the molecular configuration, these radicals can either display antiferromagnetic or ferromagnetic behaviour, which is the result of spin-spin interactions within the molecule.<sup>76</sup> Through strategic modification of substituents and aromatic bridges, it has been possible to develop materials that favour high-spin ground states, enhancing their suitability for a range of spintronic applications.

The ability of Blatter tri-radicals to possess high-spin ground states also makes them suitable for applications where spin alignment and polarisation are crucial. For example, changing the angle between the core benzotriazinyl and the aryl substituents at the N1 position can adjust how spins interact, allowing for custom magnetic properties.<sup>77</sup> This particular property is useful in developing spintronic devices, where the spin of the electrons can be manipulated to carry information, offering a new dimension for data processing and storage.

Similar to the mono-radical, the spin density of the tri-radical is primarily localised over the three benzotriazinyl units, with minimal delocalisation onto the central benzene. This localisation is further supported by the presence of three degenerate singly occupied molecular orbitals (SOMOs), each associated with one of the benzotriazinyl components. The minimal

interaction between these components underscores their independent character, reinforcing the tri-radical's stability and modular spin configuration.

The electrostatic surface potential (ESP) map (**Figure 1.11**) of the quartet ground state also reveals similarities with the mono Blatter radicals, strengthening the concept that the three benzotriazinyl arms act independently within the tri-radical framework. The independence is confirmed through the absence of significant spin-spin interactions across the arms of the star-shaped structure. These observations align with the findings of Koutentis et al., who also concluded that the quartet state is energetically favoured due to the consistent alignment of spins across the tri-radical.<sup>72</sup>

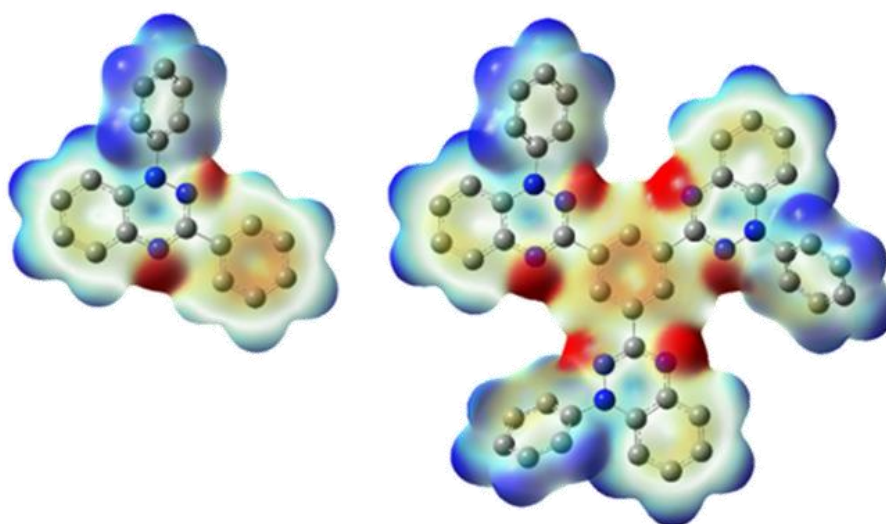


**Figure 1.11** Electrostatic surface potential map of the Blatter mono-radical **1** and tri-radical **13**. Zissimou et al. (2020).<sup>72</sup>

## 1.4 Significance of Blatter-Type Tri-Radicals in Spintronics

### 1.4.1 Potential Applications in Spintronics

Blatter-type radicals have shown promising performance when it comes to near infrared (NIR) photodetectors due to their extensive UV-Vis NIR absorbance range.<sup>78</sup> An example of this is

diradical **14** (**Figure 1.12**). which, when blended with [6,6]-phenyl C<sub>61</sub> butyric acid methyl ester (PCBM) in a 1:2 ratio, exhibits high responsivity and detectivity across wavelengths from 300 to 1200 nm.<sup>58</sup> This performance compares favourably with established silicon and InGaAs photodetectors, positioning Blatter-based materials as a viable option for flexible, low-cost photodetectors suited for wearable or mobile applications.

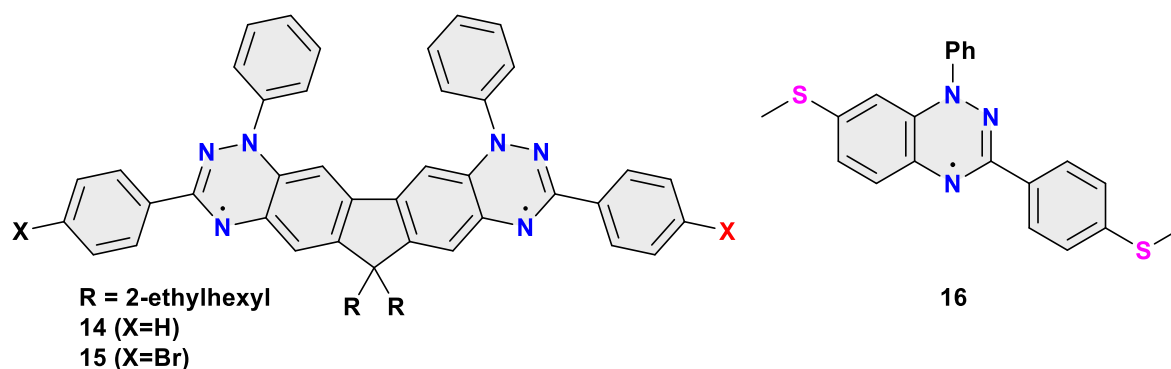


*Figure 1.12 Structure of Blatter-type radicals 14–16.*<sup>58</sup>

Blatter radicals have demonstrated some unique characteristics as spin carriers in organic field-effect transistors (OFETs).<sup>79</sup> This is observed in benzotriazine diradicals like **14** and **15**, that exhibit unusual self-doping behaviour, where reversible electron interactions between their open- and closed-shell states lead to the formation of radical anion-radical cation pairs. These pairs in turn impart p-type characteristics to OFETs, with adaptable hole mobility values sensitive to temperature and environmental factors. Furthermore, the addition of electron acceptors like 2,3,5,6-tetrafluoro-7,7,8,8-tetracyano-dimethane (F4TCNQ) can also enhance their performance by mimicking high-temperature effects, enabling controlled, reversible self-doping capabilities not achievable through traditional chemical doping.<sup>58</sup>

Blatter radicals are emerging as promising components for single-molecule spintronic devices. For instance, when interfaced with gold electrodes, Blatter radical **16** (**Figure 1.12**) has demonstrated remarkable stability in its open-shell configuration under ultra-high vacuum



conditions.<sup>80</sup> This preserves its radical properties, and studies indicate that the unpaired electrons in these radicals can interact with conducting electrons, leading to Kondo resonance,<sup>80</sup> a phenomenon in which localised spins interact with a sea of conduction electrons, resulting in an increase in electrical conductance at low temperatures. This resonance can be used to control single-molecule conductance, as observed through techniques such as atomic force microscopy (AFM) and scanning tunnelling microscopy (STM).<sup>81</sup>

Blatter radicals can also be applied as photoconductive liquid crystals. For instance, Kaszyński et al. synthesised benzo[e][1,2,4]triazinyl derivatives **17–20** (**Figure 1.13**), with **17** and **19** enabling photoinduced hole transport within specific temperature ranges.<sup>58</sup> These materials, which are responsive to environmental factors such as temperature,<sup>82</sup> offer new possibilities for tuneable photoconductive applications, expanding the potential use of Blatter radicals in responsive optical and electronic devices.

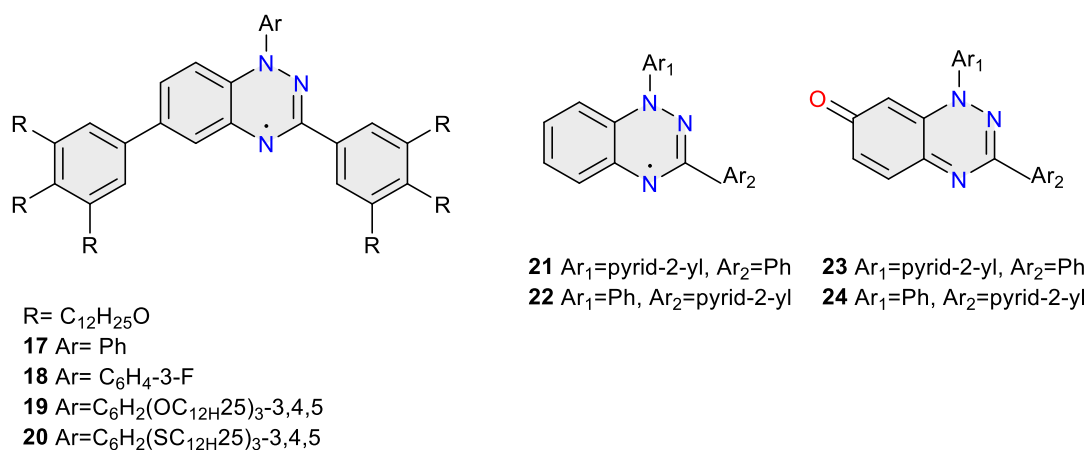


**Figure 1.13** Structure of Blatter-type radicals **17–22** and oxidation products **23** and **24**.<sup>58</sup>

In addition to their role in spintronics, Blatter radicals have shown promising applications in other fields due to their stable radical properties and reactivity. One notable example is their potential in anti-cancer therapy, where certain benzotriazinyl radicals have been investigated for cytotoxicity against cancer cell lines. Studies done by Aldabbagh et al.<sup>83</sup> found that

benzotriazinyl radicals, such as **21** and **22**, exhibited significantly lower cytotoxicity compared to their oxidation products, benzo[1,2,4]triazin-7-one derivatives (**23** and **24**). The introduction of pyridine groups was found to increase cytotoxic effects against certain cell lines, indicating that these radicals could be tuned for targeted cancer therapies.

Blatter radicals also show potential as pH sensors. Wudl et al. developed a stable pyrenotriazinyl radical, **25** (**Figure 1.14**), which exhibits high sensitivity to picric acid.<sup>84</sup> This radical undergoes a distinct colour change from purple to green in response to picric acid, detectable even at low concentrations. This colorimetric shift, which is caused by protonation of the radical, highlights the potential of the Blatter-type radicals for future chemical sensing applications.

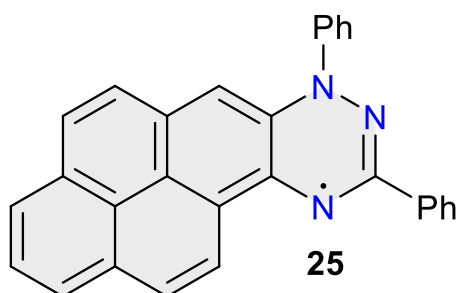


*Figure 1.14* Structure of Blatter-type radical **25**.<sup>58</sup>

Lastly, Blatter radicals can also be utilised to create stable, paramagnetic thin films without the need for metals. Casu et al. reported that radical **25** with its low vapour pressure and excellent film-forming properties,<sup>85</sup> maintains its paramagnetic properties under various conditions, indicating strong potential for use in organic molecular beam deposition (OMBD). This opens new pathways for Blatter radicals in magnetic applications requiring environmentally stable films, particularly for device interfaces in advanced electronic and spintronic technologies.

### 1.4.2 Advantages Over Conventional Spin Carriers

Blatter radicals feature a high degree of chemical and photostability, which makes them well-suited for devices that require reliable and long-term operation. Their capacity to maintain open-shell configurations without rapid degradation or loss of radical properties offers a significant advantage over many traditional organic molecules, which are often prone to instability.

Unlike conventional doped semiconductors, Blatter-type radicals exhibit reversible self-doping effects, allowing them to adapt their conductive properties in response to external conditions, such as temperature and the presence of electron acceptors.<sup>79</sup> This feature is particularly useful for applications in flexible electronics, where a dynamic response to environmental conditions is desired.

The unique combination of stability and tuneability in Blatter radicals, alongside their compatibility with low-cost, low-temperature, and solution-based processing, makes them highly favourable for integration into organic semiconductor devices.<sup>86–88</sup> Their structural flexibility enables them to be incorporated into a wide range of device architectures, from single-molecule junctions to thin films, broadening their applicability in advanced and spintronic technologies.

Blatter radicals have demonstrated stable paramagnetic properties in thin-film form, providing a metal-free option for magnetic thin-film applications. The ability to produce stable, paramagnetic organic films represents a significant advancement toward developing organic spintronic devices that do not rely on metal-based magnetic materials. This capability broadens the scope of spintronic applications and opens pathways for new device functionalities, enhancing the versatility of organic materials in magnetic and electronic technologies.

### 1.4.3 Additional Systems Relevant to this Thesis

During the course of this thesis, we became interested in exploring additional classes of Blatter-based polyradicals. This interest was sparked following a short research visit by the thesis author to the Koutentis group at the University of Cyprus. As a result, alongside the primary focus on Blatter tri-radicals, we conducted further investigations into other systems, illustrated in **Figure 1.15** (Pn = pnictogen). Systems **26a–28a** represent three isomeric variations of a potential Blatter radical fused with distinct dithiazole radical rings. Beyond these, we examined variations where the nitrogen atom in the dithiazole ring was substituted with phosphorus (**26b–28b**) and the sulphur atoms were replaced with phosphorus (**26c–28c**).

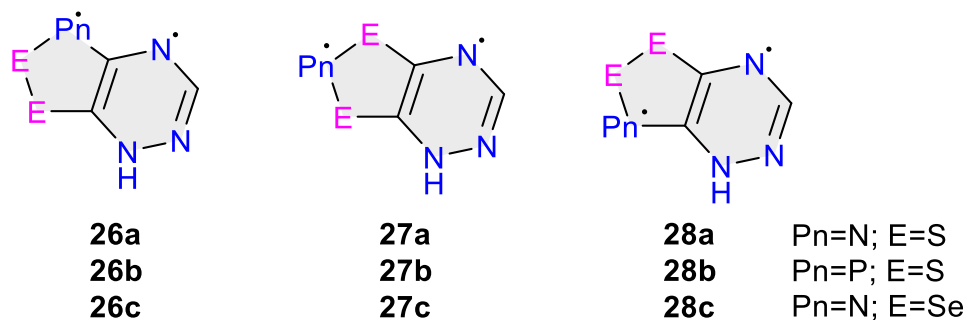


*Figure 1.15 Proposed diradical structures of the fused dithiazole-triazine systems 26–28.*

Finally, two other systems were also investigated, namely the aza-acene tri-radical (**29**) and a Blatter-type diradical taken from Schatz et al. (**30**),<sup>89</sup> the two compounds highlighted in **Figure 1.16**. These investigations broaden the scope of this thesis, offering insights into the diverse structural and electronic properties of Blatter-based radical systems.

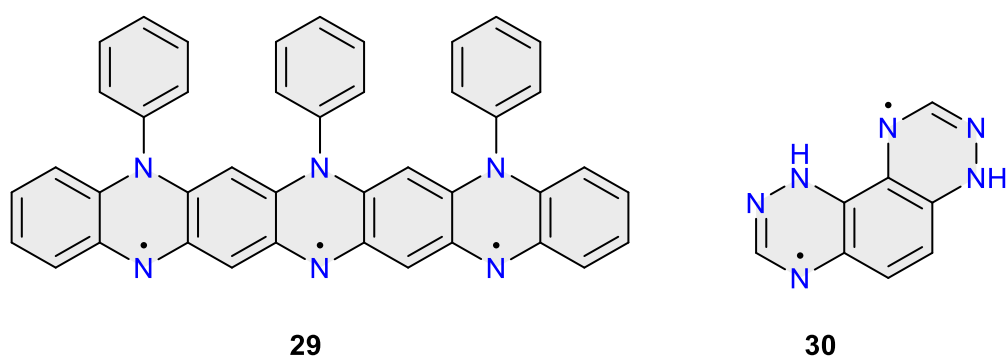


*Figure 1.16 Structures of the aza-acene compound 29 and the Schatz Blatter radical 30.<sup>89</sup>*

## 1.5 Relevant Computational Work

There has been some work on  $C_3$ -symmetrical Blatter-type triradicals, particularly from a computational perspective, but this remains a relatively underexplored area. A notable piece of work done by Zissimou et al. (2020) also combined a mixture of experiments and DFT calculations to calculate such a system. They confirmed the triradical showed a quartet ground state and calculated a very small energy gap between the doublet and quartet states ( $\Delta E_{D-Q} \approx 0.109$  kcal/mol) using the UB3LYP/6-31G(2d,p) level of theory.<sup>90</sup> However, their computational focus was molecule-specific and primarily was aimed at supporting experimental findings, rather than using computation to guide molecular design.

In contrast, the Ali group (Ali et al. 2023)<sup>91</sup> conducted a more rigorous computational study using a range of ab initio methods to improve the accuracy of doublet–quartet energy gaps. Acknowledging the limitations of traditional broken-symmetry DFT (BS-DFT), which tends to overestimate energy gaps, they implemented spin-constrained BS-DFT (CBS-DFT) and multireference methods such as CASSCF and NEVPT2. Their work demonstrated that computational chemistry could play a proactive role in designing new high-spin organic molecules.

This thesis takes a different approach by focussing on computational prediction as a primary tool going further than the molecule-specific focus from Zissimou et al. (2020) and building on the computational methods of Ali et al. (2023). Rather than interpreting known structures, this project systematically explores how structural variations, both at the central core and on the outer positions and how it influenced the spin states. By relying exclusively on computational approaches, this thesis hopes to address a clear gap in the literature and offers a more design-oriented framework for developing new triradicals. Doing this complements the earlier efforts stated and contributes to a deeper theoretical understanding when it comes to the relationship between the structural properties and  $C_3$ -symmetrical high spin systems.

## 1.6 Objectives of the Thesis

The primary objective of this thesis is to address critical gaps in our understanding of Blatter-type tri-radicals by investigating how geometric structure and substituent modifications influence their electronic properties, stability, and high-spin behaviour, particularly in maintaining robust spin states at room temperature. Blatter-type tri-radicals, with their unique physical properties—such as stability, antiferromagnetic and ferromagnetic interactions, and spin  $\pi$ -delocalisation—are promising candidates for advanced applications in materials science, electronics, and spintronics. However, existing research has primarily focused on their synthesis and basic characterisation, leaving many aspects of their electronic behaviour and practical potential unexplored.

One key knowledge gap lies in understanding how structural variations, such as changes in geometry and substituent groups, impact the electronic structure, doublet-quartet energy gap, and excited-state properties of these high-spin polyradicals. This gap has limited the rational design and optimisation of Blatter-type tri-radicals for practical spintronic applications.

Moreover, challenges in achieving stability and sustaining high-spin states at ambient conditions further restrict their use in device contexts.

This thesis aims to bridge these gaps through a comprehensive computational investigation of  $C_3$ -symmetrical Blatter-type tri-radicals. Using advanced methods—including density functional theory (DFT) and multi-reference approaches such as complete active space self-consistent field (CASSCF) and N-electron valence state perturbation theory (NEVPT2)—this thesis explores the effects of various geometric configurations and inner/outer substituent modifications on the electronic structure, ground-state multiplicity, and excited-state topology of these radicals. Expected outcomes include a deeper understanding of suitable DFT approaches for accurately describing these systems, identifying the factors that govern their stability and high-spin performance, and uncovering how various substituents influence critical properties, such as the doublet-quartet energy gap.

Ultimately, this research aims to establish fundamental design principles for Blatter-type tri-radicals, guiding the development of novel, high-performance organic polyradicals for real-world applications in spintronics and advanced magnetic devices. The insights gained will help pave the way for next-generation devices that utilise the spin properties of organic materials.

# Chapter

## 2. Theoretical Framework and Methodology

### 2.1 Density Functional Theory (DFT) Calculations

#### 2.1.1 Fundamentals of Density Functional Theory

Density Functional Theory (DFT) is a key foundation in computational quantum chemistry.<sup>92</sup>

Walter Kohn, who later won the Nobel Prize in Chemistry in 1998 for his development of DFT, significantly contributed to its advancement.

DFT provides an exact approach to the problem of electronic structure theory<sup>93</sup> by focussing on the electron density rather than the many body-wave function. This makes DFT a powerful tool and a computationally feasible method for studying the quantum state of atoms, molecules and solids, as well as for *ab initio* molecular dynamics.<sup>92</sup> Even with this, solving the electronic structure problem is inherently complex due to the need to simultaneously consider the interactions between the electrons and atomic nuclei.<sup>93–95</sup>

To address the complexity of this problem, the Born-Oppenheimer approximation can be used. The approximation was introduced by Max Born and J. Robert Oppenheimer in 1927, and it simplifies the problem by separating the motions of electrons and nuclei.<sup>96</sup> Within the Born-Oppenheimer approximation, the electronic energy,  $E_e[\rho(\mathbf{r})]$ , can be written as a functional of electron density:<sup>97</sup>

$$E_e[\rho(\mathbf{r})] = T[\rho(\mathbf{r})] + V_{en}[\rho(\mathbf{r})] + J[\rho(\mathbf{r})] + Q[\rho(\mathbf{r})]$$

Equation 1



In *Equation 1*,  $T[\rho(\mathbf{r})]$  represents the kinetic energy carried by the electrons  $V_{en}[\rho(\mathbf{r})]$  is the energy resulting from the attraction between the nuclei and the electrons,  $J[\rho(\mathbf{r})]$  describes the classical repulsion between electrons, and  $Q[\rho(\mathbf{r})]$  is the non-classical (quantum) electron–electron interaction energy. *Equation 2* and *Equation 3*, which express  $V_{en}[\rho(\mathbf{r})]$  and  $J[\rho(\mathbf{r})]$ , respectively, are shown below:

$$V_{en}[\rho(\mathbf{r})] = - \sum_{A=1}^n \int \frac{Z_A}{|\mathbf{r} - \mathbf{R}_A|} \rho(\mathbf{r}) d\mathbf{r}$$

*Equation 2*

$$J[\rho(\mathbf{r})] = 1/2 \iint \frac{\rho(\mathbf{r}_1)\rho(\mathbf{r}_2)}{r_{12}} d\mathbf{r}_1 d\mathbf{r}_2$$

*Equation 3*

DFT aims to formulate accurate approximations for the functionals for the kinetic energy  $T[\rho(\mathbf{r})]$  and the exchange-correlation energy  $Q[\rho(\mathbf{r})]$ . The kinetic energy poses the largest uncertainty in its accurate estimation. The Thomas-Fermi model, introduced in 1927,<sup>98</sup> provides an approximation for the kinetic energy, as shown in *Equation 4* below:<sup>98</sup>

$$T[\rho(\mathbf{r})] = \frac{3}{10} (3\pi^2)^{2/3} \int \rho(\mathbf{r})^{5/3} d\mathbf{r}$$

*Equation 4*

Developed soon after the establishment of quantum mechanics, the Thomas–Fermi model provides a simplistic and rough approximation for the kinetic energy functional  $T[\rho(\mathbf{r})]$ .<sup>92</sup> It serves as the simplest approach to  $T[\rho(\mathbf{r})]$ , being exact for an infinite uniform electron gas (UEG).<sup>97</sup> Despite its simplicity, efforts have been made to enhance it with gradient corrections and nonlocality. The Thomas–Fermi model remains most applicable to materials with nearly uniform densities, such as semiconductors and alloys, but it cannot properly describe

chemical bonds. Consequently, the development of precise kinetic energy functionals tailored for molecular systems remains a challenging task.

In the mid-1960s, Pierre Hohenberg, Walter Kohn and Lu Jeu Sham established a logically rigorous DFT of the quantum mechanical ground state. This development led to the introduction of an approximative explicit theory called the local-density approximation (LDA). The local-density approximation (LDA) for computations of the quantum ground state of many-particle systems proved to be superior to both the Hartree–Fock method, which is a wave function-based approach that approximates the wave function of a many-electron system as a single Slater determinant, and the Thomas–Fermi theory.<sup>92</sup> Kohn and Sham<sup>94</sup> successfully addressed the challenge of designing the kinetic energy functional for applications in molecular systems by demonstrating that it can be approximated using a single Slater determinant constructed from an set of orbitals  $\{\phi_i\}$ . This determinant represents a hypothetical system of non-interacting electrons that shares the same electron density as the exact many-body wave function. However, practical implementations that incorporate orbitals significantly increase the computational expense compared to orbital-free DFT (OF-DFT) approaches. However, Kohn–Sham DFT (KS-DFT)<sup>99–101</sup>, which is still fundamentally an exact theory, remains the most prevalent variant, with widespread applications in chemistry and physics.

In KS-DFT, the non-interacting kinetic energy obtained through the orbital approach does not correspond to  $T[p(\mathbf{r})]$ . The difference between these quantities is merged with  $Q[\rho(\mathbf{r})]$  to define the exchange-correlation energy,  $E_{xc}[p(\mathbf{r})]$ :

$$T_s[\{\phi_i\}] = -\frac{1}{2} \sum_{i=1}^n \int \phi_i^*(\mathbf{r}) \nabla^2 \phi_i(\mathbf{r}) d\mathbf{r}$$

*Equation 5*

$$E_{xc}[p(\mathbf{r})] = T[p(\mathbf{r})] - T_s[\{\phi_i\}] + Q[p(\mathbf{r})]$$

*Equation 6*

Here, the primary unknown term is the exchange-correlation functional, which is represented as a sum of an exchange functional  $E_x[p(\mathbf{r})]$  and the correlation functional  $E_c[p(\mathbf{r})]$ . From this point forward, KS-DFT and DFT will both be used to refer to Kohn-Sham density functional theory.

Developing density functionals is notably challenging due to them lacking systematic ways to improve, unlike the hierarchical progression observed in wavefunction theory. While wavefunction theory does allow for progressively refined models by adding more components, the same approach does not necessarily guarantee improvement across all the interactions in density functionals. To offer a general hierarchical conceptual map of DFT, John Perdew introduced the concept of Jacob’s Ladder,<sup>95,102</sup> which in the Bible refers to the ladder that Jacob dreams of, reaching from Earth to Heaven.<sup>103</sup> At the base of the ladder lies the “Hartree World”, where the exchange-correlation energy is zero. In this foundational level, electron-electron interactions are described exclusively by classical electrostatics, and can be denoted as  $J[p(\mathbf{r})]$ . As one progresses up the Jacob’s ladder, the approximations increase in sophistication, and components are then introduced to improve the modelling of  $E_{xc}$ . The framework offers a pathway for defining density functionals although it does lack the straightforward hierarchy found in wave function theory.

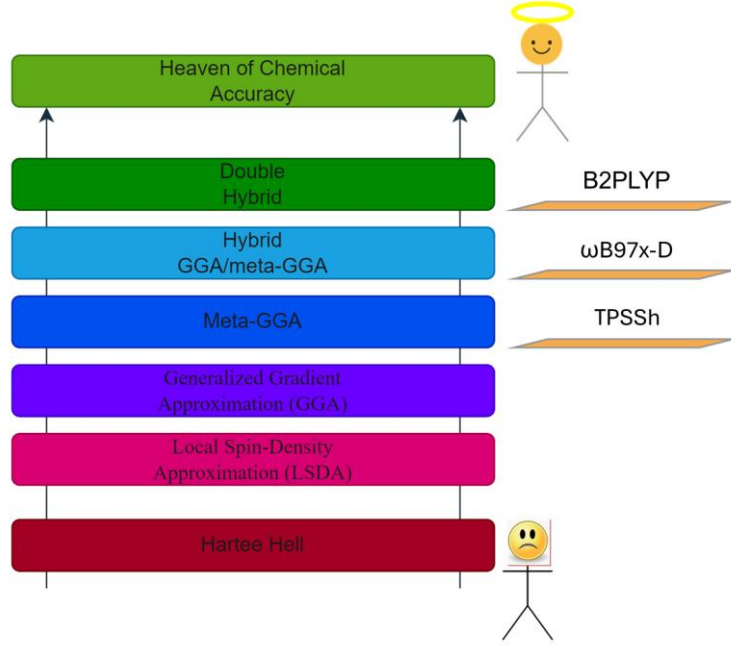


**Figure 2.1** Perdew's metaphorical Jacob's ladder highlights the five stages of exchange-correlation models in DFT, with each rung providing new physical depth and a step closer to better accuracy.

Jacob's ladder starts with the simplest exchange-correlation functionals, which are defined by their dependence solely on the electron density. This first level is known as the local spin-density approximation (LSDA). Although LSDA functionals are exact for an infinite uniform electron gas, they do fall short in accuracy when it comes to molecular properties due to the inhomogeneous density distributions which are typical of most real systems. The LSDA functional, which dates from work from John Slater and Paul Dirac, has an exact analytic form presented in *Equation 7*.<sup>97</sup>

$$E_x^{LSDA} = \sum_{\sigma}^{\alpha,\beta} \int e_{x,\alpha}^{UEG} d\mathbf{r} = -\frac{3}{2} \left(\frac{3}{4}\right)^{\frac{1}{3}} \sum_{\sigma}^{\alpha,\beta} \int P_{\sigma}^{\lambda/3} d\mathbf{r}$$

*Equation 7*

It is vital to improve on LSDA as it does not capture certain important physical effects accurately, such as the non-locality of exchange-correlation effects and the varying density gradients in

systems. This itself leads to inaccuracies in predicting properties like bond lengths, electronic band gaps and reaction energies.<sup>104,105</sup>

Moving up the Jacob's ladder, the generalised gradient approximation (GGA) occupies the second rung and is an improvement significantly on LSDA. The general form of the GGA exchange function is given below:

$$E_x^{GGA} = \sum_{\sigma}^{\alpha,\beta} \int e_{x,\sigma}^{UEG} g_{x,\sigma}^{GGA} d\mathbf{r}$$

*Equation 8*

The function  $g_{x,\sigma}^{GGA}$  enhances the exchange energy per unit volume  $e_{x,\sigma}^{UEG}$  in a UEG by serving as an inhomogeneity correction factor (ICF). Many forms of  $g_{x,\sigma}^{GGA}$  have been proposed over the years. One of the efforts to refine the LSDA with density gradient came from Frank Herman and his team in the late 1960s.<sup>106,107</sup> They introduced the  $X_{\alpha,\beta}$  exchange functional, which used the ICF  $g_{x,\sigma}^{GGA} = 1 + c_{x,1}x_{\sigma}^2$ , where  $x_{\sigma} = \frac{|\nabla p_{\sigma}|}{p_{\sigma}^{4/3}}$ . This dimensionless variable was derived through dimensional analysis and defined over the range  $[0,\infty)$ . Herman's approach improved atomic energy calculations by utilising the ICF, thereby refining the accuracy of calculations. However, the results produced excessively high numbers, necessitating cutoff values to simplify computations.

To address this problem, Becke introduced a suitable alternative to  $X_{\alpha}$  in 1986, given by  $u_{\alpha} = \frac{\gamma x_{\alpha}^2}{1 + \gamma x_{\alpha}^2}$ , with  $\gamma$  being a nonlinear parameter. Exchange functionals that utilise a simple ICF  $g_{x,\sigma}^{GGA} = 1 + c_{x,1}x_{\sigma}^2$  include B86 and PBE (Perdew–Burke–Ernzerhof).<sup>104,108</sup> Advancing this concept, Becke introduced a power series that led to the creation of the B97 density functional,<sup>109</sup> employing an exchange ICF which is expressed in *Equation 9*.

$$g_{x,\sigma}^{GGA}(u_\sigma) = \sum_{j=0}^N c_{x,j} u_\sigma^j$$

Equation 9

An ingredient that can increase the accuracy of density functionals is the kinetic energy density. The kinetic energy density, incorporated into numerous contemporary functionals, enhances the functional form's adaptability, facilitating both constraint satisfaction and a closer match to empirical data. Chemically speaking, kinetic energy density is particularly valuable for identifying electron delocalisation in molecules.<sup>110</sup> Functionals utilising this are in third rung of Jacob's Ladder, termed meta-generalised gradient approximations (meta-GGA). Typically, a meta-GGA exchange functional is defined by Equation 10 and Equation 11. A variable used in the dimensionless meta-GGA functionals is  $\alpha_\sigma = t_\sigma^{-1} - \frac{5}{3} s_\sigma^2$ . This variable quite effectively differentiates between various types of interactions like weak ( $\alpha \gg 1$ ), covalent ( $\alpha = 0$ ) and metallic ( $\alpha \approx 1$ ) bonds.

$$E_x^{mGGA} = \sum_{\sigma}^{\alpha,\beta} \int e_{x,\sigma}^{UEG} g_{x,\sigma}^{mGGA} d\mathbf{r}$$

Equation 10

$$g_{x,\sigma}^{mGGA}(w_\sigma, u_\sigma) = \sum_{i=0}^N \sum_{j=0}^N c_{x,ij} w_\sigma^i u_\sigma^j$$

Equation 11

Moving up Jacob's ladder to the fourth rung are hybrid GGA density functionals. Compared to meta-GGA, hybrid functionals are generally more accurate due to the inclusion of exact exchange. However, meta-GGA can still provide high improvements over most GGA functionals.<sup>111,112</sup> A drawback for hybrid GGA is that the computational cost is higher compared to meta-GGAs. Meta-GGA. Despite this they are preferred for many applications due to their

superior accuracy, while meta-GGA functionals often strike a balance between accuracy and computational efficiency.<sup>111,113</sup>

In 1993, Becke developed the first global hybrid functional,<sup>114</sup> B3PW91, by calibrating three linear parameters against 56 atomisation energies. A global hybrid functional is a type of density functional that mixes a fixed portion of exact exchange energy from Hartree-Fock theory with exchange-correlation energy from DFT across the entire system. B3PW91 can be represented by *Equation 12*:

$$E_{xc}^{B3PW91} = c_x E_x^{HF} + (1 - c_x - a_x) E_x^S + a_x E_x^{B88} + (1 - a_c) E_c^{PW92} + a_c E_c^{PW91}$$

*Equation 12*

where  $c_x = 0.2$ ,  $a_x = 0.72$ , and  $a_c = 0.81$ . For a boarder set of 124 atomisation energies, B3PW91 significantly decreases the mean absolute deviation (MAD) of BLYP by almost 2.5 times. GGAs typically feature an exact exchange mixing parameter between 15% and 20%. Among these, B3LYP is the most commonly used, incorporating a 20% exact exchange mixing parameter. B3LYP is similar to B3PW91 but uses VWN1RPA and LYP correlation functionals instead of PW92 and PW91.<sup>115</sup> Another notable three-parameter global hybrid GGA functional is B3P86, which modifies B3LYP by substituting the LYP correlation functional with P86.

The most popular non-empirical global hybrid GGA is PBE0,<sup>116</sup> which incorporates 25% exact exchange. Non-empirical global hybrid GGAs are constructed using theoretical constraints and principles which are derived from first principles considerations, such as UEG, scaling properties, or exact conditions for exchange-correlation energy.<sup>104,110</sup> Parameters in non-empirical functionals are determined without reference to experimental data, aiming to provide a more universally applicable and theoretically grounded approach.<sup>117</sup> The most popular semi-empirical global hybrid GGA after B3LYP is B97.<sup>109</sup>

Lastly, at the top of the ladder, the fifth rung is double hybrid (DH) functionals. Both DH and hybrid GGA approaches in computational chemistry aim to enhance the accuracy of electronic structure calculations beyond traditional pure density functionals. DH methods, such as those proposed by Stefan Grimme in 2006,<sup>118</sup> extend the concept of hybrid functionals by incorporating wave function expressions for electron correlation from second-order Møller–Plesset perturbation theory (MP2), in addition to exact exchange. These functionals typically include a higher fraction of exact exchange, which reduces self-interaction errors and improves accuracy.<sup>119</sup> While DH functionals provide a more comprehensive treatment of electron correlation, especially for systems with strong correlation effects or significant dispersion interactions, this comes at the cost of increased computational demands. An example of a DH functional is PBE0-2, with the general form shown in *Equation 13*.

$$E_{DH} = (1 - a)E_{DFT-x} + aE_{HF-x} + (1 - b)E_{DFT-c} + bE_{PT2-c}$$

*Equation 13*

In *Equation 13*,  $E_{DFT-x}$  and  $E_{DFT-c}$  are the exchange and correlation energies from a standard DFT functional, while  $E_{HF-x}$  is the HF exchange energy. The term  $E_{PT2-c}$  denotes the MP2 correlation energy, with  $a$  and  $b$  being empirical mixing parameters.<sup>104,113,118</sup>

Furthermore, PBE0-2 is a specific type of DH functional that builds on the PBE0 functional. PBE0 itself is a hybrid functional that combines PBE GGA with an exact percentage of HF exchange, as shown in *Equation 14*.

$$E_{PBE0} = 0.75E_{PBE-x} + 0.25E_{HF-x} + E_{PBE-c}$$

*Equation 14*

Building on *Equation 14*, PBE0-2 includes a portion of the MP2 correlation energy, making it a double hybrid, as shown below in *Equation 15*:



$$E_{PBE0-2} = 0.75E_{PBE-x} + 0.25E_{HF-x} + (1 - b)E_{PBE-c} + bE_{MP2-c}$$

Equation 15

with the number for  $b$  varying depending on the molecular system used.<sup>120</sup>

When discussing DFT, it is essential to address dispersion and its role in calculations. Dispersion interactions, also known as London dispersion forces or van der Waals (vdW) forces, are weak, long-range forces that arise from the correlated fluctuations in electron density in non-bonded atoms and molecules. These interactions are a type of intermolecular force that plays a crucial role in determining the physical properties and behaviours of molecular systems, particularly when those systems do not have ionic or covalent interactions.<sup>121,122</sup> The challenge of accounting for dispersion in DFT arises from the inadequacy of local and semi-local functionals. LDA and GGA fail to capture the dispersion forces adequately because they are not designed to account for the long-range electron correlations. GGAs, such as the PBE functional, only considers the local or semi-local electron density information, making them insufficient for describing long-range, non-local nature of dispersion interactions.<sup>93,94,123</sup>

One approach to solving this problem is to add an empirical dispersion correction term to DFT calculations. The most common empirical dispersion correction methods known as DFT-D methods, where the “D” stands for dispersion. A widely commonly used version is the Grimme DFT-D2 method.<sup>124</sup>

$$E_{disp} = -s_6 \sum_{i < j} \frac{C_6^{ij}}{R_{ij}^6} f_{damp}(R_{ij})$$

Equation 16

The terms in *Equation 16* are as follows:  $C_6^{ij}$  is the dispersion coefficient for atom pair  $i$  and  $j$ , and  $R_{ij}$  is the distance between the atoms  $i$  and  $j$ . The term  $s_6$  is the global scaling factor which

is specific to the functional used. The term  $f_{damp}(R_{ij})$  is the damping function, which avoids divergence at short distances.

There have been improvements on this functional since 2006 by Grimme. In 2010, Grimme et al. introduced the DFT-D3 method, which improves on the DFT-D2 method by providing a more sophisticated damping function and it also allows for anisotropic  $C_6$  coefficients which depend on the local chemical environment. Although the general form is very similar to the DFT-D2 the DFT-D3 has environment-dependent coefficients.<sup>125</sup>

$$E_{disp} = -s_6 \sum_{i < j} \frac{C_6^{ij}(R_{ij})}{R_{ij}^6} f_{damp}(R_{ij})$$

*Equation 17*

Further refinement was done by Grimme in 2011, focusing on a variant of DFT-D3 called DFT-D3(BJ). This variant incorporates a Becke-Johnson (BJ) damping function, which improves the accuracy of medium-range interactions.<sup>113</sup> Understanding and accurately modelling dispersion interactions are very important for predicting behaviour of molecular systems and materials, guiding the design of new materials and enhancing an overall comprehension of fundamental chemical processes.

Traditionally, DFT has been highly effective for closed shell-systems, where all the electrons are paired. The closed-shell DFT is based on the framework of Kohn and Sham, which maps interacting electron systems onto a non-interacting reference system with the same electron density.<sup>126</sup> The Kohn-Sham equation, shown in *Equation 18*.

$$\left[ -\frac{1}{2} \nabla^2 + V_{eff}(\mathbf{r}) \right] \psi_i(\mathbf{r}) = \epsilon_i \psi_i$$

*Equation 18*

With  $V_{eff}(\mathbf{r})$  being the effective potential, comprising the external potential, Hartree potential, and exchange-correlation potential, this approach is better in systems where electron pairs dominate, thus providing an accurate description of the ground-state properties.

However, a lot of interesting chemical and physical phenomena involve open-shell systems, in which the unpaired electrons play a crucial role. This leads us away from closed-shell to open-shell systems and into the realm of Spin-Flip Density Functional Theory (SF-DFT), a method specifically designed to handle these challenging open-shell cases.

Open-shell systems, characterised by having one or more unpaired electrons, require some special treatment. The unrestricted Hartree-Fock (UHF) method extends HF theory to handle open-shell systems by allowing different spatial orbitals for spin-up ( $\alpha$ ) and spin-down ( $\beta$ ) electrons. However, this approach can result in spin contamination, where the wave function deviates from being a pure spin state.<sup>126</sup> The treatment of  $\alpha$  and  $\beta$  electrons is described by *Equation 19* and *Equation 20*, respectively, which define the spatial orbitals for these spin states.

$$[-\frac{1}{2}\nabla^2 + V_{eff}^{\alpha}(r)]\psi_i^{\alpha}(\mathbf{r}) = \epsilon_i^{\alpha}\psi_i^{\alpha}$$

*Equation 19*

$$[-\frac{1}{2}\nabla^2 + V_{eff}^{\beta}(r)]\psi_i^{\beta}(\mathbf{r}) = \epsilon_i^{\beta}\psi_i^{\beta}$$

*Equation 20*

SF-DFT, as previously stated, is a solution for open shell systems, simultaneously reducing concerns about spin contamination. Proposed by Shao et al. in 2003,<sup>127</sup> SF-DFT operates by alternating the spin orientation of an electron of an excited state configuration relative to the predefined high-spin reference state. Through this approach, SF-DFT can effectively capture

multi-configurational character, which enables description on both the ground and excited states on a unified framework.

In SF-DFT, the Kohn–Sham determinant of a high-spin reference state serves as the foundation. This reference state enables SF-DFT to generate single excitations through manipulation of the spins of individual electrons. This approach is particularly beneficial for characterising systems such as diradicals, tri-radicals, and other multi-reference systems. Mathematically, SF-DFT can be expressed in *Equation 21*:

$$\mathcal{H}_{SF-DFT} = \mathcal{H}_{KS-DFT} + \mathcal{H}_{SF}$$

*Equation 21*

As shown above,  $\mathcal{H}_{KS-DFT}$  represents the Kohn–Sham Hamiltonian corresponding to the reference of the high-spin state, whereas  $\mathcal{H}_{SF}$  represents the spin-flip excitation operator. SF-DFT is very advantageous for systems where the electron correlation effects are significant and has multiple electronic configurations that contribute to the wave function.<sup>127</sup> Furthermore, SF-DFT can describe low-lying excited states and the ground state within the same theoretical framework, offering a unified approach to tackle open-shell systems.

### 2.1.2 The Gaussian 16 Software

Gaussian 16<sup>128</sup> is a widely used quantum chemical software package, renowned for its ability to perform advanced computational chemistry simulations. Building upon decades of development since the introduction of the Gaussian program by John Pople and his collaborators in the 1970s, Gaussian has evolved into a sophisticated tool for predicting molecular properties and exploring chemical systems. The program's design facilitates the study of molecules and reactions in various chemical environments, making it indispensable in both academic and industrial research.

The software implements a comprehensive range of quantum mechanical methods, including HF, post-HF, and DFT, allowing users to calculate molecular energies, optimise geometries, and predict vibrational frequencies with high accuracy. Gaussian 16 is particularly effective for studying electronic properties, reaction mechanisms, and transition states, enabling users to characterise intermediates and pathways in complex reactions. These capabilities are essential for systems that are experimentally challenging to access, such as high-energy intermediates or short-lived radicals.

A standout feature of Gaussian 16 is its ability to handle multi-reference systems, including diradicals, tri-radicals, and other open-shell configurations. SF-DFT and multi-configurational (or multi-reference) methods (vide infra) available in the software facilitate accurate treatment of these systems, providing key information into their electronic structures. This is particularly useful for studying reactive species, excited states, and photochemical processes. The program also supports the analysis of molecular orbitals, electron density distributions, and other properties.

Gaussian 16 was employed in this thesis for all DFT calculations, utilising a spin-flip, broken-symmetry (BS) approach to accurately model the polyradicals studied.

## 2.2 Post-Hartree–Fock Calculations

### 2.2.1 Fundamentals of Post-Hartree–Fock Methods

HF theory has significantly advanced simulation methods in computational chemistry, providing a foundational framework for approximating molecular wave functions. However, the simplifications inherent in HF, particularly regarding electron correlation, often render it inadequate for accurately capturing complex physical phenomena. These shortcomings can be addressed through more sophisticated methods, collectively known as post-HF approaches,

which incorporate electron correlation effects with greater rigor. While these methods offer enhanced accuracy, their increased computational demands typically limit their application to smaller systems.

Three common post-HF methods are coupled cluster (CC), MP2, and configuration interaction (CI). The CC method extends HF theory by constructing multi-electron wavefunctions using an exponential cluster operator  $T$ . This operator generates the total wavefunction  $|\Psi\rangle$  of the system as:<sup>129–131</sup>

$$|\Psi\rangle = e^T |\phi_0\rangle$$

*Equation 22*

Where  $|\phi_0\rangle$  represents the Slater determinant derived from the HF method, serving as the reference wave function. The operator  $T$  generates excited Slater determinates by including single ( $T_1$ ), double ( $T_2$ ), and higher-order excitations. CC methods vary in accuracy depending on the level of excitations considered, with common approaches including CCS (coupled cluster with single excitations), CCSD (coupled cluster with single and double excitations), and CCSDT (coupled cluster with single, double, and triple excitations). While CCSDT offers higher accuracy, it comes at a significantly increased computational cost.

One of the most widely used CC methods is CCSD(T), which stands for coupled cluster with single and double excitations augmented by a perturbative treatment of triple excitations. Often referred to as the "gold standard" of quantum chemistry, CCSD(T) strikes an excellent balance between computational efficiency and accuracy, making it a popular choice for high-accuracy calculations of molecular properties and reaction energies. The perturbative inclusion of triple excitations significantly improves the accuracy compared to CCSD, capturing essential electron correlation effects at a fraction of the cost of full CCSDT.

A key advantage of CC methods, including CCSD(T), is their size-extensivity and size-consistency. Size-extensivity refers to a method's ability to ensure that the total energy of a system scales correctly with the number of particles (e.g. electrons or nuclei) in the system. For example, if a molecule is doubled in size (such as by combining two identical, non-interacting subsystems), the total energy calculated by the method should also double. This property is essential for accurately describing extensive properties and for studying large or multi-component systems. Size-consistency, on the other hand, ensures that the energy of a system composed of two or more non-interacting fragments is equal to the sum of the energies of the individual fragments calculated separately. For instance, in the case of two molecules far apart with no interaction, the total energy of the combined system should precisely match the sum of the energies of each molecule individually. This property is crucial for accurately modelling dissociation processes and non-interacting systems. CCSD(T), being both size-extensive and size-consistent, provides reliable and consistent results for systems ranging from small molecules to larger clusters, making it an indispensable tool in computational chemistry.

Møller–Plesset (MP) perturbation theory improves upon the HF theory by incorporating electron correlation effects through Rayleigh–Schrödinger perturbation theory.<sup>132,133</sup> It introduces a perturbed Hamiltonian  $H$  comprising the unperturbed Hamiltonian  $H_0$  and a perturbation  $V$ . The HF determinant serves as the zero-order wavefunction, forming the foundation for successive corrections to the energy.

The second-order correction, MP2, is particularly significant as it captures 80-90% of the total correlation energy, offering a substantial improvement over HF while maintaining reasonable computational demands. Higher-order corrections, such as MP3 and MP4, provide increased accuracy but at the cost of greater computational expense, with their convergence behaviour depending on the system's complexity and the choice of basis set. Among these methods, MP2 is the most widely adopted for practical studies of electron correlation, offering a favourable

balance between accuracy and computational cost, particularly when moderate-sized basis sets are used.

Lastly, CI improves upon the HF method by expanding the wavefunction beyond a single Slater determinant. It achieves this by representing the wavefunction as a linear combination of multiple determinants, allowing a more accurate treatment of electron correlation. These determinants are constructed by introducing excitations from the HF reference state using  $N$ -electron basis functions, thereby accounting for a broader range of electron configurations.

CI can focus on specific types of excitations, such as double excitations (CID), or include both single and double excitations (CISD), depending on the desired balance between computational efficiency and accuracy. While CI methods provide a systematic framework for capturing electron correlation, they are computationally demanding, especially for large systems, as the number of determinants grows combinatorically with the system size. Nonetheless, CI remains a benchmark for testing and validating other methods due to its rigorous treatment of electron correlation.

### 2.2.2 Complete Active Space Self-Consistent Field (CASSCF) Calculations

The complete active space self-consistent field (CASSCF) method is a cornerstone in quantum chemistry for accurately modelling the electronic structure of molecules, particularly those requiring a multiconfigurational or multireference description. Unlike single-reference methods, which rely on a single electronic configuration to describe a system, CASSCF captures the complexities of systems where multiple electronic configurations contribute significantly to the wavefunction. This multireference nature is crucial for accurately describing phenomena such as bond dissociation, excited states, and diradical or polyradical systems, where a single configuration fails to capture the electronic interactions adequately.



The method relies on three key concepts: active space selection, wavefunction optimisation, and electron correlation.

The active space represents a carefully chosen subset of molecular orbitals that are most significant for describing the electronic states of a molecule. This subset typically includes orbitals involved in bonding, anti-bonding, and crucial electronic excitations. Selecting the appropriate active space is critical, as it determines the accuracy of the calculation. However, increasing the size of the active space significantly raises computational demands.<sup>134</sup> Balancing these factors is essential for capturing the most relevant electronic interactions while maintaining computational feasibility.

Wavefunction optimisation in CASSCF enhances the modelling of complex molecular systems by simultaneously optimising the orbital shapes and the electronic configurations that describe their interactions. This dual optimisation ensures a highly accurate depiction of electronic states, particularly for systems where single-configuration approximations fail.<sup>135</sup>

The third pillar of CASSCF is electron correlation, which encompasses both static and dynamic correlation. Static correlation addresses situations where a single electronic configuration is insufficient to describe the system, while dynamic correlation captures the instantaneous interactions between electrons. CASSCF excels in modelling static correlation, making it suitable for systems with multiple near-degenerate configurations. However, dynamic correlation is better handled by complementary methods.

To incorporate dynamic correlation, second-order N-electron valence state perturbation theory (NEVPT2)<sup>136</sup> is often employed alongside CASSCF. NEVPT2 refines the electronic structure calculations by accurately accounting for dynamic electron correlation, which involves the short-range, time-dependent interactions between electrons as they respond to each other and

to nuclei. This step is critical for capturing the subtle repulsions between electrons that simpler methods often miss.

Both CASSCF and NEVPT2 are implemented in ORCA,<sup>137</sup> a versatile computational chemistry software. In this thesis, ORCA was used to combine these techniques for a detailed and precise characterisation of complex systems, such as Blatter tri-radicals. This integrated approach provided comprehensive insights into their electronic structures and properties, highlighting the strength of these advanced computational methods.

### 2.2.3 The Orca 5 Software

ORCA is a versatile quantum chemistry software package developed and maintained by Frank Neese at the Max Planck Institute for Chemical Energy Conversion. Offered as freeware for academic users, ORCA has become one of the most widely used tools in the field, with over 40,000 registered academic users globally. Its extensive capabilities encompass electronic structure calculations, molecular properties, and multilevel modelling, making it an indispensable tool for researchers in both academia and industry. Additionally, ORCA is commercially distributed to industrial users through FAccTs, ensuring its availability across diverse research domains.

The fifth iteration of the program, ORCA 5, was released in July 2021, bringing significant advancements in numerical efficiency, enhanced user-friendliness, and expanded functionality. These enhancements are underpinned by the integration of the SHARK engine, which optimises integral calculations and task handling, leading to significant speedups across various quantum chemical methods. This version also includes redesigned numerical grids and improved algorithms for DFT, hybrid, and DH functionals, further solidifying ORCA's reputation as a state-of-the-art computational tool.

ORCA's capabilities in multireference calculations make it a powerful tool for studying complex electronic structures, particularly in magnetic systems and strongly correlated molecules. Version 5 introduced significant advancements, including the CASPT2-K method, which is intruder-state-free and eliminates empirical parameters, and reformulated CASPT2 and NEVPT2 approaches, achieving speedups of up to two orders of magnitude for large active spaces. The linear-scaling DLPNO-NEVPT2 (vide infra) implementation enables efficient treatment of large systems, while the expanded ab initio ligand field theory (AILFT) module allows detailed parameterisation of transition metal complexes, bridging theory and experiment. These features, combined with iterative configuration expansion (ICE) methods for approximate full-CI results, position ORCA as a leading platform for tackling the most challenging problems in quantum chemistry with accuracy and efficiency. As a free, user-friendly, and continually evolving platform, ORCA not only supports the scientific community but also drives innovation, making it a cornerstone in the field of computational chemistry.

All post-HF calculations conducted in this thesis were performed using the ORCA quantum chemistry program.<sup>138</sup> The decision to employ two different software packages for the main parts of the calculations was driven by multiple considerations. Firstly, it allowed us to utilise each program for its specific strengths, ensuring that the methodologies applied were optimised for their respective computational tasks. Secondly, and equally important, this approach provided the thesis author with the opportunity to explore and gain hands-on experience with different quantum chemistry software tools.

## 2.3 Computational Details

A brief overview of the computational details is provided here, with more specific information detailed in the following sections. To begin, a benchmark investigation of DFT functionals was

conducted to optimise the geometries of Blatter radicals at their ground-state multiplicities. Two radicals, **4** (mono-radical, doublet state) and **13** (tri-radical, quartet state), were selected, and their optimised geometries were compared with experimental data. Vibrational harmonic frequencies confirmed that the optimised structures are minima on the corresponding potential energy surfaces.

Section 2.3.1 provides details on the selected molecules, section 2.3.2 discusses the functional selection, and section 2.3.3 covers the basis set choices. For systems containing sulphur and selenium, custom basis sets were used (section 2.3.4). All DFT calculations included empirical dispersion corrections (section 2.3.5).

Doublet-quartet (D–Q) energy gaps for Blatter tri-radicals and singlet-triplet gaps for additional biradicals were determined via single-point energy calculations. Spin-contamination corrections were included and are further described in section 2.3.6. To identify the optimal DFT method for these calculations, a second benchmark compared DFT results with NEVPT2/CASSCF energy gaps, employing the domain-based local pair natural orbital (DLPNO)<sup>139</sup> approach for efficient multireference calculations and the resolution of the identity for Coulomb and chain of spheres for exchange (RIJCOSX)<sup>140,141</sup> approximation to accelerate integral evaluation.

Solvation effects were included in single-point calculations using the implicit solvation model based on density (SMD)<sup>142</sup> and the self-consistent reaction field (SCRF) framework, with the integral equation formalism polarised continuum model (IEFPCM)<sup>143</sup> implemented in Gaussian 16 to simulate dichloromethane (DCM,  $\epsilon = 8.93$ ) as the solvent.

The criteria for performing the benchmark for the geometry optimisation calculations is described in section 2.3.7. All DFT calculations were performed in Gaussian 16, while

multireference calculations were conducted in ORCA 5<sup>138</sup>. Molecular structures were visualised using ChemCraft,<sup>144</sup> and all other plots were created in Python via VS Code.<sup>145</sup>

### 2.3.1 Selection of Molecules

A comprehensive list of the Blatter tri-radicals examined in this study is presented in **Figure 2.2**. These systems are categorised into two primary groups based on the substitution patterns. The first group focuses on "outer" substitutions, where the inner Ph ring retains hydrogen atoms at the Y positions, while the X substituents vary across two subclasses: the "halide" series and the "EWG/EDG" series. It is important to note that, despite being termed "halide," this subclass only includes halomethyl substituents, as the differences among pure halides were minimal and thus excluded from the discussion. Conversely, the "EWG/EDG" series encompasses all other electron-withdrawing group (EWG) and electron-donating group (EDG) substituents.

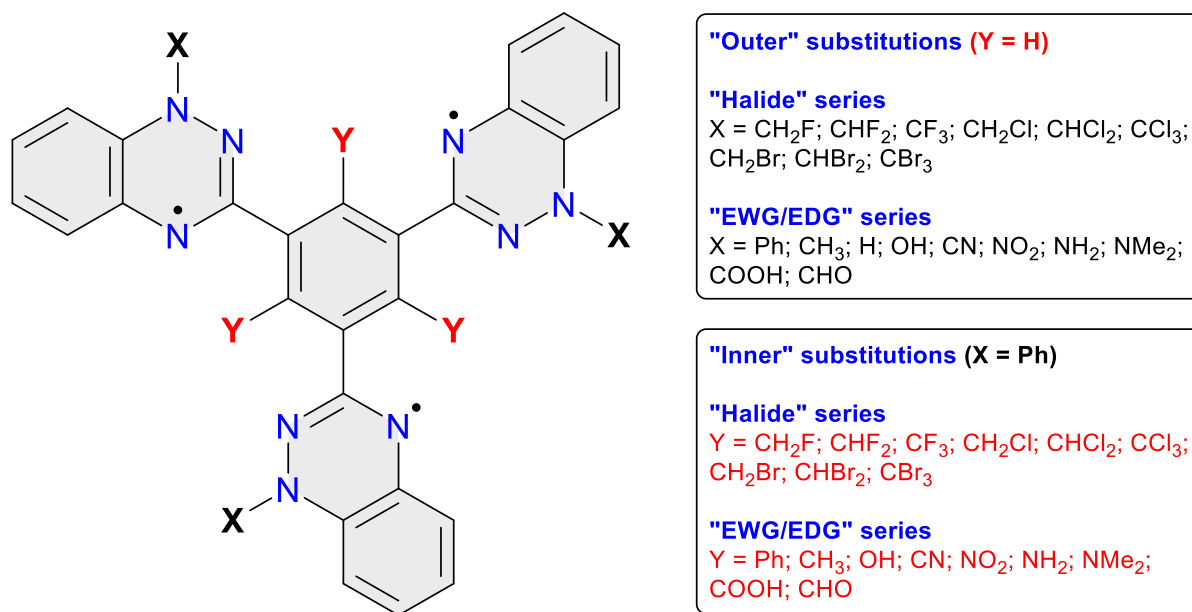


**Figure 2.2** List of Blatter tri-radicals investigated in this thesis. This is the first study that changes molecules in the X and Y position.

The second group addresses "inner" substitutions, where X substituents on the triazine rings are fixed as Ph groups, and the Y substituents vary according to the same two subclasses (halide and EWG/EDG), naturally excluding Y = H. This classification allows for a systematic investigation of the electronic and steric effects of substituents at distinct positions within the Blatter tri-radicals.

In addition to these tri-systems, calculations were also performed on the original Blatter radical (**4**) and systems **26–30**, as depicted in Figures **1.15** and **1.16**. These additional systems provided further context and enriched the understanding of the chemical and electronic properties explored in this study.

### 2.3.2 Selection of Functionals

The selection of functionals for this thesis encompasses a diverse range of methodologies to ensure robust calculations across different chemical systems. The functionals used are classified as follows:

- Hybrid: PW6B95D3,<sup>146,147</sup> B3PW91,<sup>148</sup> PBE0 (written in Gaussian 16 as PBE1PBE),<sup>149</sup> M06-2X,<sup>147</sup> BP86,<sup>150</sup> B3LYP,<sup>151</sup>  $\omega$ B97X-D,<sup>152</sup> M06HF.<sup>153</sup>
- Meta-GGA: MN15,<sup>154</sup> TPSSh.<sup>155</sup>

Among these, MN15, a meta-hybrid GGA functional, is particularly noteworthy for its balance of accuracy and computational efficiency, making it suitable for capturing electron correlation effects. The mathematical formulation of this functional is provided in *Equation 23*.

$$E_{xc}^{MN15} = \frac{X}{100} E_x^{HF} + E_{nxc} + E_c$$

*Equation 23*

The term  $E_X^{HF}$  is the nonlocal HF exchange energy computed from the Kohn–Sham orbitals, where  $X$  denotes the percentage of HF exchange. The  $E_{nxc}$  term refers to the non-separable local exchange-correlation energy. Lastly,  $E_c$  accounts for the additional correlation energy.<sup>156</sup> Another example of functional used is the hybrid, long-range corrected functional  $\omega$ B97X-D. Its mathematical formulation is provided in *Equation 24*.

$$E_{\omega B97X-D} = E_X^{B97} + E_C^{LYP} - \sum_{i<j} \frac{C_6^{ij}}{R_{ij}^6} \frac{1}{1 + e^{-d(R_{ij}/R_0-1)}}$$

*Equation 24*

The first term is the exchange energy  $E_X^{B97}$  from the Becke 97 functional, with its purpose to account for the repulsive part of the exchange interaction between electrons.<sup>109</sup> Following this, the correlation energy  $E_C^{LYP}$  from Lee, Yang and Parr (LYP: Lee–Yang–Parr) functional is introduced, serving to address the attractive part of the correlation interaction between electrons.<sup>157</sup> Next, the functional incorporates the dispersion energy with damping, represented by the term  $\sum_{i<j} \frac{C_6^{ij}}{R_{ij}^6}$ . This term sums over all pairs of atoms  $i$  and  $j$ , calculating the dispersion interaction between them based on the interatomic distances  $R_{ij}$ . To prevent overestimation of dispersion forces at short distances, a damping function,  $\frac{1}{1+e^{-d(R_{ij}/R_0-1)}}$ , is applied. Here,  $d$  controls the steepness of the damping, and  $R_0$  represents the reference distance. This component ensures proper treatment of vdW interactions while avoiding singularities.<sup>149,158</sup>

Another DFT functional used is TPSSh.<sup>155</sup> This functional is known for its inclusion of kinetic energy density as an additional variable to improve the description of exchange-correlation effects. The mathematical formulation of TPSSh is provided in *Equation 25*:

$$E_{TPSSh} = aE_{HF} + (1 - a)E_{XC}^{TPSS}$$

*Equation 25*

Here,  $E_{HF}$  represents the HF exchange energy,  $E_{XC}^{TPSS}$  is the exchange-correlation energy derived from the Tao-Perdew-Staroverov-Scuseria (TPSS)<sup>155</sup> functional, and  $a$  is the mixing coefficient. This functional aims to provide a balanced and accurate description of correlation and exchange effects, specifically for inhomogeneous electron systems.<sup>159–161</sup>

### 2.3.3 Basis Sets

The thesis utilised two basis sets from the def2 family: def2-SVP (split valence polarised) and def2-TZVPP (triple-zeta with two sets of polarisation).

The def2-SVP basis set, developed by Weigend and Ahlrichs, is designed to balance computational efficiency with accuracy. It incorporates polarisation functions, enabling a flexible and more realistic description of the electron distribution compared to minimal or standard split-valence basis sets. This makes def2-SVP particularly suitable for studying medium-sized molecules, where computational resources may be limited. It offers significant improvements over simpler basis sets without demanding excessive computational resources, making it a practical choice for initial explorations and geometry optimisations.<sup>162</sup>

In contrast, the def2-TZVPP basis set, also from the def2 family, provides a higher level of accuracy by including triple-zeta functions for valence electrons along with polarisation functions on all atoms. This basis set is ideal for detailed quantum chemical calculations, especially for large molecules or systems where precise electronic structure data is essential. However, its enhanced accuracy comes with increased computational cost, requiring significantly more time and resources to complete calculations.<sup>162,163</sup>

In this thesis, def2-SVP was selected for geometry optimisations due to its computational efficiency, allowing the exploration of molecular structures within a reasonable timeframe. For single-point energy calculations, def2-TZVPP was employed to achieve the high accuracy



required for describing the electronic properties of the radicals. However, due to the computational intensity of def2-TZVPP, it was not utilised for optimising the radicals, ensuring a balanced use of computational resources while maintaining accuracy where it was most critical.

#### 2.3.4 Custom Basis Sets for Selenium and Sulphur Systems

Singlet-triplet energy gap calculations for selenium- and sulphur-containing compounds required the use of tailored basis sets to ensure accurate results. The def2-SVPD basis set, which includes diffuse functions to better account for the delocalised electron density of these elements, was selected for this purpose. As the def2-SVPD basis set is not natively implemented in Gaussian 16, the Basis Set Exchange<sup>164</sup> platform was utilised to generate a mixed basis set. This approach allowed the incorporation of diffuse functions into the def2-SVP framework, ensuring reliable geometry optimisations and energy gap calculations for selenium- and sulphur-containing molecules.

#### 2.3.5 Inclusion of Empirical Dispersion

Empirical dispersion corrections, specifically Grimme's D3 and D3(BJ) methods, were incorporated into the calculations for this thesis to improve the accuracy of quantum chemical simulations. These methods are designed to address the dispersion interactions that standard DFT often fails to capture, thereby enhancing the treatment of vdW forces and non-covalent interactions.

As discussed before, the D3 method, developed by Grimme, is a widely adopted approach that adds dispersion corrections to DFT calculations, improving predictions of molecular

geometries and interaction energies. The D3(BJ) variant further refines these corrections by introducing Becke-Johnson damping, which mitigates errors in short-range interactions, leading to more accurate and reliable results for molecular properties and energetics.

In this thesis, the D3(BJ) correction was employed for geometry optimisation and single-point calculations performed with the PBE0 functional. Additionally, single-point calculations using the B3PW91 functional also utilised the D3(BJ) correction, ensuring a consistent and accurate treatment of dispersion effects throughout the study.

### 2.3.6 Spin Contamination

The correction factor used to account for spin contamination in the Gaussian calculations associated with the calculation of the doublet-quartet energy gap,  $\Delta E_{DQ}$ , is defined in *Equation 26*:

$$\Delta E_{DQ} = \frac{\langle S^2 \rangle_{HS} - 0.75}{\langle S^2 \rangle_{HS} - \langle S^2 \rangle_{BS}} (E_{BS} - E_{HS})$$

*Equation 26*

where  $E_{BS}$  represents the energy of the broken symmetry state, which corresponds to the doublet state, while  $E_{HS}$  refers to the high-spin state which in this case is a quartet state. The total spin operator for the doublet state holds a value of 0.75, while for the quartet state, it is 3.75. In this equation  $\Delta E_{DQ}$  signifies the corrected energy gap. In the expression,  $\langle S^2 \rangle_{HS}$  and  $\langle S^2 \rangle_{BS}$  account for the computed expected value of the total spin operator  $\langle S^2 \rangle$  for the states. In cases involving singlet and triplet states, corresponding singlet-triplet energy gap,  $\Delta E_{ST}$ ,  $E_{BS}$  and  $\langle S^2 \rangle_{BS}$  correspond to the open-shell singlet state, while  $E_{HS}$  and  $\langle S^2 \rangle_{HS}$  are related to the triplet state.

### 2.3.7 Criteria for Geometry Benchmarking

To benchmark geometries, the root-mean-square deviation (RMSD) of the computed structures was calculated using different functionals, with the crystal structure of the Blatter mono-radical **1** and tri-radical **13** serving as references. The RMSD quantifies the average deviation between corresponding atomic positions in two molecular structures and is a critical metric for assessing the accuracy of computed geometries. The RMSD is calculated as:

$$RMSD = \sqrt{\frac{1}{N} \sum_{i=1}^N (d_i)^2}$$

*Equation 27*

where  $N$  is the number of atoms in the molecule, and  $d_i$  represents the distance between the  $i$ -th atom in the two structures being compared.

The ChemCraft<sup>144</sup> software utility was used for these calculations, which involves comparing two molecular structures side by side. First, two instances of ChemCraft<sup>144</sup> are launched, and the reference crystal structure and computed geometry are loaded into separate windows. The structures must have identical atomic sequences; if not, the atoms in one structure must be manually reordered to match. This can be accomplished using the "Edit/Update sequence by atomic labels" feature in ChemCraft.<sup>144</sup>

Once the structures are prepared, the "Tools/RMS compare structures" option is selected to compute the RMSD. The utility displays minimised atomic distances in a table, along with RMSD values calculated for different atom types and for all atoms combined. If required, weights can be assigned to individual atoms using the "Use custom weights" option, allowing specific atoms to contribute more or less to the RMSD calculation.

The RMSD values provide a quantitative assessment of how well the computed structures align with the reference crystal structure. For example, the "All atoms" RMSD gives an overall measure of structural agreement, while RMSDs for individual atom types highlight specific areas of deviation. This approach ensures a thorough evaluation of the computed geometries and validates the performance of the selected functionals.

Using this methodology, the geometric benchmarks revealed how well the chosen functionals could reproduce the experimentally determined geometry of the Blatter tri-radical systems. The results offered a way into assessing the accuracy of the computational methods applied in this thesis and selecting the best one for geometry optimisations.

The benchmarking process involved evaluating the Blatter mono-radical **1** and the Blatter tri-radical **13**. Crystal structures for both systems were obtained from the Cambridge Crystallographic Data Centre (CCDC).<sup>165</sup> The structures were then edited using the Avogadro molecular editor to isolate the corresponding monomers for further analysis.

To determine the most suitable functional for accurate mono-radical and tri-radical calculations, five different functionals were applied to the monomers. The performance of each functional was assessed using root-mean-square deviation (RMSD) comparisons between the computed and experimental geometries. In these comparisons, hydrogen atoms were excluded from the RMSD calculations as their positions had negligible influence on the overall structural differences. This approach ensured that the analysis focused on the key structural features of the molecules.

# Chapter

## 3. Results and Discussion

This chapter provides a comprehensive analysis of the structural properties and electronic behaviour of Blatter tri-radicals associated with compound **13** and related systems, including fused dithiazole-triazine diradicals **26–28**, the aza-acene tri-radical **29**, and the Blatter-type Schatz diradical **30**. The focus is on examining the effects of various substituents and their influence on molecular geometry, spin states, and energy gaps. The first section investigates the structural effects of outer and inner substitutions on the Blatter tri-radicals, comparing halide-substituted and electron-donating/electron-withdrawing groups. A comprehensive geometry benchmark analysis is conducted, revealing trends in planarity, bond lengths, and steric effects, with findings visualised through optimised 3D structures. The chapter also examines the D–Q energy gaps for these systems, highlighting how substituents influence spin-state stability.

Subsequently, the focus shifts to singlet-triplet energy gaps in potential phenyl-substituted dithiazole-triazine diradicals. This analysis explores the effects of the dithiazole ring structure, selenium and phosphorus substitutions, and the incorporation of functional groups like CN and OCH<sub>3</sub>, to verify if these systems can indeed be labelled as diradicals. Trends in singlet stability are identified, illustrating the effects of electronic and steric factors on molecular properties. Finally, we analyse the aza-acene tri-radical and the Blatter-type Schatz diradical. Together,

these results provide a thorough understanding of how structural modifications affect the electronic characteristics and stability of these radical systems.

### 3.1 Blatter Tri-Radicals: Structural Analysis

#### 3.1.1 Structural Benchmark

We begin this section by presenting the results of the geometry benchmark analysis. illustrates the RMSD values for the Blatter mono-radical **1** using five different functionals, namely B3LYP, BP86, M06-2X, PBE0, and  $\omega$ B97X-D. In turn, **Figure 3.2** shows the values for Koutentis' tri-radical system **13**.

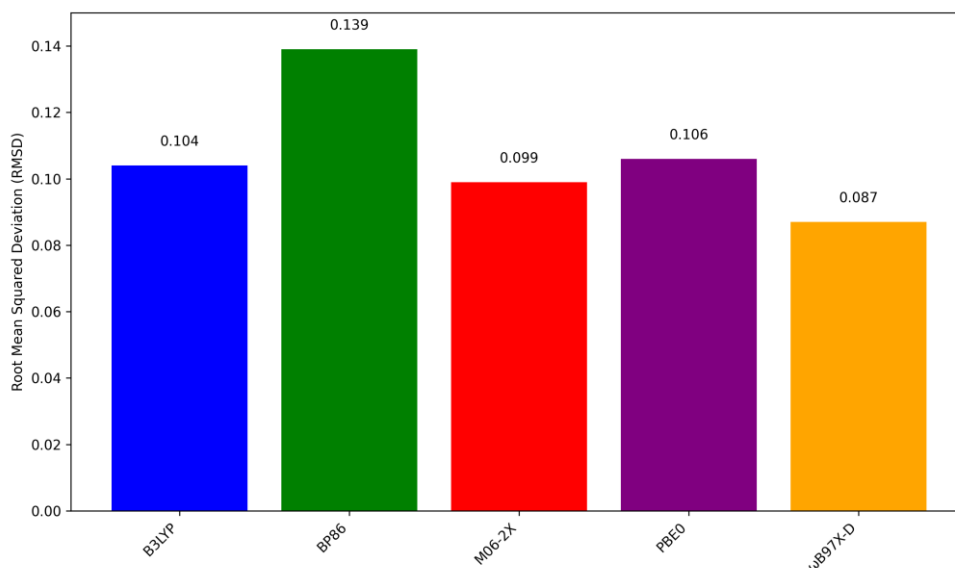


*Figure 3.1* RMSD values for five DFT functionals compared against the crystal structure of Blatter mono-radical **1**.

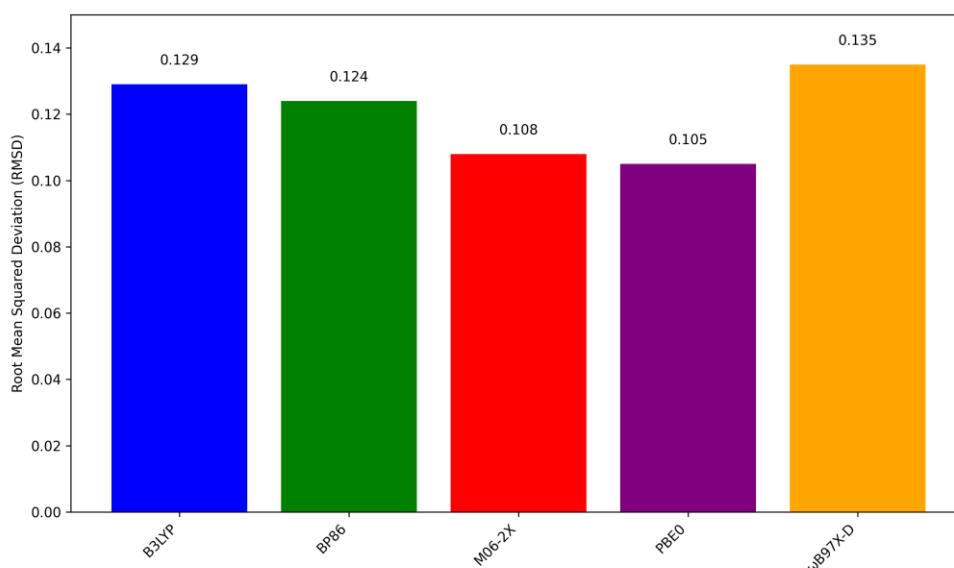


**Figure 3.2** RMSD values for five DFT functionals compared against the crystal structure of Blatter tri-radical **13**.

For the mono-radical, the analysis reveals that BP86 is the least optimal choice, with a significantly higher RMSD value of 0.139. In contrast,  $\omega$ B97X-D emerges as the most suitable functional, achieving the lowest RMSD of 0.087, indicating its superior accuracy in reproducing the mono-radical crystal structure.

Interestingly, the performance trends shift when examining the tri-radical data. While  $\omega$ B97X-D was the top performer for the mono-radical, it is the least suitable for the tri-radical, yielding an RMSD of 0.135. On the other hand, PBE0 stands out as the most suitable functional for the tri-radical, with an RMSD of 0.105. Notably, PBE0 also performs well for the mono-radical, with an RMSD of 0.106. The marginal difference between these values across both radicals establishes PBE0 as the most reliable choice for optimisation calculations using Gaussian.

The lower RMSD values reflect better agreement with experimental crystal structures, with values below approximately 0.15 Å widely accepted as indicative of reliable geometry optimisations in computational studies.

Based on the benchmark results, Gaussian 16 was employed for the optimisation and frequency analysis using the PBE0 functional. Frequency calculations were performed alongside the

optimisations to confirm the stability of the computed geometries and validate the successful completion of the calculations.

### 3.1.2 Structural Analysis of Outer-Substituted Systems

We now turn to the structural analysis of Blatter tri-radicals with substitutions at the N–H bonds, where the hydrogen atom is replaced by methyl and halogenated methyl groups. This analysis investigates how these substitutions influence the overall molecular geometry of the Blatter tri-radical in its quartet ground state and minimum-energy configuration. These halide substitutions influence the spatial arrangement and bonding characteristics within the molecule. This section explores the structural variations and bonding differences observed across a series of halide-substituted methyl groups in both the outer and inner positions: CH<sub>3</sub>, CH<sub>2</sub>F, CHF<sub>2</sub>, CF<sub>3</sub>, CH<sub>2</sub>Cl, CHCl<sub>2</sub>, CCl<sub>3</sub>, CH<sub>2</sub>Br, CHBr<sub>2</sub>, and CBr<sub>3</sub>. This comprehensive analysis highlights the impact of halogenation on molecular geometry and electronic properties. The 3-D structures of selected optimised compounds with substitutions in the outer ring are shown in **Figure 3.3**.

Starting with the CH<sub>3</sub> group, the molecule is largely planar, with the natural exception of the hydrogen atoms within the methyl group. Two hydrogen atoms are positioned below the plane, while the third, associated with the longest C–H bond (~1.10 Å), extends slightly above it. The bond lengths within the CH<sub>3</sub> group show minimal variation, with two nearly identical C–H bonds (~1.10 Å) and a slightly shorter third bond (~1.09 Å). The C–N bond connecting the methyl group to the rest of the molecule measures approximately 1.44 Å.



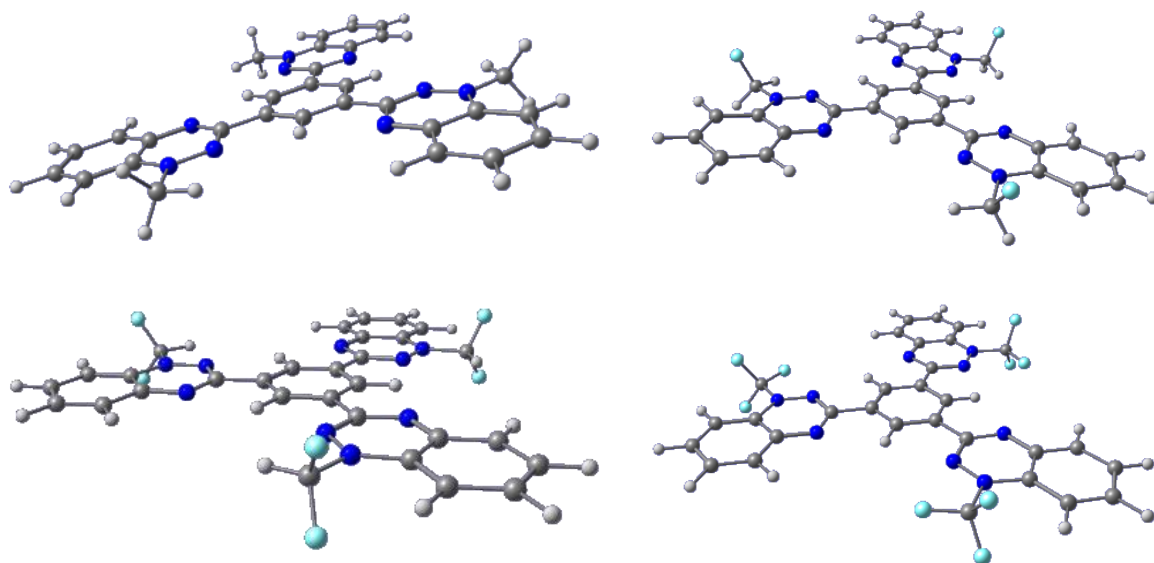


**Figure 3.3** Selected optimised outer-substituted structures (quartet state) of the Blatter tri-radical at the PBE0-D3(BJ)/def2-SVP level of theory. Top-left shows  $\text{CH}_3$ , top-right depicts  $\text{CH}_2\text{F}$ , bottom-left illustrates  $\text{CHF}_2$ , and bottom-right presents  $\text{CF}_3$ .

Substituting one hydrogen atom with a fluorine atom to form the  $\text{CH}_2$  group introduces some changes in bond characteristics while preserving the molecule's overall planarity. The two remaining C–H bonds remain consistent at approximately 1.10 Å, while the C–F bond is noticeably longer at ~1.37 Å, reflecting fluorine's larger atomic radius. Additionally, the C–N bond length shortens slightly to ~1.43 Å, a minimal yet noteworthy change. This can be attributed to fluorine's high electronegativity, which withdraws electron density from the carbon atom, increasing its partial positive charge. In turn, this enhances the electrophilicity of the carbon, strengthening the C–N bond by increasing its partial double-bond character. Although these changes in bond lengths are relatively small, they underscore how the substitution of a highly electronegative atom like fluorine can subtly alter the molecular geometry and electronic structure.

In the  $\text{CHF}_2$  group, the molecule remains predominantly planar, with slight deviations in the spatial orientation of the two fluorine atoms. The C–H bond stays consistent at approximately 1.10 Å, while the two C–F bonds are identical at ~1.34 Å, slightly shorter than the single C–F

bond in  $\text{CH}_2\text{F}$  due to the stronger electron-withdrawing effect of two fluorine atoms. The fluorine atoms are positioned asymmetrically, with one extending slightly above the plane and the other below, introducing minor non-planarity.

This spatial arrangement likely represents one of several conformers, as the C–N bond in the molecule is rotatable, allowing for different relative orientations of the  $\text{CHF}_2$  group. These conformers are expected to have very similar energies due to minimal steric hindrance between the groups, reflecting the dynamic nature of the molecule's geometry. Such conformational flexibility ensures that the molecule can adopt configurations that balance electronic and structural factors effectively.

Finally, the  $\text{CF}_3$  group exhibits a more pronounced influence of fluorine substitution on the molecular geometry. The three C–F bonds show a subtle trend of decreasing bond lengths compared to the mono and difluoromethyl groups, measuring approximately  $\sim 1.33 \text{ \AA}$  and  $\sim 1.31 \text{ \AA}$ , respectively. This slight shortening can be attributed to the cumulative electron-withdrawing effect from the three fluorine atoms, which strengthens the C–F bonds.

Interestingly, the C–N bond length reverts to  $\sim 1.44 \text{ \AA}$ , similar to the value observed in the  $\text{CH}_3$  group. This suggests a stabilisation effect as additional fluorine atoms are introduced, possibly due to the symmetrical distribution of electron-withdrawing effects around the carbon atom. This symmetry reduces electronic strain and restores the C–N bond length to its original length, highlighting how fluorination can influence not only localised bonding but also the broader electronic structure of the molecule.

Following the analysis of fluorine-substituted methyl groups, attention now shifts to the effects of chlorine substitution in the Blatter radical at the outer position. Chlorine's larger atomic size and moderate electronegativity, compared to fluorine, introduce distinct structural and electronic changes. These characteristics subtly reshape the bond lengths and spatial

arrangements, offering a contrasting perspective on the influence of halide substitutions. The resulting structural variations are depicted in **Figure 3.4**, highlighting the key differences introduced by chlorine substitution and providing further insights into the behaviour of these systems.

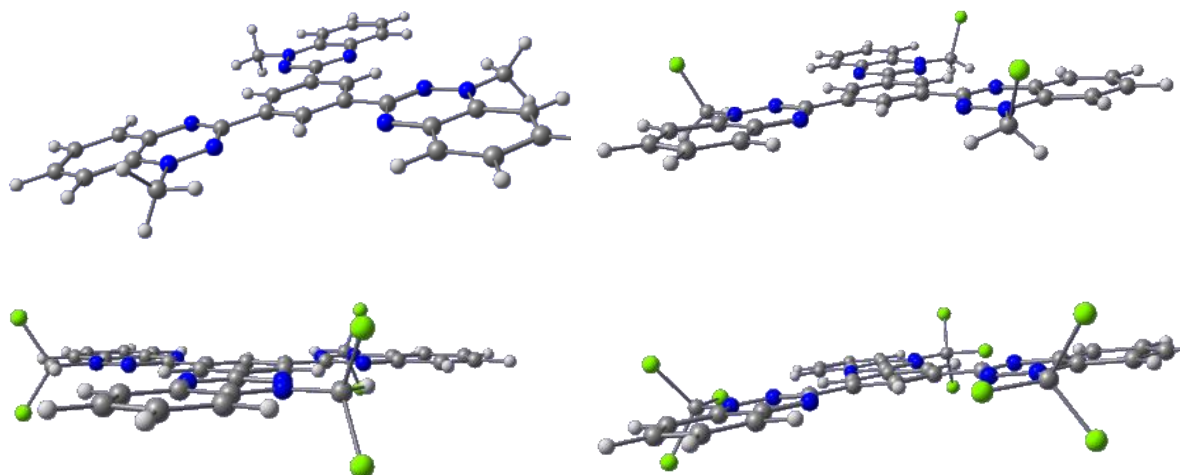


**Figure 3.4** Selected optimised outer-substituted structures (quartet state) of the Blatter tri-radical at the PBE0-D3(BJ)/def2-SVP level of theory. Top-left shows  $\text{CH}_3$ , top-right depicts  $\text{CH}_2\text{Cl}$ , bottom-left illustrates  $\text{CHCl}_2$ , and bottom-right presents  $\text{CCl}_3$ .

In the  $\text{CH}_2\text{Cl}$  group, the molecule retains its planar structure, much like the  $\text{CH}_2\text{F}$  group discussed earlier. The two C–H bonds remain consistent, measuring approximately 1.10 Å each. However, the C–Cl bond is notably longer at approximately 1.80 Å, significantly exceeding the length of the corresponding C–F bond in  $\text{CH}_2\text{F}$  (~1.37 Å). This elongation is naturally expected and attributed to chlorine’s larger atomic radius.

The C–N bond length measures about 1.42 Å, reflecting a slight shortening compared to the unsubstituted methyl group. This shift is similar to that observed in the  $\text{CH}_2\text{F}$  group, suggesting that the introduction of chlorine, like fluorine, influences the electronic environment around the carbon atom, subtly altering the bond characteristics within the molecule.

After the introduction of a second chlorine atom to form the  $\text{CHCl}_2$  group, the molecule continues to exhibit planarity, but the additional chlorine creates more pronounced changes. The single C–H bond remains consistent at approximately 1.10 Å, while the two C–Cl bonds measure around 1.79 Å each, slightly shorter than the lone C–Cl bond in  $\text{CH}_2\text{Cl}$ . This modest reduction in bond length mirrors the trend observed in the difluoromethyl group, where the addition of a second halogen resulted in shorter bonds. This effect is likely due to the cumulative electronic influence of the chlorine atoms, which slightly alters the electron density distribution around the central carbon atom. The C–N bond length remains steady at approximately 1.42 Å, showing that the introduction of a second chlorine atom maintains a similar structural balance as in  $\text{CH}_2\text{Cl}$ .

Finally, with the introduction of the  $\text{CCl}_3$  group, shows that it is possible to see that the molecule stays planar, with two of the C–Cl bonds measuring around 1.80 Å each, while the third bond being shorter in length, at 1.75 Å. This mirrors the pattern seen in the  $\text{CF}_3$  group, with the three C–X bonds ( $\text{X} = \text{halogen}$ ) showing small variations in bond lengths. The C–N bond in  $\text{CCl}_3$  case extends back to approximately 1.44 Å, similar to the value observed in the fully substituted  $\text{CF}_3$  group. This suggests a stabilisation effect as the number of chlorine atoms increases, likely due to the symmetrical electron-withdrawing influence of the three chlorine atoms, which balances the electronic environment around the central carbon atom. These observations also emphasise the parallels between the structural impacts of fluorine and chlorine substitutions while highlighting the unique contributions of each halogen's size and electronegativity.

Following the analysis of chlorine-substituted methyl groups, the structural analysis now shifts to the effects of bromine substitution in the Blatter radical at the outer position. Bromine represents the halogen with largest atomic size and lowest electronegativity compared to the halogens investigated in this thesis. The structures are shown in **Figure 3.5**.

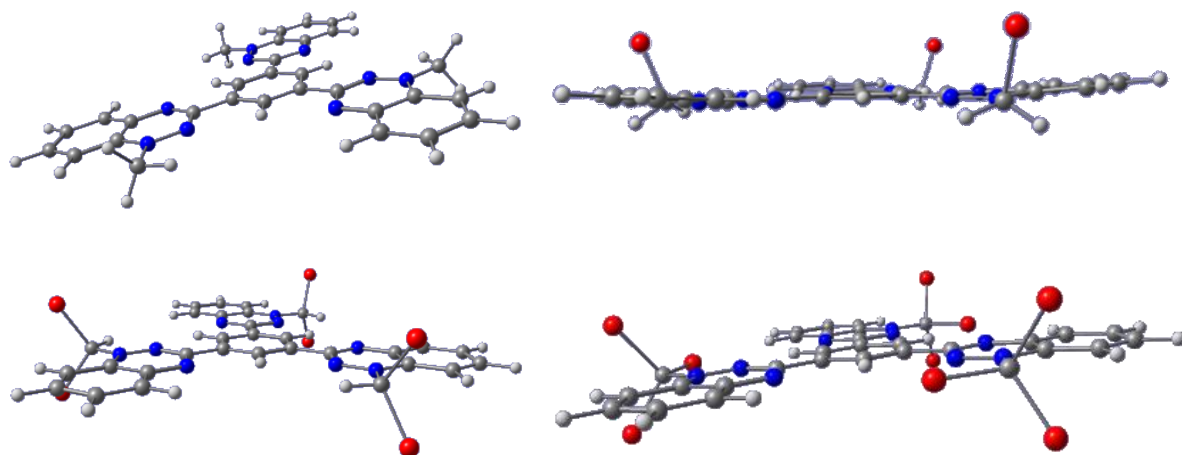


**Figure 3.5** Selected optimised outer-substituted structures (quartet state) of the Blatter tri-radical at the PBE0-D3(BJ)/def2-SVP level of theory. Top-left shows  $\text{CH}_3$ , top-right depicts  $\text{CH}_2\text{Br}$ , bottom-left illustrates  $\text{CHBr}_2$ , and bottom-right presents  $\text{CBr}_3$ .

In the  $\text{CH}_2\text{Br}$  group, the molecule retains planarity, consistent with the trends observed in previous substitutions. The introduction of bromine results in a C–Br bond length of approximately 1.98 Å, the longest bond observed in this analysis. The two C–H bonds measure around 1.10 Å and 1.09 Å, remaining largely unaffected by the substitution. The C–N bond length is approximately 1.41 Å, comparable to those in  $\text{CH}_2\text{Cl}$  and  $\text{CH}_2\text{F}$ , indicating that the substitution of bromine has a limited impact on the electronic environment of the C–N bond.

In both  $\text{CHBr}_2$  and  $\text{CBr}_3$  groups, planarity is preserved, with bromine's larger atomic size and steric effects resulting in the longest C–Br bonds observed. In  $\text{CHBr}_2$ , the two C–Br bonds are approximately 1.95 Å, while in  $\text{CBr}_3$ , the bonds range from 1.93 Å to 1.97 Å, showing a pattern consistent with increasing halogen substitution. The C–H bond in  $\text{CHBr}_2$  remains unchanged at ~1.09 Å, and the C–N bond length across both groups increases slightly, reaching ~1.43 Å in  $\text{CBr}_3$ . This progression highlights bromine's influence on bond elongation and structural adjustments, with steric effects becoming more pronounced as substitution increases.

The structural analysis of halide-substituted methyl groups in the Blatter radical demonstrates a consistent trend of maintained planarity despite variations in substituents. Fluorine

substitutions ( $\text{CH}_2\text{F}$ ,  $\text{CHF}_2$ ,  $\text{CF}_3$ ) lead to progressively shorter C–X bonds due to fluorine's strong electron-withdrawing effect. Chlorine substitutions ( $\text{CH}_2\text{Cl}$ ,  $\text{CHCl}_2$ ,  $\text{CCl}_3$ ) result in longer bonds, reflecting chlorine's larger size and lower electronegativity. Bromine substitutions ( $\text{CH}_2\text{Br}$ ,  $\text{CHBr}_2$ ,  $\text{CBr}_3$ ) produce the longest C–X bonds, driven by bromine's significant atomic size. Despite these variations, the substituents are positioned far from each other, avoiding steric clashes that could disrupt the molecular backbone's planarity. This highlights the stability of the Blatter tri-radical's core structure, regardless of the halogen substituent.

### 3.1.3 Structural Analysis of the Inner-Substituted Systems

To compare the effects of outer and central substitutions, the focus now shifts to Blatter radicals where the hydrogen atoms on the central phenyl ring are replaced by the same substituents previously discussed. This allows for a direct analysis of the structural alterations and differences between substitutions at these two positions. The comparison begins with the methyl group and the fluorine-substituted methyl groups, whose optimised 3-D structures are shown in **Figure 3.6**, highlighting how their placement impacts the molecular geometry and bonding characteristics of the Blatter tri-radical.

With  $\text{CH}_3$ , the structural impact differs significantly between inner and outer substitutions. As discussed before, in the outer position, the molecule retains planarity, consistent with previous observations. In the inner position, however, steric interactions between  $\text{CH}_3$  and the adjacent phenyl rings cause the outer phenyls to twist out of the plane, forming a crown-like structure. The central benzene ring remains planar, while the surrounding geometry adapts to minimise steric clashes.

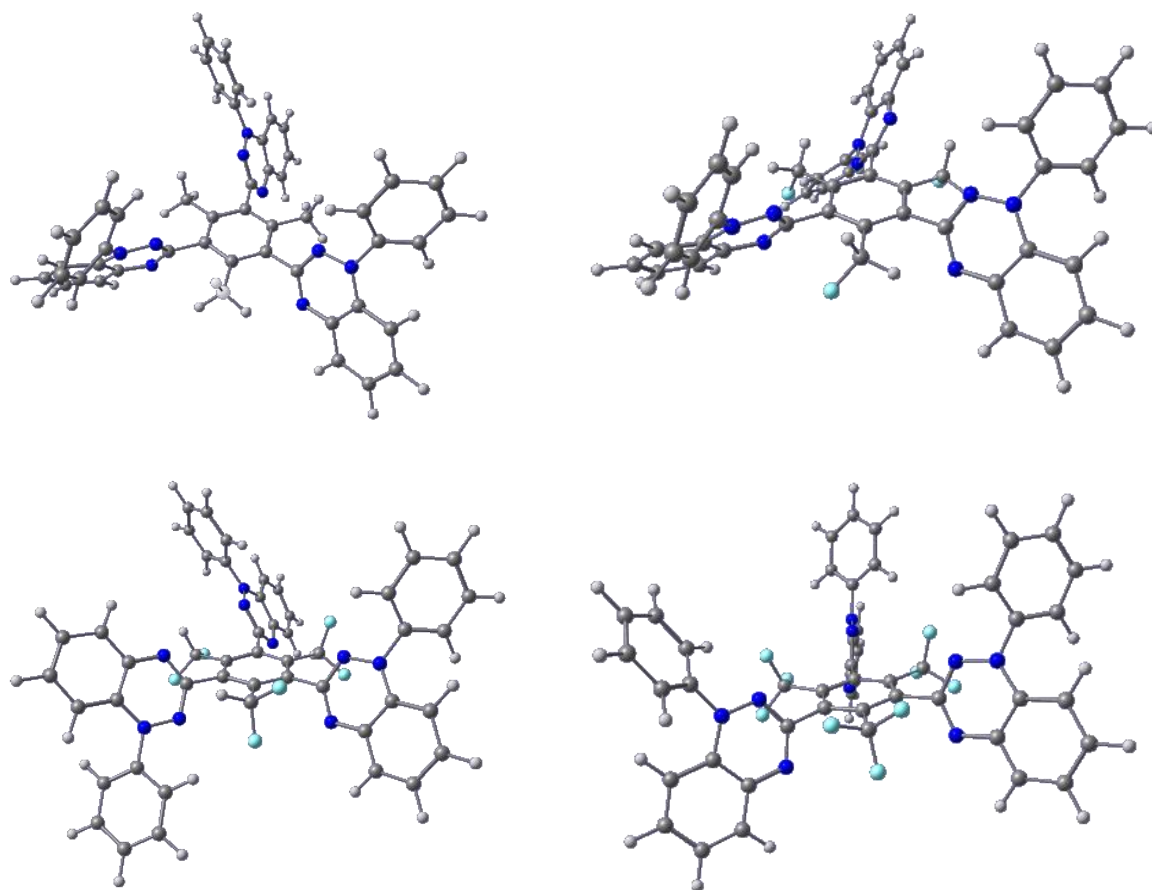


**Figure 3.6** Selected optimised inner-substituted structures (quartet state) of the Blatter tri-radical at the PBE0-D3(BJ)/def2-SVP level of theory. Top-left shows  $\text{CH}_3$ , top-right depicts  $\text{CH}_2\text{F}$ , bottom-left illustrates  $\text{CHF}_2$ , and bottom-right presents  $\text{CF}_3$ .

In this configuration, the C–C bonds within the central phenyl ring remain in the plane, with two C–H bonds extending below the plane and the third C–H bond of the methyl group positioned above it. The C–C bond lengths in the central phenyl are approximately 1.5 Å, while the C–H bonds measure around 1.1 Å. This pronounced difference between inner and outer substitutions point out the significant influence of steric effects when the substitution occurs closer to the core of the Blatter tri-radical molecule.

When fluorine-substituted methyl groups are placed in the inner position, the central phenyl ring remains planar, but the structural effects on the surrounding Blatter radical are more pronounced. For the  $\text{CH}_2\text{F}$  group, the molecule maintains planarity with C–H bonds at 1.1 Å and the C–F bond extending to 1.38 Å. Similar to the inner  $\text{CH}_3$  substitution, steric interactions cause the outer phenyl rings to rotate, preserving the crown-like structure observed previously.

In the case of the CHF<sub>2</sub> group, planarity of the central ring is also retained, but the spatial arrangement of the fluorine atoms introduces additional complexity. The C–F bonds, at ~1.35 Å, are positioned above and below the plane, creating a slightly non-planar configuration for the substituent. This orientation reflects a balance of steric and electronic effects, similar to outer CHF<sub>2</sub> substitution, where fluorine atoms influence bond lengths and spatial alignment. Despite these subtle variations, the inner CHF<sub>2</sub> group maintains the crown-like rotation of the Blatter radical, consistent with the trends seen in CH<sub>2</sub>F substitution.

Finally, for the CF<sub>3</sub> group, the inner substitution does lead to more significant structural rotations due the steric bulk that comes from the three fluorine atoms. The C–F bonds average between 1.33 Å and 1.34 Å, similar to outer substitution, but the rotations are more pronounced, furthering reinforcing the crown-like structure.

Moving on to the chlorine-containing systems (**Figure 3.7**), planarity is preserved in the central phenyl ring with CH<sub>2</sub>Cl substituents, but steric interactions induce a "bird-like" arrangement of the Blatter radicals, contrasting the planar outer substitution. The C–Cl bond measures ~1.80 Å, comparable to the outer system, but the inner C–C bond (~1.50 Å) is slightly shorter. Similarly, for CHCl<sub>2</sub>, inner substitutions maintain phenyl ring planarity but introduce asymmetry with one C–Cl bond above and one below the plane (~1.79–1.81 Å), and the C–C bond length increases to ~1.51 Å due to steric effects.



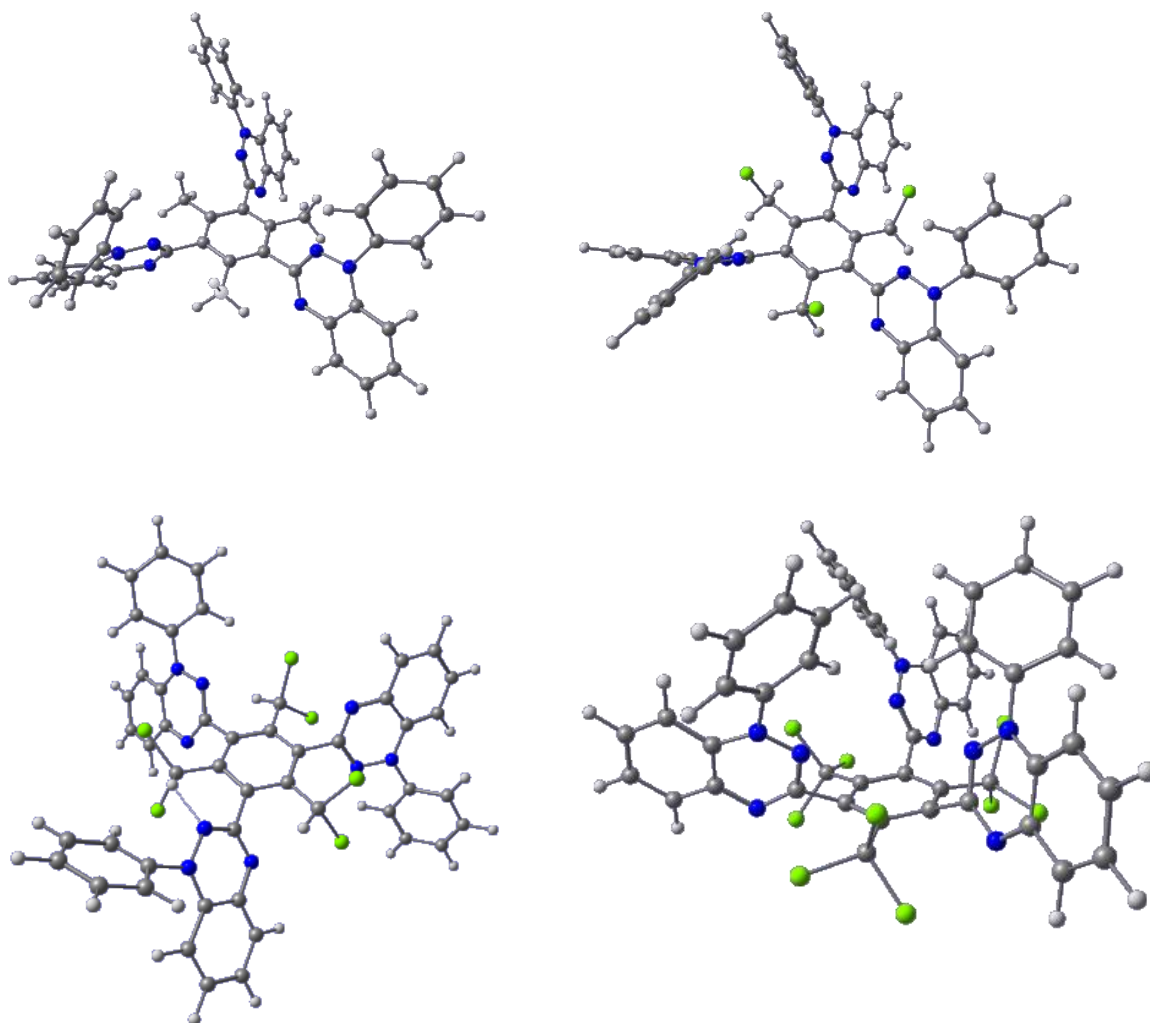


**Figure 3.7** Selected optimised inner-substituted structures (quartet state) of the Blatter tri-radical at the PBE0-D3(BJ)/def2-SVP level of theory. Top-left shows  $\text{CH}_3$ , top-right depicts  $\text{CH}_2\text{Cl}$ , bottom-left illustrates  $\text{CHCl}_2$ , and bottom-right presents  $\text{CCl}_3$ .

The trend intensifies with  $\text{CCl}_3$ , where inner substitutions disrupt planarity entirely, creating a pronounced crown-like structure. The C–Cl bonds ( $\sim 1.79$ – $1.80$  Å) remain consistent, but the C–C bond stretches to  $\sim 1.54$  Å, the longest in the series.

For bromine-substituted groups (**Figure 3.8**), the pattern mirrors chlorine but with more pronounced effects due to bromine's larger atomic size. In  $\text{CH}_2\text{Br}$ , inner C–Br bonds measure  $\sim 1.96$  Å, slightly shorter than in outer substitutions ( $\sim 1.98$  Å), while the central phenyl ring remains planar.  $\text{CHBr}_2$  introduces minor distortions to the phenyl ring, with C–Br bonds ( $\sim 1.94$ – $1.95$  Å) consistent between inner and outer positions. In  $\text{CBr}_3$ , planarity is entirely lost,

and inner C–Br bonds ( $\sim 1.95$ – $1.98$  Å) remain similar to outer substitutions, but the C–C bond length reaches  $\sim 1.54$  Å.

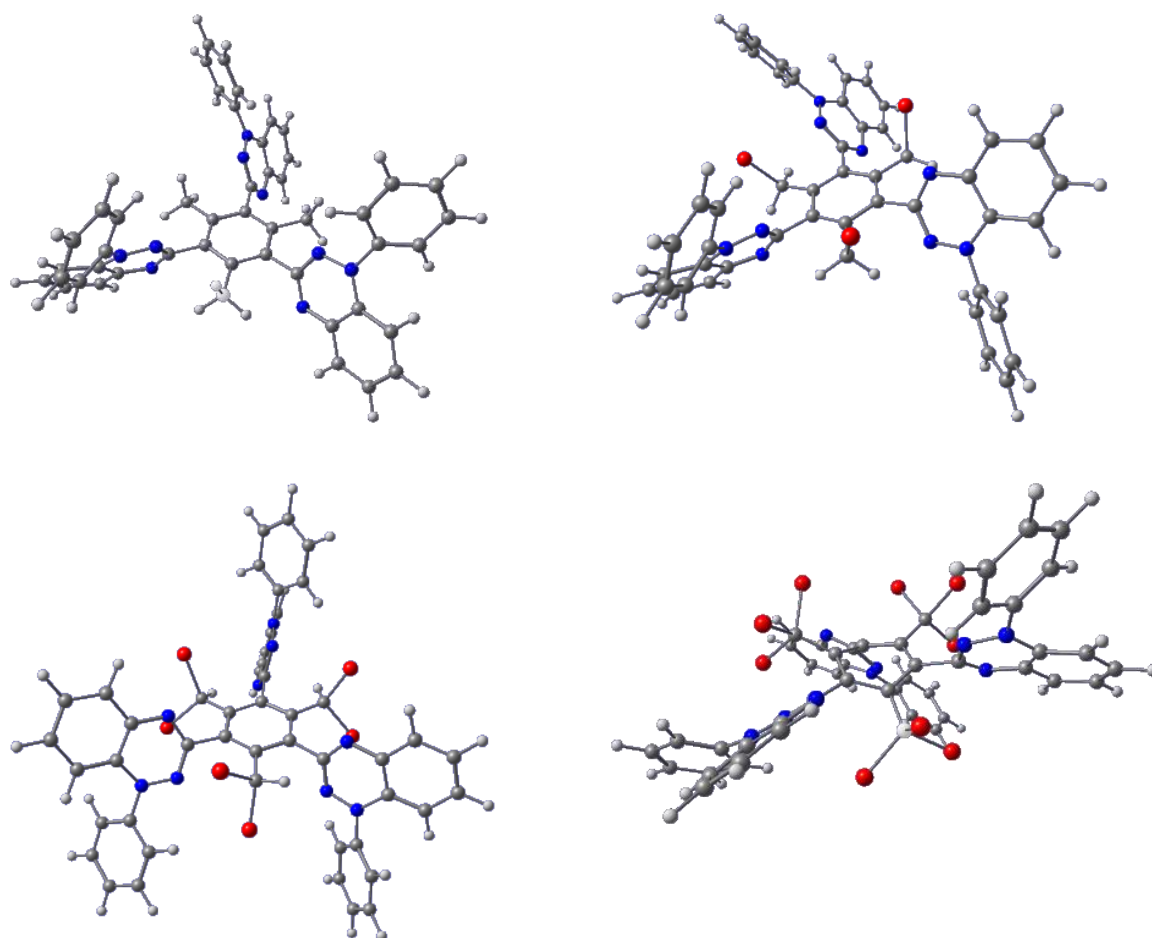


**Figure 3.8** Selected optimised inner-substituted structures (quartet state) of the Blatter tri-radical at the PBE0-D3(BJ)/def2-SVP level of theory. Top-left shows  $\text{CH}_3$ , top-right depicts  $\text{CH}_2\text{Br}$ , bottom-left illustrates  $\text{CHBr}_2$ , and bottom-right presents  $\text{CBr}_3$ .

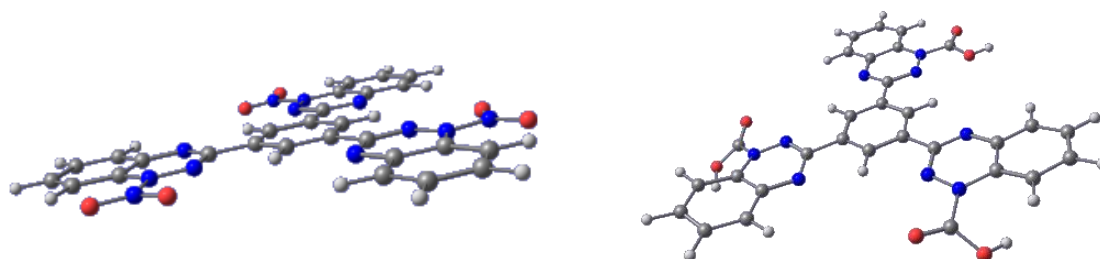
In conclusion, the halide analysis reveals a clear trend: increasing halogen size from fluorine to bromine leads to longer bond lengths and greater structural distortions, particularly in inner substitutions. Steric effects dominate, overshadowing electronegativity, with inner positions showing shorter bond lengths and more pronounced rearrangements compared to outer positions.

### 3.1.4 Outer EDG/EWGs

Continuing the structural analysis of the tri-radical systems, the focus now shifts to the influence of EWGs and EDGs on the molecular geometry. Both outer and inner substitutions are considered, starting with groups such as NO<sub>2</sub>, COOH, H, Ph, NH<sub>2</sub>, and CH<sub>3</sub> in the outer positions. The optimised structures for these groups are presented in **Figure 3.9**. The structure with R = CH<sub>3</sub> was discussed in the previous section and was placed here merely for visual comparison.

Let us start with the outer substitutions. The initial analysis begins with the NO<sub>2</sub> group, where the molecule remains fully planar despite the strong electron-withdrawing nature of the substituent. The N–N bond length is approximately 1.45 Å, while the N–O bonds measure around 1.19 Å and 1.20 Å. The uniformity of these bond lengths indicates that the NO<sub>2</sub> group integrates effortlessly into the molecular framework, as illustrated in **Figure 3.9**.

In contrast, the COOH group also preserves the overall planarity of the molecule but introduces a slight distortion. The carboxyl group causes a minor deviation, with the O–H portion positioned slightly above the molecular plane and the C=O bond slightly below it. This subtle alteration is reflected in the bond lengths: the C–O bond measures approximately 1.33 Å, the C=O bond around 1.19 Å, and the O–H bond about 0.97 Å. The N–C bond length remains consistent with that of the NO<sub>2</sub> group at approximately 1.44 Å, reinforcing that planarity is largely maintained despite the COOH substitution.



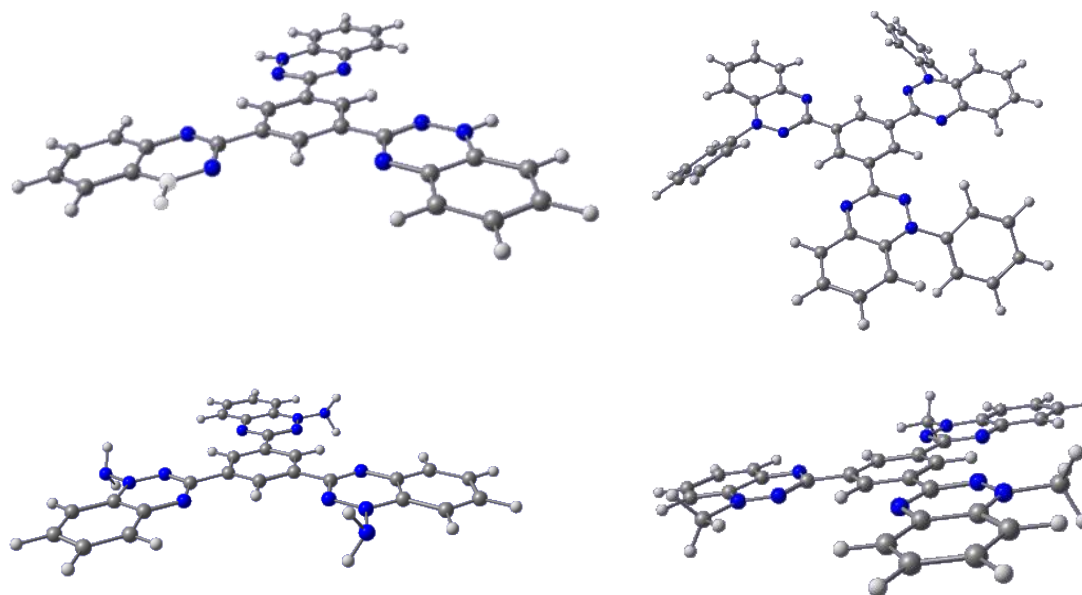


**Figure 3.9** Selected optimised outer-substituted structures (quartet state) of the Blatter tri-radical at the PBE0-D3(BJ)/def2-SVP level of theory. From top-left to bottom-right: NO<sub>2</sub>, COOH, H, Ph, NH<sub>2</sub>, and CH<sub>3</sub>.

Hydrogen, being a simple and neutral substituent in this series, is also shown as a reference point for the structural comparison. As anticipated, the system remains completely planar, with the N–H bond length measuring approximately 1.01 Å.

The Ph group represents the original structure of the Blatter radical. Although the core of the molecule remains planar, the Ph groups do occupy non-planar orientations through out of plane rotations, indicating that these rings do not participate in a larger conjugation with the core structure. The steric bulk of the phenyl group drives this deviation, as illustrated in **Figure 3.9**.

Continuing the series, the NH<sub>2</sub> group introduces a distinct distortion. While the molecule remains planar up to the NH<sub>2</sub> group, the attached hydrogens deviate slightly, with one positioned above the plane and the other below. This bent conformation results in N–N bond lengths of approximately 1.38 Å, shorter than those observed with NO<sub>2</sub> and COOH groups, reflecting a different electronic environment. The N–H bonds, both measuring around 1.02 Å, are similar to the bond length observed when hydrogen was the substituent.

To summarise, irrespective of the substituent, the Blatter tri-radical core remained planar. Substituents such as NO<sub>2</sub> and COOH maintain full planarity, with all atoms participating in the planar system. In contrast, Ph, NH<sub>2</sub>, and CH<sub>3</sub> induce non-planarity only in their substituent regions, leaving the core structure virtually unaffected.

### 3.1.5 Inner EWG/EDGs

This section examines the impact of EWGs and EDGs on the structural properties of the Blatter tri-radical system featuring inner substitutions. While the central Ph ring retains its planarity across all cases, substitutions in the inner positions introduce deviations in the overall molecular structure. Key substitutions analysed include EDGs such as NH<sub>2</sub> and N(Me)<sub>2</sub>, as well as EWGs like COOH and CHO, as illustrated in **Figure 3.10**.

Through the formation of hydrogen bonds between the NH<sub>2</sub> group and the nitrogen atoms in the outer systems, the NH<sub>2</sub> group leads the overall structure to become almost entirely planar, with just the Ph substituents deviating from planarity. The presence of these intramolecular hydrogen bonding creates a unique honeycomb-like structure, providing structural stability despite minor out-of-plane deviations. Bond lengths within the NH<sub>2</sub> system include a C–N bond of approximately 1.33 Å and C–H bonds ranging from 1.02 Å to 1.03 Å, with the longer bonds corresponding to hydrogens involved in hydrogen bonding.

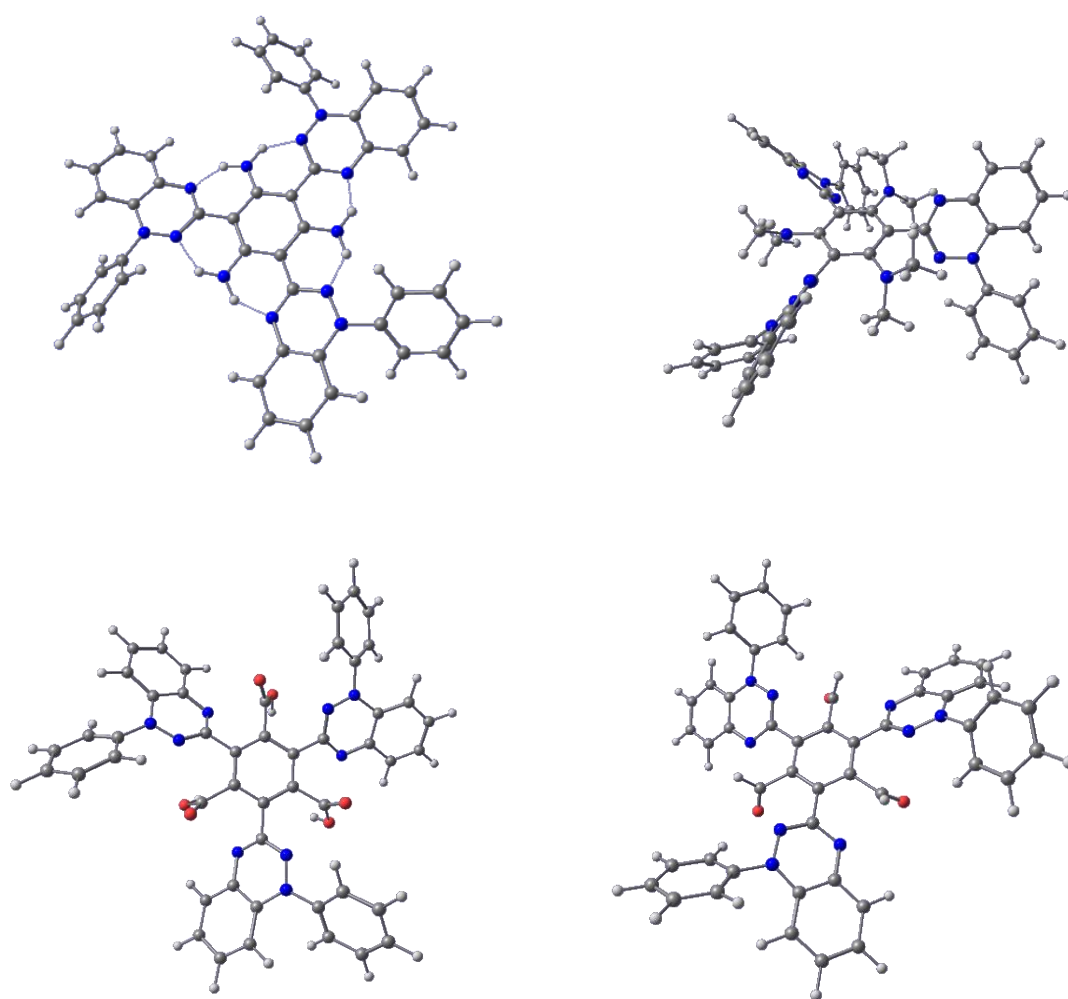


**Figure 3.10** Selected optimised outer-substituted structures (quartet state) of the Blatter tri-radical at the PBE0-D3(BJ)/def2-SVP level of theory. From top-left to bottom-right:  $\text{NH}_2$ ,  $\text{CH}_3$ ,  $\text{COOH}$ ,  $\text{CHO}$ .

The second EDG analysed in the inner position is  $\text{N}(\text{Me})_2$ . Similar to  $\text{NH}_2$ , the central phenyl ring remains planar; however, significant deviations arise due to steric hindrance from the two Me groups. One Me group extends above the plane, while the other points below, resulting in more pronounced out-of-plane distortions compared to  $\text{NH}_2$ . Unlike  $\text{NH}_2$ , the absence of hydrogen bonding in this system exacerbates the deviations, causing the Blatter radicals to rotate more extensively. Bond lengths in the  $\text{N}(\text{Me})_2$  group reveal a central C–N bond length of approximately 1.39 Å, slightly longer than in  $\text{NH}_2$ , while the C–N bonds of the methyl groups measure around 1.43 Å. C–H bond lengths range from 1.10 Å to 1.11 Å.

For the EWGs, COOH maintains planarity in the central phenyl ring, though the COOH group itself shows slight out-of-plane rotations. In the optimised conformer, the C=O bond extends above the plane, while the hydroxyl (OH) group points below. Unlike other systems, no hydrogen bonding is present. Bond lengths for the COOH group align with typical carboxylic acid behaviour: the C=O bond measures  $\sim 1.20$  Å, the C-O bond  $\sim 1.37$  Å, and the O-H bond  $\sim 0.97$  Å.

The fourth group and the second EWG in the inner analysis is CHO, which behaves similarly to COOH regarding the planarity of the central phenyl ring but exhibits the opposite orientation for the functional groups. No hydrogen bonding is observed, and the bond lengths are comparable to those in COOH: the C=O bond is  $\sim 1.20$  Å, while the C-H bond is slightly longer at  $\sim 1.11$  Å compared to the O-H bond in COOH.

To summarise the inner system substitutions, EDGs generally preserve the planarity of the central phenyl ring. The NH<sub>2</sub> group is unique due to its stabilising hydrogen bonding, which forms a honeycomb-like structure, whereas the bulkier N(Me)<sub>2</sub> introduces significant out-of-plane deviations due to steric hindrance from the methyl groups. EWGs such as COOH and CHO also maintain planarity but induce greater out-of-plane distortions due to the orientation of their functional groups, with no hydrogen bonding to stabilise the structure.

When comparing inner and outer systems, both EDGs and EWGs maintain the planarity of the central phenyl ring, but inner substitutions show greater deviations due to steric effects. Outer substituents like NO<sub>2</sub> and COOH, despite their electron-withdrawing nature, retain planarity with only minor out-of-plane shifts. Steric effects are more pronounced in the inner system, particularly with bulkier groups like N(Me)<sub>2</sub>, highlighting the influence of substitution position on the overall molecular geometry.

## 3.2 Blatter Tri-Radicals: Doublet-Quartet Gaps

### 3.2.1 Benchmark of D–G gaps

In this section, we discuss the benchmark done for the D–G energy gaps of the Blatter tri-radical system. These calculations were carried out through single-point calculations with several DFT functionals at the PBE0-optimised geometry. Among the tested functionals, PBE0 itself produced a D–Q gap of  $60\text{ cm}^{-1}$ . This value was compared to a reference DQ gap of  $38.1\text{ cm}^{-1}$ , calculated by Koutentis and his team at the University of Cyprus using the B3LYP functional.<sup>68</sup> The notable discrepancy between the PBE0 and B3LYP results already indicated a need for further refinement.

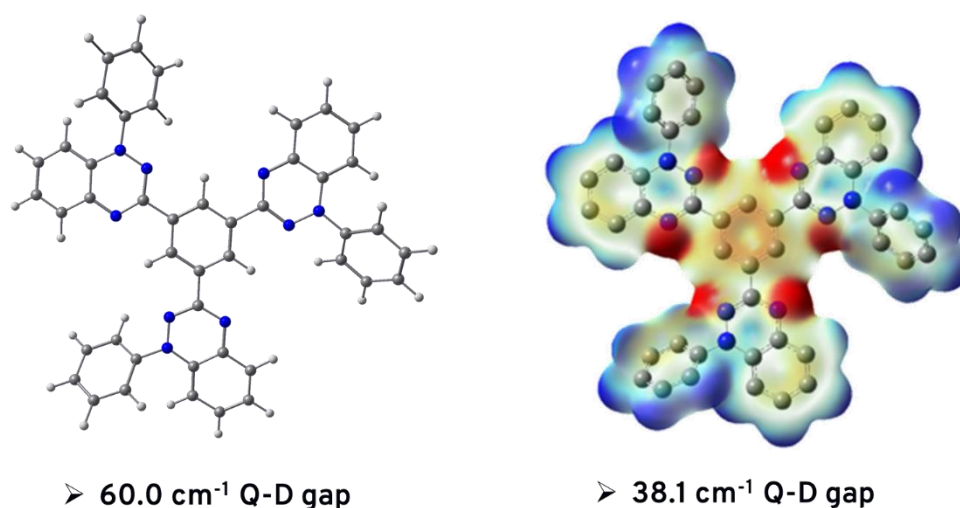


**Figure 3.11** Representation of the Blatter tri-radical: the left-hand side displays the calculated doublet-quartet gaps using the PBE0-D3(BJ)/def2-SVP method, while the right-hand side features the electrostatic potential map alongside a literature-reported doublet-quartet gap value using B3LYP.

To resolve this, additional single-point calculations were conducted using CASSCF/NEVPT2 methods with different active spaces, all based on the PBE0-optimised geometry. The reference active space selected for these calculations was (11,11). These advanced methods provided a more detailed and accurate analysis of the tri-radical's electronic structure, offering a robust evaluation of the functionals and basis sets. This systematic approach was crucial for improving



the reliability of the predicted electronic properties and ensuring consistency across the computational methodologies employed.

**Figure 3.12** illustrates the results of the CASSCF calculations performed with various active spaces, both with and without dynamic correlation included via the NEVPT2 approach. The data reveal that the choice of active space size significantly impacts the D–Q energy gap. A consistent trend is observed, where the gap increases as the active space is expanded from NEVPT2/CASSCF(3,3) to NEVPT2/CASSCF(11,11), suggesting that the quartet spin state becomes progressively more stabilised with improved treatment of electron correlation. However, the NEVPT2/CASSCF(7,7) calculation stands out with an anomalously negative gap of  $-7.9 \text{ cm}^{-1}$ , likely due to convergence issues. Attempts to extend the active space to 13,13 failed due to computational limitations, making NEVPT2/CASSCF(11,11) the largest feasible active space. Furthermore, NEVPT2/CASSCF(9,9) is not displayed as it did not converge properly. Consequently, the gap obtained with NEVPT2/CASSCF(11,11), calculated as  $45.3 \text{ cm}^{-1}$ , was adopted as the reference value.

**Figure 3.13** presents the D–Q gaps obtained with various density functionals compared against the NEVPT2/CASSCF(11,11) reference value. The data reveal that functionals like PBE0 and  $\omega$ B97X-D tend to overestimate the gap, whereas MN15, B3PW91, PW6B95D3, and TPSSh provide results more consistent with the multireference calculations. Their respective gaps and deviations ( $\Delta E$ ) are: MN15 ( $48.9 \text{ cm}^{-1}$ ,  $\Delta E$ :  $+3.6 \text{ cm}^{-1}$ ), B3PW91 ( $45.2 \text{ cm}^{-1}$ ,  $\Delta E$ :  $-0.1 \text{ cm}^{-1}$ ), PW6B95D3 ( $42.6 \text{ cm}^{-1}$ ,  $\Delta E$ :  $-2.7 \text{ cm}^{-1}$ ), and TPSSh ( $42.1 \text{ cm}^{-1}$ ,  $\Delta E$ :  $-3.2 \text{ cm}^{-1}$ ). Based on this comparison, B3PW91 was initially selected for single-point calculations due to its minimal deviation from the reference value.

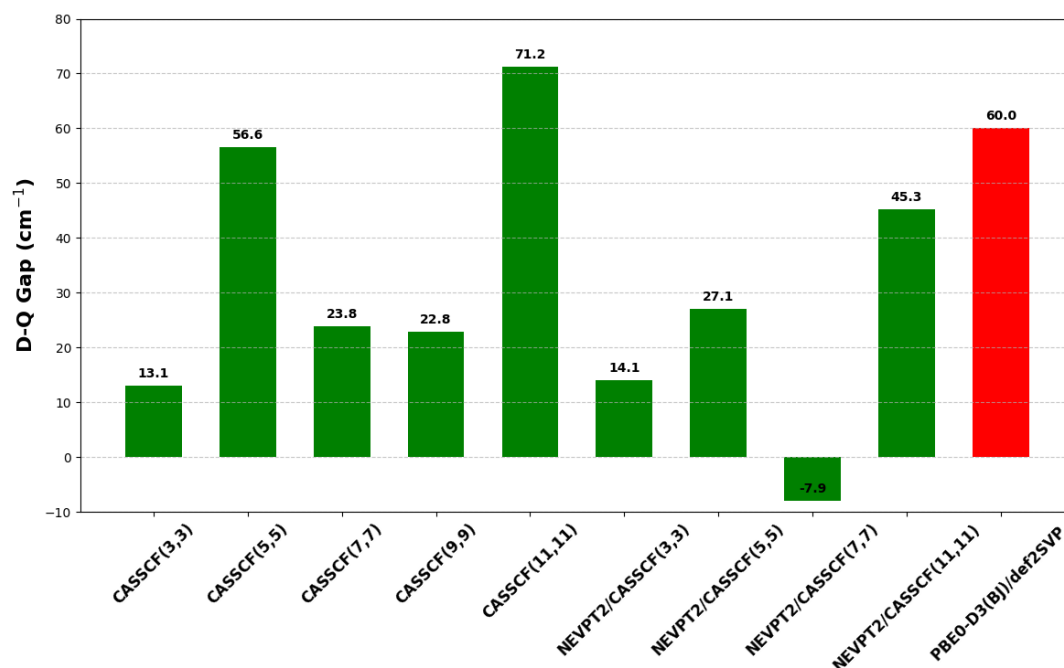


**Figure 3.12** Comparison of multireference calculations with PBE0 data for doublet-quartet energy gaps (cm<sup>-1</sup>) for the Blatter tri-radical **13**. Data includes calculations with dynamic correlation (NEVPT2/CASSCF) and without (CASSCF), for active spaces ranging from (3,3) to (11,11). Green bars represent post-HF calculations, while the red bar corresponds to the DFT (PBE0-D3(BJ)/def2-SVP) value. Results for NEVPT2/CASSCF(9,9) are excluded due to convergence issues.

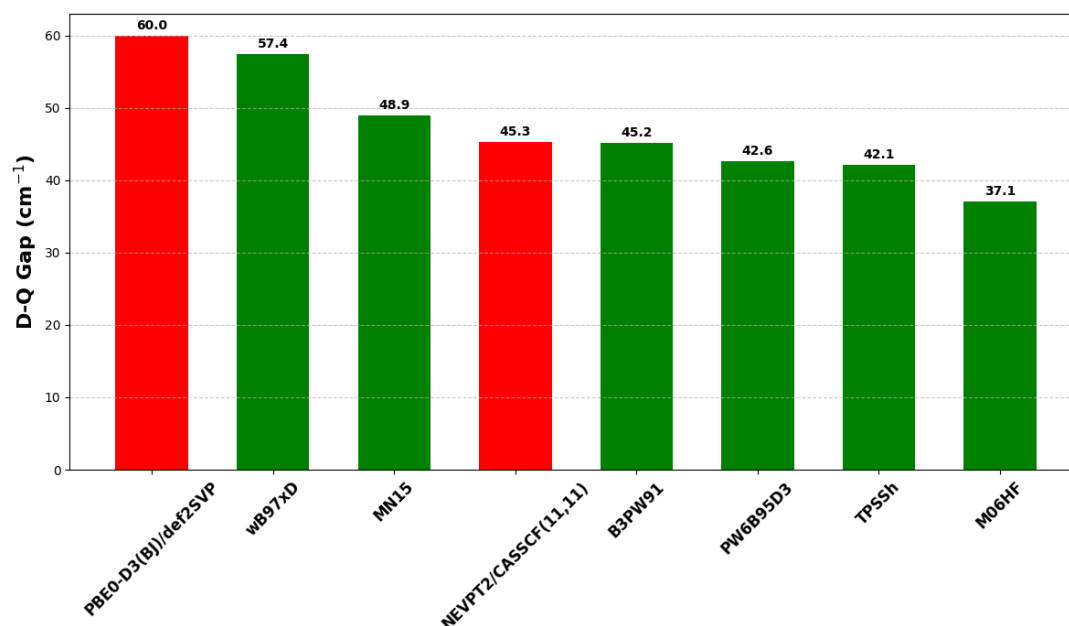


**Figure 3.13** Calculated doublet-quartet energy gaps (cm<sup>-1</sup>) for the Blatter tri-radical **13**. Energies for selected functionals are compared to reference values. Each bar represents a different functional, with reference values from NEVPT2/CASSCF(11,11) and PBE0-D3(BJ) shown in red, and results from other functionals displayed in green.

However, the use of different functionals for geometry optimisation (PBE0) and single-point energy calculations (B3PW91) introduced inconsistencies for certain systems, as explained in

later sections. To address this issue and streamline the analysis, the thesis mostly presents results using PBE0. Although this functional slightly overestimates the D–Q gaps relative to the multireference calculations, it offers a consistent framework for interpreting the results and provides an upper limit for the energy gaps.

Position	Major Observations
<b>Outer Halides</b>	Halides generally favour the quartet state. Cl-substituted systems show the highest D–Q gaps, F shows moderate gaps, and Br the lowest. CBr <sub>3</sub> is an outlier with an unusually small gap. PBE0 overestimates gaps; consistent use of functionals is crucial due to geometry sensitivity.
<b>Outer EWG/EDG</b>	EWGs (e.g., CHO, CN) increase the D–Q gap, favouring the quartet state, while EDGs (e.g., NH <sub>2</sub> , CH <sub>3</sub> ) reduce it. OH shows a high gap due to polar interactions. EWGs generally lead to larger gaps than EDGs.
<b>Inner Halides</b>	The inner halide groups show smaller D–Q gaps compared to the outer positions, likely due to steric effects. CF <sub>3</sub> and Cl-substituted groups favour the quartet state, while CHCl <sub>2</sub> shows a slight preference for the doublet. Bromine’s larger size and lower electronegativity reduce quartet stability
<b>Inner EWG/EDG</b>	EWGs like COOH and CHO show larger D–Q gaps, favouring the quartet state, similar to outer positions. EDGs like NH <sub>2</sub> , CH <sub>3</sub> , and N(Me) <sub>2</sub> show smaller gaps, with NH <sub>2</sub> favouring the doublet due to electron delocalization. Steric factors impact quartet stability more significantly in inner positions.

### 3.2.1 D–Q Gaps of Outer-Substituted Systems

This section examines the D–Q energy gaps for outer substitutions of Blatter tri-radicals, based on optimised structures at the PBE0 level of theory. Single-point energy evaluations were performed with both the PBE0 and B3PW91 levels, with most of the results discussed using PBE0, as stated above. The focus remains on halides, EWGs, and EDGs that were previously analysed.

**Figure 3.14** illustrates the calculated D–Q energy gaps of all outer-substituted systems, calculated at the PBE0-D3(BJ)/def2-SVP level of theory. Each bar represents a different system within the outer series, with halide-containing groups shown in red and the remaining EWGs and EDGs displayed in green.

Examining **Figure 3.14**, it is evident that various substituents significantly impact the D–Q energy gap, influencing the stability of the quartet versus doublet states. EDGs such as  $\text{NH}_2$  and  $\text{N}(\text{Me})_2$  still favour the quartet state but to a lesser extent than EWGs. EWGs like  $\text{NO}_2$ ,  $\text{CN}$ , and  $\text{CHO}$  heavily favour the quartet state, particularly the latter, exhibiting the most extreme gap at  $194.4\text{ cm}^{-1}$ . In all cases, however, the quartet remains as the ground state multiplicity. This analysis indicates that EWGs favour the quartet state more than EDGs. Notably, the  $\text{OH}$  substituent is absent from the dataset due to its calculation returning an error value, which prevented its inclusion in the analysis.

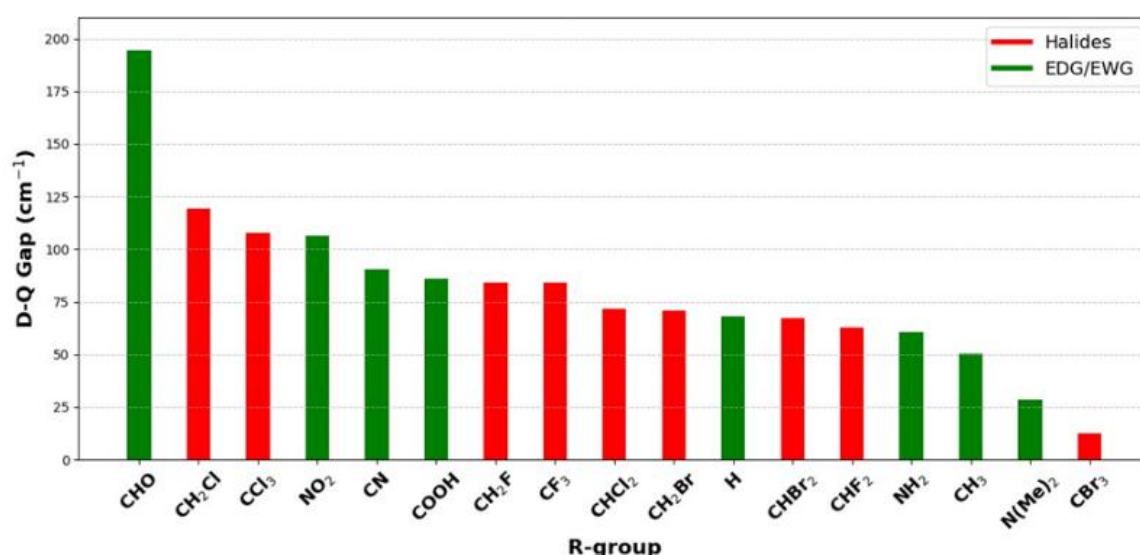


**Figure 3.14** Optimized energies for the doublet-quartet gaps for all of the outer substituted systems, calculated at the PBE0-D3(BJ)/def2-SVP level of theory. Each bar represents a different system within the outer series, with halide-containing groups shown in red and the electron-withdrawing and electron-donating groups displayed in green.

In contrast to this, substitutions like  $\text{CBr}_3$  and  $\text{N}(\text{Me})_2$  show much smaller D–Q gaps.  $\text{CBr}_3$  is especially notable, having the smallest D–Q gap of  $12.5\text{ cm}^{-1}$ . Although the specific reasons for the particularly small difference between the doublet and quartet states are beyond the scope of this thesis, future investigations could benefit from analysing spin densities, bringing information into the electronic distribution and interactions that contribute to these differences.

Halogenated substituents, such as  $\text{CHF}_2$ ,  $\text{CHCl}_2$  and  $\text{CHBr}_2$ , display moderate to high D–Q gaps, with  $\text{CH}_2\text{Cl}$  clearly standing out at  $119.5\text{ cm}^{-1}$ , reinforcing a strong trend towards the quartet state. The only halogenated system that does not follow this trend is  $\text{CBr}_3$ .

Next, we discuss the results for the D–Q energy gaps obtained using the combined approach, where geometries were optimised with the PBE0 functional and energy gaps calculated using B3PW91. These results are presented in **Figure 3.15**. For example, in the case of  $\text{CHO}$ , it is evident that, as noted earlier, PBE0 tends to overestimate the energy gaps compared to B3PW91, which aligns more closely with the NEVPT2/CASSCF data. However, in certain instances, such as  $\text{NO}_2$  and  $\text{N}(\text{Me})_2$ , the energy gaps deviate significantly, appearing dramatically larger than for any other system.

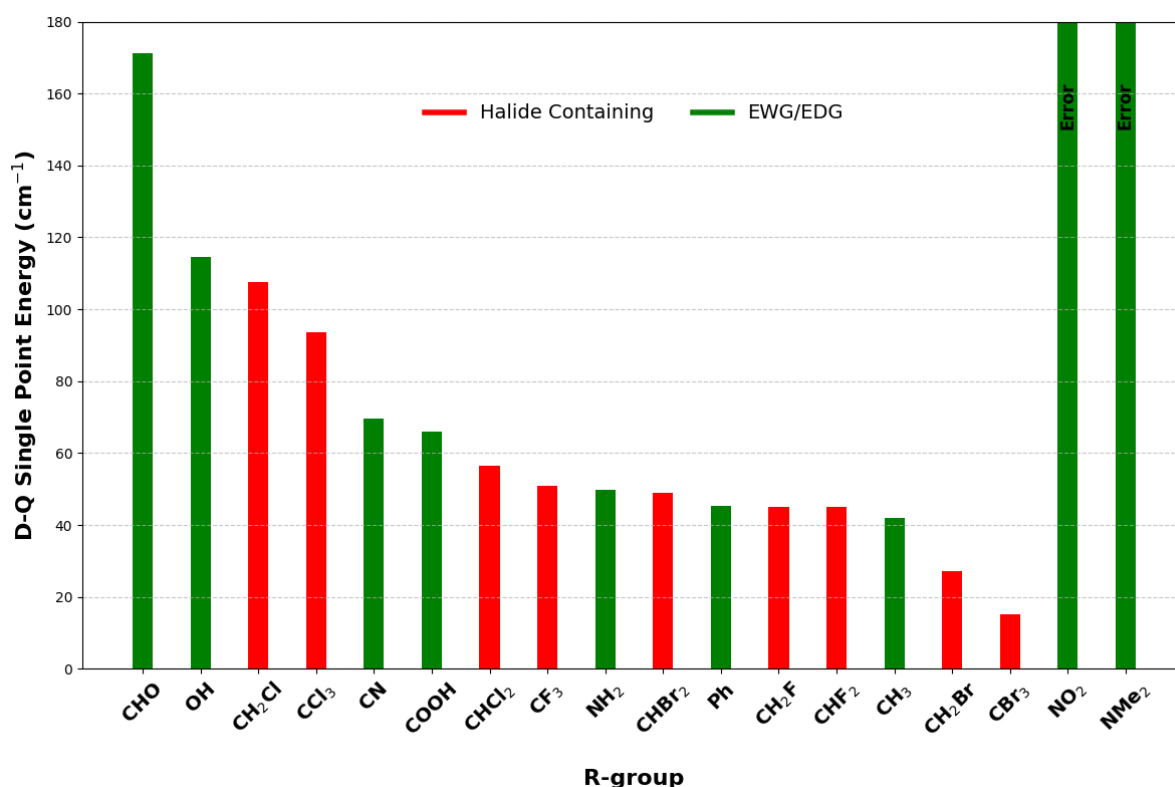


**Figure 3.15** Single-point energies for the doublet-quartet gaps across all outer-substituted systems, calculated at the B3PW91-D3(BJ)/def2-TZVPP//PBE0-D3(BJ)/def2-SVP level of theory. Each bar represents a unique system within the outer series, with halide-containing groups highlighted in red, and electron-withdrawing and electron-donating groups shown in green. Notably, two outer systems exhibit anomalously high values, suggesting significant error; these points are displayed on the right-hand side of the figure for completeness.

This discrepancy is particularly pronounced in the inner-substituted systems, as discussed later, and highlights the sensitivity of these computations to geometry changes. These findings suggest that it is critical to use the same functional for both geometry optimisation and energy calculations to ensure consistency. As a future direction, reevaluating the DFT-derived values with a unified functional for both geometry optimisations and D–Q gap calculations is strongly recommended. Preliminary results, which highlight the differences arising from optimising geometries and calculating single-point energies using the B3PW91 functional, are discussed in greater detail later in this thesis.

Focusing now on the halides a consistent pattern emerges. The fluoride-substituted groups show moderate D–Q gaps, ranging between  $44.9\text{ cm}^{-1}$  and  $51.0\text{ cm}^{-1}$ . Compared to PBE0, these results confirm that PBE0 tends to overestimate the energy gaps. This adjustment indicates that the fluorinated systems have a slightly reduced preference for the quartet state than initially suggested by the PBE0 calculations.

Chlorine-substituted groups exhibit a higher and broader range of values than fluoride-substituted groups, ranging from  $56.6\text{ cm}^{-1}$  to  $107.6\text{ cm}^{-1}$ . This increasing trend reflects chlorine's ability to stabilise the quartet state more effectively, observed in both single-point and geometry energies. The PBE0 functional overestimation of D–Q gaps is, again, observed.

Focusing on the bromide-substituted groups, they show the smallest D–Q gap range among the halides, from  $15.3\text{ cm}^{-1}$  to  $48.9\text{ cm}^{-1}$ . This suggests that bromine's larger atomic size and lower electronegativity exert less stabilising influence on the radical's quartet state. It is important to note that  $\text{CBr}_3$ , which could be potentially further explored at the NEVPT2 level.

Turning our attention to EDGs, we observe a different trend. EDGs like  $\text{NH}_2$ ,  $\text{CH}_3$ , and  $\text{OH}$  tend to reduce the D–Q gap, as their ability to donate electron density destabilises the quartet state relative to the doublet. The groups  $\text{NH}_2$  and  $\text{CH}_3$ , with gaps of  $49.9\text{ cm}^{-1}$  and  $41.9$

cm<sup>-1</sup> respectively, show a slight tendency to stabilise the quartet state but only marginally compared to EWGs. This suggests a more balanced stability between the two spin states. However, the OH group shows a high gap of 114.5 cm<sup>-1</sup>, which could imply that polar interactions stabilise the quartet state beyond expectations. Overall, EDGs tend to favour a narrower D–Q gap compared to EWGs, but their effects can be influenced by additional factors such as potential hydrogen bonding or polar interactions.

In summary, the D–Q gaps of the Blatter tri-radical in the outer systems are heavily influenced by the electronic nature of the substituent groups. The trend among the halides is that lighter halogen-containing groups like chlorine favour the quartet state more, leading to larger gaps, while heavier halide-containing groups tend to reduce the gap, resulting in the lowest gaps in the data set. EWGs like CHO and CN push the system towards quartet stability, while EDGs, though still favouring the quartet state somewhat, lead to smaller gaps. Anomalous results in NO<sub>2</sub> and N(Me)<sub>2</sub> need further exploration, and CBr<sub>3</sub>, highlighted as an anomalous result, should be tested at the NEVPT2 level to validate the single-point calculations.

Next, we performed direct comparisons of molecules that were optimised and had single-point energies calculated using the same functional. This approach was taken because using different functionals for optimisation and single-point calculations led to anomalous results, such as for N(Me)<sub>2</sub> and NO<sub>2</sub> with B3PW91 single points. Calculations were performed where systems were optimised and single-point energies calculated using either only PBE0 or only B3PW91, to determine whether the functionals themselves were at fault or if the mixing of functionals caused the anomalous values observed in **Figure 3.16**.

The results clearly demonstrate that the D–Q energy gap is highly sensitive to differences in geometries. Taking the Ph substituent as an example, using PBE0 exclusively yields a gap of 60.0 cm<sup>-1</sup>. When single-point energies are calculated with B3PW91 on the PBE0-optimised

geometry, the gap reduces to  $45.2\text{ cm}^{-1}$ , as shown in previous plots. However, when both geometry optimisation and single-point calculations are performed with B3PW91, the D-Q gap further decreases to  $22.5\text{ cm}^{-1}$ , which is significantly smaller than the value obtained from the reference NEVPT2/CASSCF(11,11) calculations.

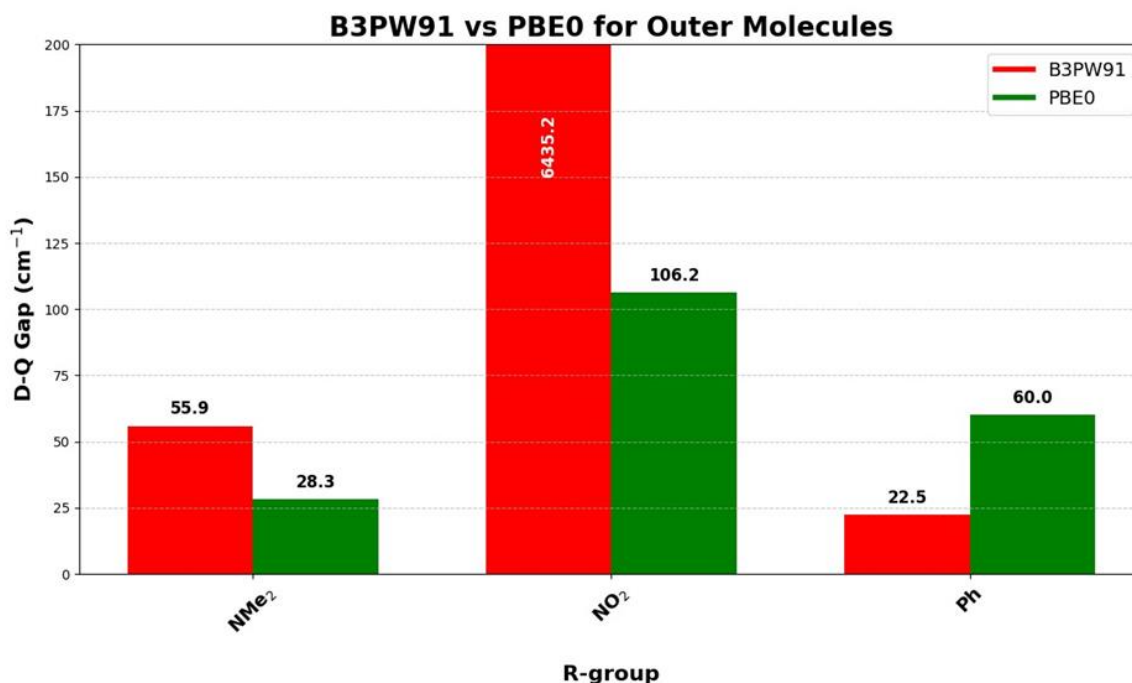


**Figure 3.16** Comparison of single-point energies for the doublet-quartet gap in the outer systems, focusing on three groups:  $N(\text{Me})_2$ ,  $\text{NO}_2$ , and Ph. Calculations for B3PW91 were performed at the B3PW91-D3(BJ)/def2-TZVPP//B3PW91-D3(BJ)/def2-SVP level, while PBE0 calculations used the PBE0-D3(BJ)/def2-TZVPP//PBE0-D3(BJ)/def2-SVP level of theory. Data is colour-coded, with B3PW91 results in green and PBE0 results in red. One B3PW91 value shows an anomalously high result, included for completeness.

A particularly notable anomaly is observed for the  $\text{NO}_2$  system, where B3PW91 predicts an energy gap of  $6,453.2\text{ cm}^{-1}$ —dramatically larger than the  $106.2\text{ cm}^{-1}$  gap computed with PBE0. This suggests that relying solely on the Ph system as a benchmark is insufficient and that the benchmark should also include systems exhibiting anomalies, such as  $\text{NO}_2$ , to ensure more robust conclusions.

Moreover, the choice of method significantly affects the predicted trends. For example, PBE0 suggests that  $N(\text{Me})_2$  decreases the D-Q



energy gap compared to Ph, whereas B3PW91 predicts the opposite trend. Expanding the benchmark analysis to include NEVPT2/CASSCF calculations for these systems, particularly those with anomalous behaviour, could provide important information for selecting an appropriate method. Collectively, these findings strongly suggest that mixed approaches—where geometries are optimised at one DFT level and energy gaps are computed with another—should be avoided.

### 3.2.2 D–Q Gaps of Inner-Substituted Systems

This section focuses on the D–Q gaps for the inner substitutions, presenting the energy gaps of the optimised structures at the PBE0 level and, whenever applicable, single-point energy evaluations carried out at the B3PW91 level. Comparisons of single-point calculations using PBE0 and B3PW91 are also discussed. As in previous sections, the analysis concentrates on halides and EWGs/EDGs. This analysis sheds some light into how these substituents affect the D–Q gap of the Blatter tri-radicals, with particular attention to steric factors that could explain the smaller gaps.

**Figure 3.17** shows the optimised energies for the D–Q gaps for all inner-substituted systems, calculated at the PBE0-D3(BJ)/def2-SVP level of theory. Each bar represents a different system within the inner series, with halide-containing groups shown in red and EWGs and EDGs displayed in green.

The halide groups show variation in the D–Q gaps. The  $\text{CF}_3$  group shows a slight favouring of the quartet state, which is expected as all systems in the outer series favoured the quartet state, albeit more strongly than the inner systems. However, the  $\text{CHCl}_2$  group shows a very slight preference towards the doublet state, one of only two cases in these systems favouring the doublet. A small favouring of the quartet state is observed among the bromine groups, but the

halide that favours the quartet state most in the inner systems is the chlorinated substituent (with exception of the anomalous  $\text{CHCl}_2$  case). This suggests that chlorinated derivatives are drastically impacting the electronic properties, potentially due to steric crowding and their moderate electron-withdrawing properties. The bromine derivatives have the lowest average D–Q gaps among the halides, likely because the steric bulk of bromine atoms reduces the extra stability that the quartet structures usually present.

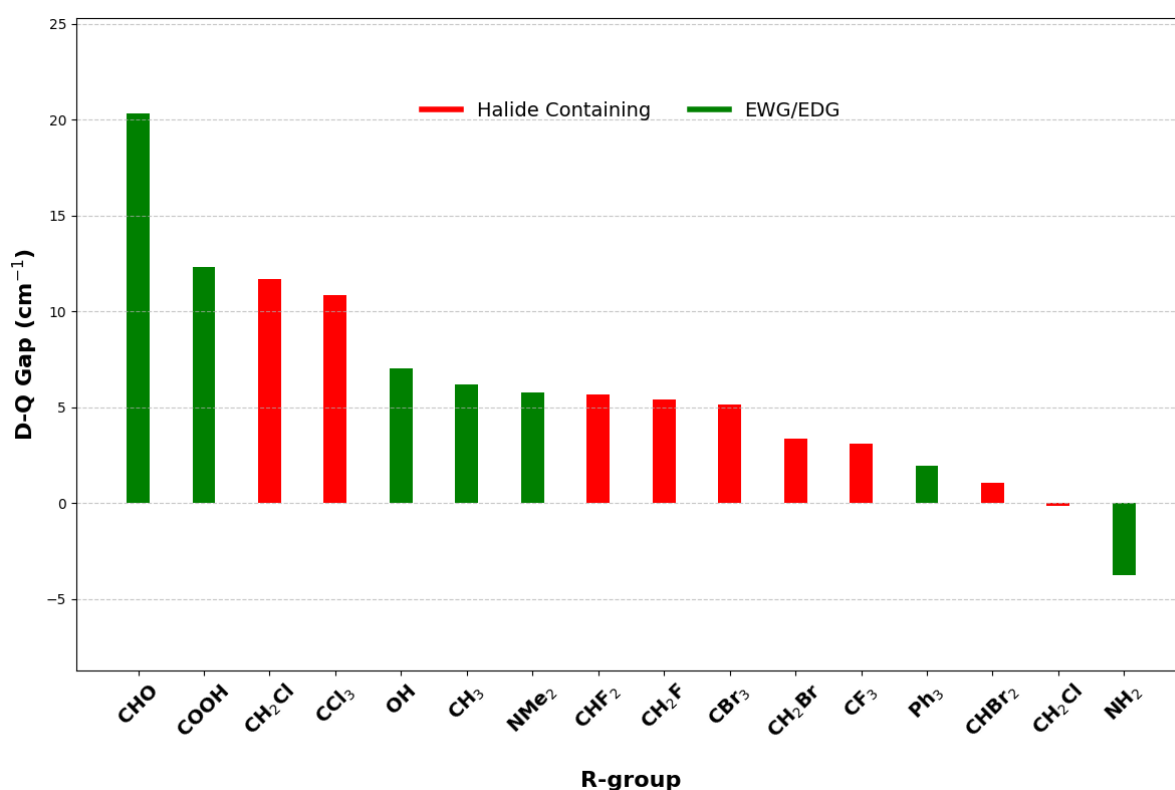


**Figure 3.17** D–Q energy gaps for all of the inner substituted systems, calculated at the PBE0-D3(BJ)/def2-SVP level of theory. Each bar represents a different system within the inner series, with halide-containing groups shown in red and the remaining electron-withdrawing and electron-donating groups displayed in green.

In contrast, electron-withdrawing groups such as COOH and CHO result in the highest D–Q gaps, in agreement with the outer cases. This suggests that these groups alter the electronic environment by pulling electron density away from the core structure of the tri-radical, thereby increasing the D–Q gap and favouring the quartet state. On the other hand, EDGs show moderate gaps within the series but are closer to favouring the doublet state than the EWGs.

The substituent  $\text{NH}_2$ , which forms an extended planar structure held together by hydrogen bonds, favours the doublet state, contrary to the other two EDGs, which slightly favour the quartet state. For  $\text{NH}_2$ , the preference for the doublet should be related to electron delocalisation, which would favour a doublet state due to reduced Pauli repulsion. For the other cases, the small preference for the quartet indicates that inner substitutions destabilise the system, which is even more pronounced for compounds featuring EDG substituents. The  $\text{CH}_3$  group shows a moderate gap, aligning with its weaker electron-donating capabilities compared to more potent EDGs like  $\text{N}(\text{Me})_2$ .

Building on the analysis of the optimised structures at the PBE0 level, we turn to the single-point calculations at the B3PW91 level. The single-point calculations are shown in **Figure 3.18** and **Figure 3.19**. They follow the same trends as before but with slight differences in the numerical values of the D–Q gaps. The exception is  $\text{CH}_2\text{Cl}$ , not shown in the figure because the value was considerably larger than all the others. This highlights once more that the mixed method should be avoided as it brings anomalies for some cases.

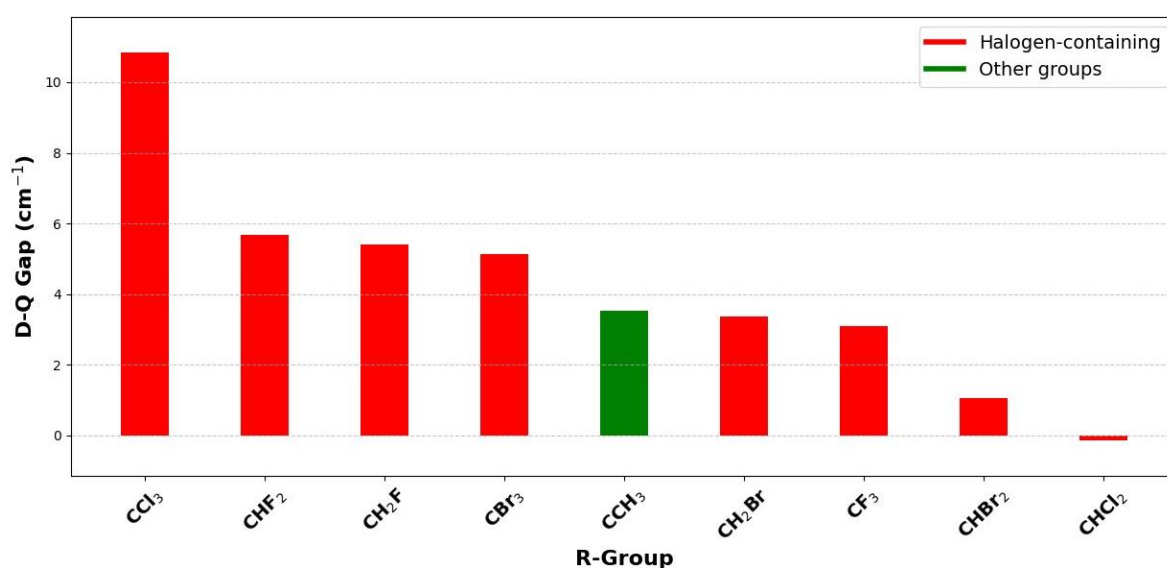


**Figure 3.18** D–Q energy gap data for inner systems containing halide groups, compared to a reference methyl group, calculated at the B3PW91-D3(BJ)/def2-TZVPP//PBE0-D3(BJ)/def2-SVP of theory. Halide-containing groups are displayed in red, while the methyl group is shown in green as the reference point. The halide data are symmetrically distributed around the

methyl group with four above and below the reference point, with chlorine-containing groups exhibiting the highest and lowest energy values.

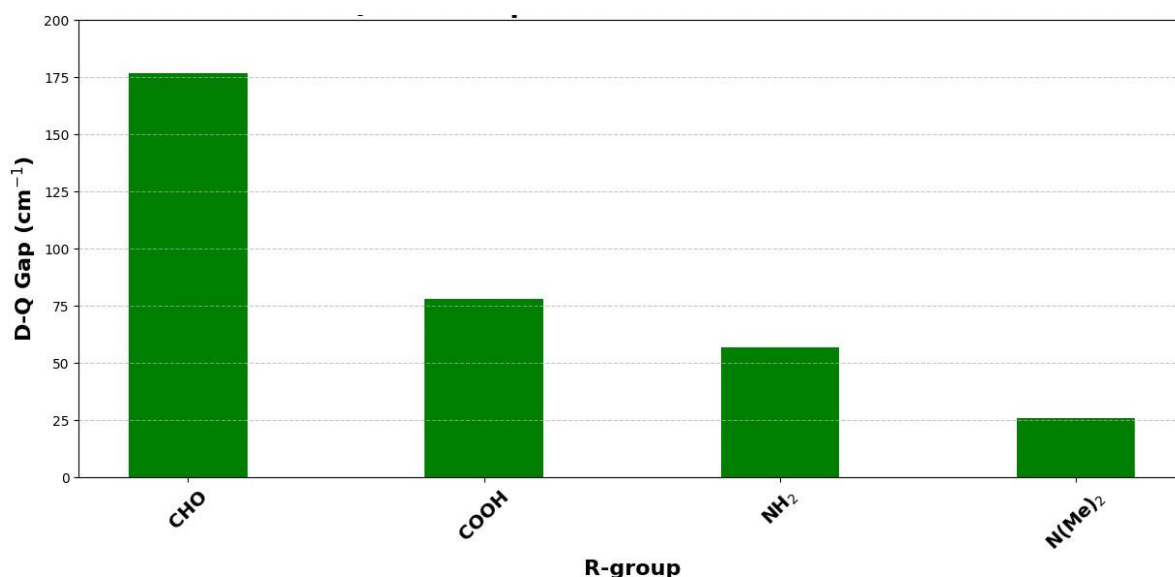


**Figure 3.19** D–Q energy gap data for inner systems with both electron withdrawing and electron-donating groups, calculated using the B3PW91-D3(BJ)/def2-TZVPP//PBE0-D3(BJ)/def2-SVP level of theory. This comparison highlights the influence of electron withdrawing and electron-donating groups on energy values within the inner system.

In the B3PW91 calculations, the smaller D–Q gaps observed for halides are consistent with trends seen with the PBE0 functional. In both cases, steric hindrance from large halogen atoms like Br and Cl contributes to reducing the energy gap. Overall, the PBE0 and B3PW91 functionals display similar trends, although the precise values of the D–Q gaps may differ slightly.

Interestingly, inspection of **Figure 3.19** reveals that B3PW91 predicts D–Q gaps for the inner systems that are comparable to the typical PBE0 values observed for the outer systems. However, these gaps are significantly larger than those predicted by B3PW91 for the systems shown in **Figure 3.18**. This suggests that B3PW91 overestimates the energy gaps for substituted systems in the inner position. Once again, this highlights the inconsistency of the mixed DFT approach across the dataset, reinforcing the importance of adopting a uniform computational methodology to ensure reliable and accurate results.

**Figure 3.20** compares the single-point energies for the D–Q gap in the inner bromine systems, calculated using both B3PW91 and PBE0 methods. The comparison reveals that PBE0 provides more reliable and consistent results. For example, the B3PW91 values fluctuate drastically, particularly for  $\text{CHBr}_2$  and  $\text{CBr}_3$ . The extreme values for these molecules suggest that B3PW91 is not consistent at the single-point level, indicating that a different functional should be selected in future studies or that PBE0, which was best for optimisation, should be used consistently. It is important to note that the PBE0 functional was observed to overestimate values in benchmark single-point calculations, but the consistency of the results, despite overshooting, demonstrates that PBE0 is suitable for calculations on these tri-radicals.

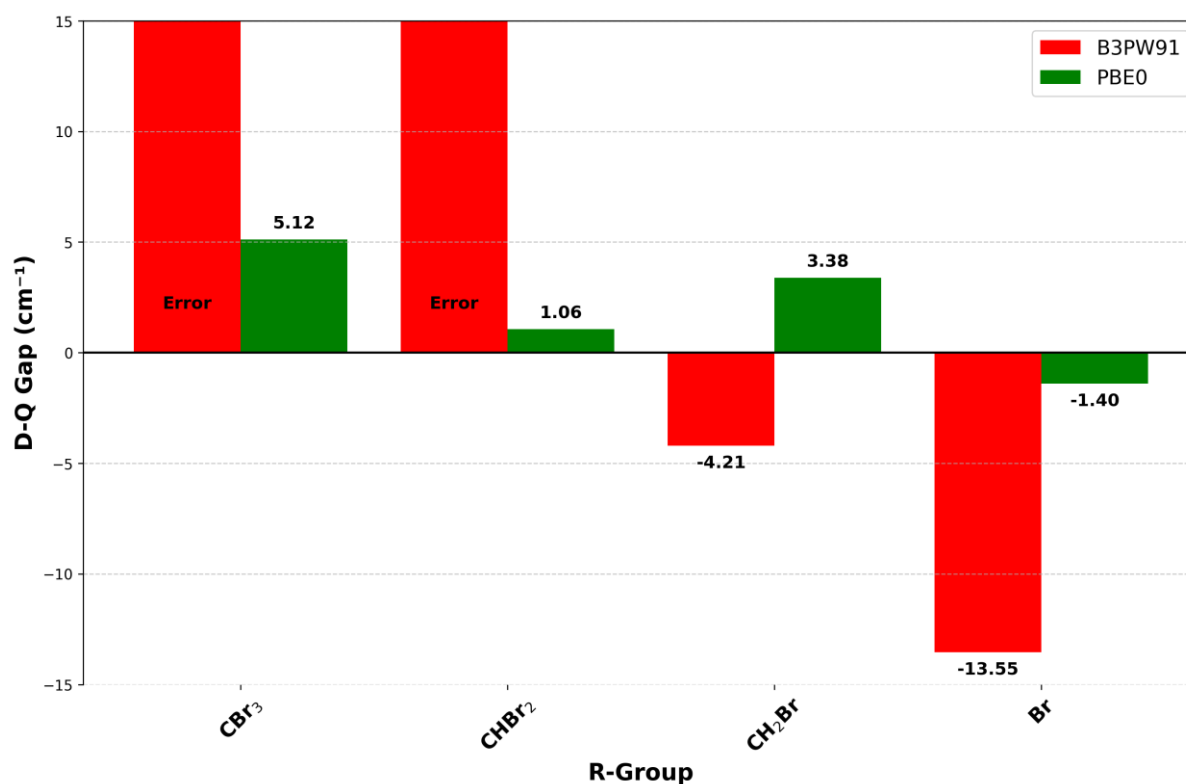


**Figure 3.20** Comparison of D–Q energy gaps in the inner bromine-containing systems, calculated using both B3PW91 and PBE0 methods. Calculations for the B3PW91 method were performed at the B3PW91-D3(BJ)/def2-TZVPP//B3PW91-D3(BJ)/def2-SVP level, while the PBE0 calculations used the PBE0-D3(BJ)/def2-TZVPP//PBE0-D3(BJ)/def2-SVP level of theory. The data is colour-coded, with B3PW91 systems shown in green and PBE0 systems in red. Notably, B3PW91 exhibits two instances where the energy gap exceeds  $7000\text{ cm}^{-1}$ , displayed as errors due to exceedingly high values.

### 3.3 Energy Gaps in Additional Systems

Finally, we move towards investigating the electronic structure of the remaining additional systems **26–30** and their variations (*vide supra*). We start by exploring the sulphur-containing fused dithiazole-triazine molecules **26–28** and their selenium- and phosphorus-containing analogues, all potential diradicals (for the structures of the systems, see **Figure 1.15**). This analysis allows for insight into their electronic properties and the intricate factors that would influence their stability.

Notably, among these groups there is a preference for the singlet state across these configurations, as shown in **Figure 3.21**. In this series, the SSN configuration (**28a**) exhibits the most favourable energy towards the singlet state, with a singlet-triplet (S–T) energy gap of  $-29.5 \text{ kcal mol}^{-1}$  (negative value indicates a singlet ground state). SSN (**26a**) follows closely with a strong preference for the singlet state, showing an energy gap of  $-22.9 \text{ kcal mol}^{-1}$ . In contrast, SNS (**27a**), although still preferring the singlet state, shows the lowest favourability with an energy gap of  $-9.3 \text{ kcal mol}^{-1}$ . These trends demonstrate that the position of the nitrogen atom inherently affects the energy gap, with certain configurations heavily favouring the singlet state. Therefore, the computations reveal that none of these cases exhibit true diradical character; instead, they are best described as closed-shell singlet ground states.

Examining the sulphur and phosphorus groups, namely SSP (**26b**), SPS (**27b**), and PSS (**28b**), there is a notable decrease in the S–T gaps across these configurations compared to the sulphur-nitrogen groups. Phosphorus-substituted molecules show a diminished preference towards the singlet state. For example, SSP (**26b**) shows a gap of  $-13.0 \text{ kcal mol}^{-1}$ , representing a considerable reduction from the corresponding SSN gap. This trend draws attention to phosphorus's distinct electronic characteristics: its larger atomic size and lower electronegativity compared to nitrogen result in less effective orbital overlap, leading to

decreased stabilisation of the singlet state. Additionally, phosphorus may destabilise the singlet state due to steric factors. Its larger size may introduce repulsive interactions with nearby atoms, affecting the overall energy.

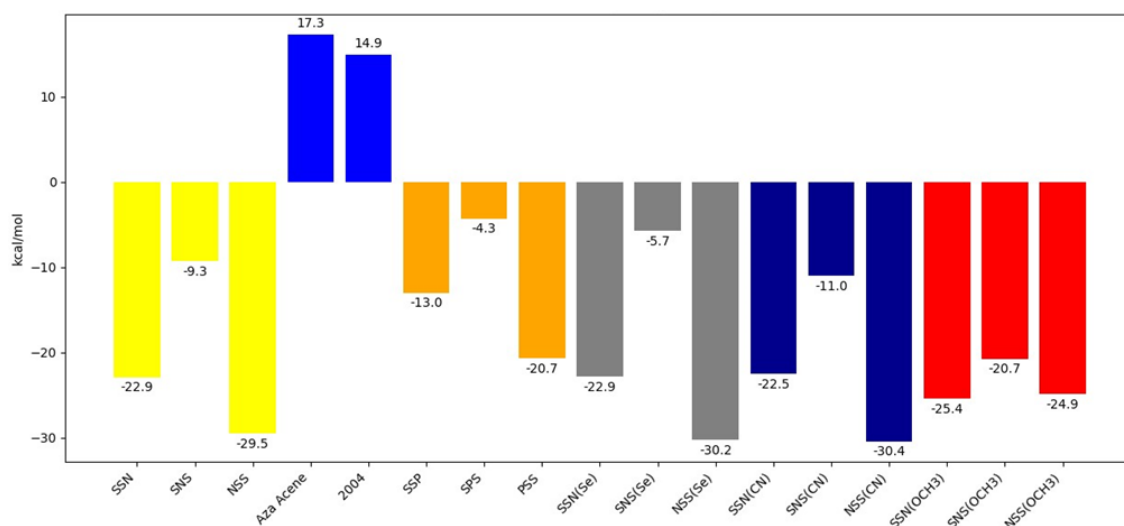


**Figure 3.21** Energy gaps for fused dithiazole-triazine derivatives, the aza-acene tri-radical and the Blatter-type Schatz diradical, optimized at the PBE0-D3(BJ)/def2-SVP level of theory. Systems are colour-coded to illustrate structural variations: yellow for dithiazole-triazine systems **26a–28a**, navy for **29** and **30**, orange for phosphorus-containing systems **26–28b**, grey for selenium-containing systems **26c–28c**, dark blue for CN group additions to **26a–28a**, and red for the corresponding OCH<sub>3</sub> group additions.

Turning to the selenium-containing molecules, where sulphur is substituted by selenium atoms, we observe that selenium introduces unique features influencing the electronic structure. In the configuration SeSeN (**26c**), herein labelled SSN(Se), the S–T gap is nearly identical to that of SSN (**26a**) with an energy gap of  $-22.9 \text{ kcal mol}^{-1}$ , indicating minimal impact from selenium substitution in this configuration. Similarly, SSN(Se) (**26c**) retains a strong singlet preference of  $-30.2 \text{ kcal mol}^{-1}$ , closely mirroring its sulphur counterpart. However, in the configuration SNS(Se) (**26b**), the S–T gap is reduced to  $-5.7 \text{ kcal mol}^{-1}$ , suggesting that in this arrangement, selenium diminishes the gap.

Adding functional groups such as CN and OCH<sub>3</sub> to the triazine ring allows the investigation into how EWGs and EDGs impact the singlet-triplet gap. Specifically, we tested replacing the

hydrogen substituent from the carbon atom of triazine, given its closer proximity to the potential radical centre. The CN EWG group increases singlet state stability in various configurations. For example, adding CN to the SNS (**27a**) configuration elevates the singlet-triplet gap from  $-9.3 \text{ kcal mol}^{-1}$  to  $-11.0 \text{ kcal mol}^{-1}$ , reflecting a stronger preference for the singlet state. Similarly, in SSN(CN), incorporating the CN group leads to a marginal gap increasing to  $-30.4 \text{ kcal mol}^{-1}$ . This trend illustrates how specific functional groups can be added to manipulate electronic properties, paving the way for tailored applications.

Turning to the EDG  $\text{OCH}_3$ , the methoxy group shows a more complex interaction with the singlet state. In the configuration SSN( $\text{OCH}_3$ ), analogous to **26a**, the S–T gap shifts to  $-25.4 \text{ kcal mol}^{-1}$ , indicating a stronger preference for the singlet state in the  $\text{OCH}_3$ -containing species rather than SSN alone (S–T gap:  $-22.9 \text{ kcal mol}^{-1}$ ). This enhancement may be due to the increased electron density provided by the methoxy group, promoting singlet-state stabilisation. However, in SSN( $\text{OCH}_3$ ), analogous to **28a**, the S–T gap becomes slightly less negative at  $-24.9 \text{ kcal mol}^{-1}$  (for comparison,  $-29.5 \text{ kcal mol}^{-1}$  for **28a**) suggesting that although the methoxy group generally enhances the singlet state, it may also introduce interactions that slightly destabilise the singlet state in specific nitrogen-sulphur configurations.

The intricate behaviour of the  $\text{OCH}_3$  group illustrates the complexity of electronic interactions within the molecular framework. The interplay between electron donation and steric factors, along with the specific geometric arrangement of atoms, can lead to varied effects on singlet stability. Therefore, it is essential in future work to consider these factors when designing such molecules.

Finally, both the aza-acene (**29**) and the Blatter-type Schatz diradical (**30**) appear as the only systems with a preference for the open-shell state (quartet and triplet, respectively) by 17.3



and 14.9 kcal mol<sup>-1</sup>. Therefore, only these two systems, amongst compounds **26–30**, can be accurately identified as genuine radicals.

In summary, this comprehensive analysis highlights the influence of heteroatom and functional group integration on the S–T energy gaps in fused dithiazole-triazine systems. The introduction of selenium generally preserves a singlet state preference, with minor variations dependent on the structural context. In contrast, substituting nitrogen with phosphorus results in a reduction of the singlet-triplet gaps, indicating a weakening of the singlet state. The electron-withdrawing properties of the CN group significantly enhance singlet stability, particularly in nitrogen-rich configurations, while the electron-donating nature of the OCH<sub>3</sub> group tends to reinforce singlet state stability but can exhibit complex interactions influenced by the specific molecular context. Therefore, none of the fused dithiazole-triazine systems can be classified as radicals; this designation applies exclusively to compounds **29** and **30** amongst the additional systems analysed.

# Chapter

## 4. Conclusions and Future Work

This thesis study provided a comprehensive analysis of the structural and electronic properties of Blatter-type tri-radicals and additional organic diradicals of interest to our experimental collaborators, focusing on the influence of various substituents on bond lengths, molecular geometry, and spin-state stability.

In the structural analysis of Blatter tri-radicals with outer substitutions, halogen substitutions significantly impacted the molecular geometry. Fluorine-substituted groups, such as  $\text{CH}_2\text{F}$ ,  $\text{CHF}_2$ , and  $\text{CF}_3$ , exhibited decreased bond lengths with increasing fluorine content, illustrating fluorine's potent electron-withdrawing effect. These substitutions maintained the planarity of the molecular structure with minimal bond length alterations. Chlorine and bromine substitutions at the outer positions led to longer C–X bonds due to their larger atomic sizes and lower electronegativities. Despite these variations, the outer substitutions generally preserved the planarity of the central phenyl ring, with steric hindrance being less pronounced than in inner substitutions.

The investigation into EDGs and EWGs at the outer positions demonstrated that these substituents generally maintained the planarity of the Blatter tri-radical core. EWGs such as  $\text{NO}_2$  and  $\text{COOH}$  preserved full planarity, with all atoms participating in the planar system. EDGs like  $\text{NH}_2$  and  $\text{CH}_3$  induced minor deviations, but the core structure remained largely unaffected.

The examination of the D–Q energy gaps for outer substitutions revealed that EWGs led to larger D–Q gaps, stabilising the quartet state by pulling electron density away from the radical centres. Halogenated substituents at the outer positions also tended to favour the quartet state, with lighter halogens like fluorine and chlorine showing larger gaps compared to heavier halogens like bromine. EDGs at the outer positions reduced the D–Q gap, indicating a more balanced stability between the doublet and quartet states.

For inner substitutions, the structural impact was more pronounced due to increased steric hindrance. Halogen substitutions at the inner positions resulted in longer bond lengths and greater structural distortions, particularly with larger halogens like bromine. Fluorine substitutions at inner positions maintained the planarity of the central phenyl ring, but steric interactions caused the outer phenyl rings to twist out of the plane, forming a crown-like structure. Chlorine and bromine substitutions introduced significant steric hindrance, leading to pronounced rotational distortions and loss of planarity.

EDGs and EWGs at inner positions had varied effects. EDGs such as  $\text{NH}_2$  and  $\text{N}(\text{Me})_2$  induced significant deviations due to steric effects. The  $\text{NH}_2$  group formed a unique honeycomb structure through hydrogen bonding, preserving some planarity despite out-of-plane deviations from terminal Ph rings.  $\text{N}(\text{Me})_2$  caused considerable out-of-plane deviations due to steric hindrance from the Me groups. EWGs like  $\text{COOH}$  and  $\text{CHO}$  maintained planarity in the central phenyl ring but induced greater out-of-plane distortions due to the orientation of their functional groups.

The examination of the D–Q energy gaps for inner substitutions highlighted that steric effects played a significant role in reducing the energy gaps. Inner substitutions generally exhibited smaller D–Q gaps compared to outer substitutions. Halogenated substituents at inner positions, despite their electronegative properties, showed relatively small gaps due to steric hindrance

reducing electronic interactions in the inner systems. EWGs at inner positions continued to lead to larger D–Q gaps, but the effects were less pronounced than in outer substitutions. EDGs at inner positions could destabilise the system, with NH<sub>2</sub> showing a negative gap, indicating a preference for the doublet state.

The computational methods revealed that the choice of functional significantly affected the predicted D–Q gaps. Using different functionals for geometry optimisation and energy calculations introduced inconsistencies. The PBE0 functional, despite slightly overestimating the D–Q gaps, provided consistent results when used for both geometry optimisation and energy calculations, reinforcing its reliability for the tri-radical calculations.

The study of fused dithiazole-triazine systems showed that the position and nature of heteroatoms significantly influenced the S–T energy gaps. Sulphur-containing configurations exhibited a strong preference for the singlet state. Phosphorus substitutions reduced the singlet–triplet gaps, highlighting the impact of phosphorus's larger atomic size and lower electronegativity on singlet stability. Selenium substitutions generally preserved the singlet state preference with minor variations dependent on the structural context. Therefore, all these systems exhibit closed-shell singlet ground states and cannot be classified as diradicals.

Functional group additions, such as CN and methoxy OCH<sub>3</sub> groups, demonstrated that EWGs enhanced singlet stability, especially in nitrogen-rich configurations. The OCH<sub>3</sub> group, while generally reinforcing singlet state stability, exhibited complex interactions influenced by the specific molecular context. Thus, substituting the H atom with these groups does not appear sufficient to induce diradical character in the fused rings, leaving the aza-acene (**29**) and the Blatter-type Schatz diradical (**30**) as the only systems with open-shell character among **26–30**.

In conclusion, this work provided key information into how outer and inner substitutions affected the structural and electronic properties of Blatter-type tri-radicals. The findings

established critical design principles for developing high-spin organic materials, highlighting the substantial influence of steric and electronic factors on spin-state stability. These results contribute to the fundamental understanding necessary for the rational design of advanced magnetic and spintronic devices.

Building upon the findings of this study, several avenues for future research are suggested to further advance the understanding and application of Blatter-type tri-radicals and related systems.

**Extended Computational Studies with Multireference Methods.** Performing additional calculations using multireference methods such as NEVPT2/CASSCF, including those with larger active spaces, is recommended. This approach would provide more accurate energy gap estimations and help validate the trends observed with DFT calculations, particularly for systems exhibiting anomalous behaviour.

**Investigation of Spin Density Distributions.** A detailed analysis of spin density distributions in both doublet and quartet states could provide deeper insights into the electronic factors contributing to spin-state preferences. Understanding how substituents affect spin delocalisation and localisation could aid in designing molecules with desired magnetic properties.

**Design of Functional Materials for Spintronic Applications.** Using the understanding of substituent effects on spin-state stability, future work could focus on designing functional materials suitable for spintronic applications. This may include incorporating Blatter-type radicals into conductive frameworks or exploring their behaviour in thin films and devices.

**Investigation of Steric Effects in Greater Detail.** Since steric factors play a significant role in influencing the electronic properties, a systematic study varying substituent sizes and positions could provide more comprehensive insights. Computational quantum chemistry

methods could be complemented with molecular mechanics or dynamics simulations to assess conformational flexibility and its impact on electronic structure.

**Alternative Heteroatom Substitutions.** Extending the study to include other heteroatoms, such as oxygen or heavier chalcogens, could reveal additional trends and opportunities for tuning electronic properties. Investigating how these substitutions affect molecular geometry and spin-state preferences would broaden the scope of potential applications.

# Chapter

## 5. References

- 1 I. Žutić, J. Fabian and S. Das Sarma, *Rev Mod Phys*, 2004, **76**, 323–410.
- 2 Nevill Francis Mott, *Proc R Soc Lond A Math Phys Sci*, 1936, **153**, 699–717.
- 3 E. Saitoh, M. Ueda, H. Miyajima and G. Tatara, *Appl Phys Lett*, 2006, **88**, 182509.
- 4 A. Privitera, M. Righetto, F. Cacialli and M. K. Riede, *Adv Opt Mater*, 2021, **9**, 2100215.
- 5 E. I. Rashba, *Phys Rev B*, 2000, **62**, R16267–R16270.
- 6 R. Meservey and P. M. Tedrow, *Phys Rep*, 1994, **238**, 173–243.
- 7 Y. Tserkovnyak, A. Brataas and G. E. W. Bauer, *Phys Rev Lett*, 2002, **88**, 117601.
- 8 H. Liu, C. Zhang, H. Malissa, M. Groesbeck, M. Kavand, R. McLaughlin, S. Jamali, J. Hao, D. Sun, R. A. Davidson, L. Wojcik, J. S. Miller, C. Boehme and Z. V. Vardeny, *Nat Mater*, 2018, **17**, 308–312.
- 9 S. Sanvito, *Nat Mater*, 2007, **6**, 803–804.
- 10 D. Sun, E. Ehrenfreund and Z. V. Vardeny, *Chem Commun*, 2014, **50**, 1781–1793.
- 11 H. Jang and C. A. Richter, *Advanced Materials*, 2017, **29**, 1602739.

- 12 K. Ando, S. Watanabe, S. Mooser, E. Saitoh and H. Sirringhaus, *Nat Mater*, 2013, **12**, 622–627.
- 13 D. Sun, K. J. van Schooten, M. Kavand, H. Malissa, C. Zhang, M. Groesbeck, C. Boehme and Z. V. Vardeny, *Nat Mater*, 2016, **15**, 863–869.
- 14 T. D. Nguyen, G. Hukic-Markosian, F. Wang, L. Wojcik, X.-G. Li, E. Ehrenfreund and Z. V. Vardeny, *Nat Mater*, 2010, **9**, 345–352.
- 15 M. Cinchetti, K. Heimer, J.-P. Wüstenberg, O. Andreyev, M. Bauer, S. Lach, C. Ziegler, Y. Gao and M. Aeschlimann, *Nat Mater*, 2009, **8**, 115–119.
- 16 P. Bakule and E. Morenzoni, *Contemp Phys*, 2004, **45**, 203–225.
- 17 T. Prokscha, E. Morenzoni, K. Deiters, F. Foroughi, D. George, R. Kobler, A. Suter and V. Vrankovic, *Physica B Condens Matter*, 2006, **374–375**, 460–463.
- 18 A. J. Drew, J. Hoppler, L. Schulz, F. L. Pratt, P. Desai, P. Shakya, T. Kreouzis, W. P. Gillin, A. Suter, N. A. Morley, V. K. Malik, A. Dubroka, K. W. Kim, H. Bouyanfif, F. Bourqui, C. Bernhard, R. Scheuermann, G. J. Nieuwenhuys, T. Prokscha and E. Morenzoni, *Nat Mater*, 2009, **8**, 109–114.
- 19 M. N. Baibich, J. M. Broto, A. Fert, F. N. Van Dau, F. Petroff, P. Etienne, G. Creuzet, A. Friederich and J. Chazelas, *Phys Rev Lett*, 1988, **61**, 2472–2475.
- 20 G. Binasch, P. Grünberg, F. Saurenbach and W. Zinn, *Phys Rev B*, 1989, **39**, 4828–4830.
- 21 D. Samal and P. S. Anil Kumar, *Resonance*, 2008, **13**, 343–354.
- 22 S. M. Yakout, *J Supercond Nov Magn*, 2020, **33**, 2557–2580.
- 23 A. Clements, *Computer Organization and Architecture: Themes and Variations Cengage Learning*, Global Engineering, Stamford, 2014.



- 24 S. M. Yakout, *J Supercond Nov Magn*, 2020, **33**, 2557–2580.
- 25 K. Dumesnil and S. Andrieu, in *Molecular Beam Epitaxy*, Elsevier, 2013, 487–507.
- 26 R. Weiss, R. Mattheis and G. Reiss, *Meas Sci Technol*, 2013, **24**, 082001.
- 27 J. Ferrer and V. M. García-Suárez, *J Mater Chem*, 2009, **19**, 1696.
- 28 K. D. Sattler, Ed., *Handbook of Nanophysics*, CRC Press, 2010.
- 29 S. Bhatti, R. Sbiaa, A. Hirohata, H. Ohno, S. Fukami and S. N. Piramanayagam, *Materials Today*, 2017, **20**, 530–548.
- 30 P. P. Power, *Chem Rev*, 2003, **103**, 789–810.
- 31 A. Caneschi, D. Gatteschi and P. Rey, in *Progress in Inorganic Chemistry*, ed. S. J. Lippard, John Wiley & Sons, New York, 1991, 331–429.
- 32 S. Sowndarya S. V., P. C. St. John and R. S. Paton, *Chem Sci*, 2021, **12**, 13158–13166.
- 33 A. Vasiļevska and T. Slanina, *Chem Commun*, 2024, **60**, 252–264.
- 34 I. Ratera, J. Vidal-Gancedo, D. MasPOCH, S. T. Bromley, N. Crivillers and M. Mas-Torrent, *J Mater Chem C*, 2021, **9**, 10610–10623.
- 35 O. Armet, J. Veciana, C. Rovira, J. Riera, J. Castaner, E. Molins, J. Rius, C. Miravittles, S. Olivella and J. Brichfeus, *J Phys Chem*, 1987, **91**, 5608–5616.
- 36 M. Gomberg, *J Am Chem Soc*, 1900, **22**, 757–771.
- 37 I. Ratera and J. Veciana, *Chem Soc Rev*, 2012, **41**, 303–349.
- 38 Z. Zhou and L. Liu, *Curr Org Chem*, 2014, **18**, 459–474.
- 39 M. Deumal, P. Lafuente, F. Mota and J. J. Novoa, *Synth Met*, 2001, **122**, 477–483.
- 40 T. Kubo, *Molecules*, 2019, **24**, 665.

- 41 P. A. Koutentis and D. Lo Re, *Synthesis*, 2010, 2075–2079.
- 42 D. Sun, E. Ehrenfreund and Z. V. Vardeny, *Chem Commun*, 2014, **50**, 1781–1793.
- 43 S. Reineke, F. Lindner, G. Schwartz, N. Seidler, K. Walzer, B. Lüssem and K. Leo, *Nature*, 2009, **459**, 234–238.
- 44 O. Ostroverkhova, *Chem Rev*, 2016, **116**, 13279–13412.
- 45 H. Sirringhaus, *Adv Mat*, 2014, **26**, 1319–1335.
- 46 A. Privitera, R. Warren, G. Londi, P. Kaienburg, J. Liu, A. Sperlich, A. E. Lauritzen, O. Thimm, A. Ardavan, D. Beljonne and M. Riede, *J Mater Chem C*, 2021, **9**, 2944–2954.
- 47 A. Troisi, *Chem Soc Rev*, 2011, **40**, 2347.
- 48 D. L. Cheung and A. Troisi, *Phys Chem Chem Phys*, 2008, **10**, 5941.
- 49 L. Guo, Y. Qin, X. Gu, X. Zhu, Q. Zhou and X. Sun, *Front Chem*, 2019, **7**, 428.
- 50 S.-J. Wang, D. Venkateshvaran, M. R. Mahani, U. Chopra, E. R. McNellis, R. Di Pietro, S. Schott, A. Wittmann, G. Schweicher, M. Cubukcu, K. Kang, R. Carey, T. J. Wagner, J. N. M. Siebrecht, D. P. G. H. Wong, I. E. Jacobs, R. O. Aboljadayel, A. Ionescu, S. A. Egorov, S. Mueller, O. Zadvorna, P. Skalski, C. Jellett, M. Little, A. Marks, I. McCulloch, J. Wunderlich, J. Sinova and H. Sirringhaus, *Nat Electron*, 2019, **2**, 98–107.
- 51 V. A. Dediu, L. E. Hueso, I. Bergenti and C. Taliani, *Nat Mater*, 2009, **8**, 850–850.
- 52 Z. G. Yu, F. Ding and H. Wang, *Phys Rev B*, 2013, **87**, 205446.
- 53 H. M. Blatter and H. Lukaszewski, *Tetrahedron Lett*, 1968, **9**, 2701–2705.
- 54 C. P. Constantinides, A. A. Berezin, M. Manoli, G. M. Leitus, G. A. Zissimou, M. Bendikov, J. M. Rawson and P. A. Koutentis, *Chem Eur J*, 2014, **20**, 5388–5396.

- 55 C. P. Constantinides, A. A. Berezin, G. A. Zissimou, M. Manoli, G. M. Leitus, M. Bendikov, M. R. Probert, J. M. Rawson and P. A. Koutentis, *J Am Chem Soc*, 2014, **136**, 11906–11909.
- 56 F. A. Neugebauer and I. Umminger, *Chem Ber*, 1981, **114**, 2423–2430.
- 57 A. Bodzioch, M. Zheng, P. Kaszyński and G. Utecht, *J Org Chem*, 2014, **79**, 7294–7310.
- 58 Y. Ji, L. Long and Y. Zheng, *Mater Chem Front*, 2020, **4**, 3433–3443.
- 59 C. P. Constantinides, P. A. Koutentis and J. M. Rawson, *Chem Eur J*, 2012, **18**, 15433–15438.
- 60 C. P. Constantinides, P. A. Koutentis, H. Krassos, J. M. Rawson and A. J. Tasiopoulos, *J Org Chem*, 2011, **76**, 2798–2806.
- 61 C. P. Constantinides, A. A. Berezin, G. A. Zissimou, M. Manoli, G. M. Leitus, M. Bendikov, M. R. Probert, J. M. Rawson and P. A. Koutentis, *J Am Chem Soc*, 2014, **136**, 11906–11909.
- 62 B. Yan, J. Cramen, R. McDonald and N. L. Frank, *Chem Commun*, 2011, **47**, 3201.
- 63 C. Constantinides, A. Berezin, G. Zissimou, M. Manoli, G. Leitus and P. Koutentis, *Molecules*, 2016, **21**, 636.
- 64 A. A. Berezin, G. Zissimou, C. P. Constantinides, Y. Beldjoudi, J. M. Rawson and P. A. Koutentis, *J Org Chem*, 2014, **79**, 314–327.
- 65 J. A. Grant, Z. Lu, D. E. Tucker, B. M. Hockin, D. S. Yufit, M. A. Fox, R. Katakya, V. Chechik and A. C. O'Donoghue, *Nat Commun*, 2017, **8**, 15088.
- 66 F. A. Neugebauer and I. Umminger, *Chem Ber*, 1980, **113**, 1205–1225.
- 67 F. A. Neugebauer and I. Umminger, *Chem Ber*, 1981, **114**, 2423–2430.

- 68 G. A. Zissimou, A. A. Berezin, M. Manoli, C. Nicolaides, T. Trypiniotis and P. A. Koutentis, *Tetrahedron*, 2020, **76**, 131077.
- 69 P. Kaszyński, C. P. Constantinides and V. G. Young, *Angew Chem Int Ed*, 2016, **55**, 11149–11152.
- 70 A. C. Savva, S. I. Mirallai, G. A. Zissimou, A. A. Berezin, M. Demetriades, A. Kourtellaris, C. P. Constantinides, C. Nicolaides, T. Trypiniotis and P. A. Koutentis, *J Org Chem*, 2017, **82**, 7564–7575.
- 71 G. A. Zissimou, A. A. Berezin, M. Manoli, C. Nicolaides, T. Trypiniotis and P. A. Koutentis, *Tetrahedron*, 2020, **76**, 131077.
- 72 G. A. Zissimou, A. A. Berezin, M. Manoli, C. Nicolaides, T. Trypiniotis and P. A. Koutentis, *Tetrahedron*, 2020, **76**, 131077.
- 73 F. A. Neugebauer and I. Umminger, *Chem Ber*, 1981, **114**, 2423–2430.
- 74 P. Kaszyński, C. P. Constantinides and V. G. Young, *Angew Chem Int Ed*, 2016, **55**, 11149–11152.
- 75 G. Karecla, P. Papagiorgis, N. Panagi, G. A. Zissimou, C. P. Constantinides, P. A. Koutentis, G. Itskos and S. C. Hayes, *New J Chem*, 2017, **41**, 8604–8613.
- 76 N. M. Gallagher, A. Olankitwanit and A. Rajca, *J Org Chem*, 2015, **80**, 1291–1298.
- 77 A. Hirohata, K. Yamada, Y. Nakatani, I.-L. Prejbeanu, B. Diény, P. Pirro and B. Hillebrands, *J Magn Magn Mater*, 2020, **509**, 166711.
- 78 Y. Zheng, M. Miao, G. Dantelle, N. D. Eisenmenger, G. Wu, I. Yavuz, M. L. Chabinyč, K. N. Houk and F. Wudl, *Adv Mat*, 2015, **27**, 1718–1723.

- 79 Y. Zhang, Y. Zheng, H. Zhou, M. Miao, F. Wudl and T. Nguyen, *Adv Mat*, 2015, **27**, 7412–7419.
- 80 J. Z. Low, G. Kladnik, L. L. Patera, S. Sokolov, G. Lovat, E. Kumarasamy, J. Repp, L. M. Campos, D. Cvetko, A. Morgante and L. Venkataraman, *Nano Lett*, 2019, **19**, 2543–2548.
- 81 L. L. Patera, S. Sokolov, J. Z. Low, L. M. Campos, L. Venkataraman and J. Repp, *Angew Chem Int Ed*, 2019, **58**, 11063–11067.
- 82 M. Jasiński, J. Szczytko, D. Pocięcha, H. Monobe and P. Kaszyński, *J Am Chem Soc*, 2016, **138**, 9421–9424.
- 83 L.-A. Keane, S. Mirallai, M. Sweeney, M. Carty, G. Zissimou, A. Berezin, P. Koutentis and F. Aldabbagh, *Molecules*, 2018, **23**, 574.
- 84 Y. Zheng, M. Miao, M. C. Kemei, R. Seshadri and F. Wudl, *Isr J Chem*, 2014, **54**, 774–778.
- 85 F. Ciccullo, N. M. Gallagher, O. Geladari, T. Chassé, A. Rajca and M. B. Casu, *ACS Appl Mater Interfaces*, 2016, **8**, 1805–1812.
- 86 C. Di, F. Zhang and D. Zhu, *Adv Mat*, 2013, **25**, 313–330.
- 87 S. Majumdar, H. S. Majumdar, R. Laiho and R. Österbacka, *J Alloys Compd*, 2006, **423**, 169–171.
- 88 T. D. Nguyen, G. Hukic-Markosian, F. Wang, L. Wojcik, X.-G. Li, E. Ehrenfreund and Z. V. Vardeny, *Synth Met*, 2011, **161**, 598–603.
- 89 C. P. Constantinides, P. A. Koutentis and J. Schatz, *J Am Chem Soc*, 2004, **126**, 16232–16241.

- 90 G. A. Zissimou, A. A. Berezin, M. Manoli, C. Nicolaides, T. Trypiniotis and P. A. Koutentis, *Tetrahedron*, 2020, **76**, 131077.
- 91 R. Khurana, A. Bajaj, K. R. Shamasundar and Md. E. Ali, *J Phys Chem A*, 2023, **127**, 7802–7810.
- 92 H. Eschrig, *The Fundamentals of Density Functional Theory*, Vieweg+Teubner Verlag, Wiesbaden, 1996, **32**.
- 93 P. Hohenberg and W. Kohn, *Phys Rev*, 1964, **136**, B864–B871.
- 94 W. Kohn and L. J. Sham, *Phys Rev*, 1965, **140**, A1133–A1138.
- 95 R. G. Parr and Y. Weitao, *Density-Functional Theory of Atoms and Molecules*, Oxford University Press, 1995.
- 96 M. Born and R. Oppenheimer, *Ann Phys*, 1927, **389**, 457–484.
- 97 N. Mardirossian and M. Head-Gordon, *Mol Phys*, 2017, **115**, 2315–2372.
- 98 L. H. Thomas, *Mathematical Proceedings of the Cambridge Philosophical Society*, 1927, **23**, 542–548.
- 99 Y. A. Wang, N. Govind and E. A. Carter, *Phys Rev B*, 1999, **60**, 16350–16358.
- 100 W. Zhou and S. Yuan, *Chin. Phys Lett*, 2023, **40**, 027101.
- 101 J. Xia, C. Huang, I. Shin and E. A. Carter, *J Chem Phys*, 2012, **136**, 084102.
- 102 J. P. Perdew, A. Ruzsinszky, J. Tao, V. N. Staroverov, G. E. Scuseria and G. I. Csonka, *J Chem Phys*, 2005, **123**, 062201.
- 103 In *The Holy Bible: New International Version, Genesis 28:10-17*, Hodder and Stoughton, 1979.

- 104 J. P. Perdew, K. Burke and M. Ernzerhof, *Phys Rev Lett*, 1996, **77**, 3865–3868.
- 105 A. J. Cohen, P. Mori-Sánchez and W. Yang, *Chem Rev*, 2012, **112**, 289–320.
- 106 F. Herman, J. P. Van Dyke and I. B. Ortenburger, *Phys Rev Lett*, 1969, **22**, 807–811.
- 107 O. V. Gritsenko, P. R. T. Schipper and E. J. Baerends, *Chem Phys Lett*, 1999, **302**, 199–207.
- 108 A. D. Becke, *J Chem Phys*, 1986, **84**, 4524–4529.
- 109 A. D. Becke, *J Chem Phys*, 1997, **107**, 8554–8560.
- 110 H. L. Schmider and A. D. Becke, *J Chem Phys*, 2002, **116**, 3184–3193.
- 111 N. Mardirossian and M. Head-Gordon, *Mol Phys*, 2017, **115**, 2315–2372.
- 112 Y. Zhao and D. G. Truhlar, *Acc Chem Res*, 2008, **41**, 157–167.
- 113 L. Goerigk and S. Grimme, *Phys Chem Chem Phys*, 2011, **13**, 6670.
- 114 A. D. Becke, *J Chem Phys*, 1992, **96**, 2155–2160.
- 115 S. H. Vosko, L. Wilk and M. Nusair, *Can J Phys*, 1980, **58**, 1200–1211.
- 116 C. Adamo and V. Barone, *J Chem Phys*, 1999, **110**, 6158–6170.
- 117 A. J. Cohen, P. Mori-Sánchez and W. Yang, *Science*, 2008, **321**, 792–794.
- 118 S. Grimme, *J Chem Phys*, 2006, **124**, 034108.
- 119 A. D. Becke, *J Chem Phys*, 1993, **98**, 5648–5652.
- 120 R. Peverati and D. G. Truhlar, *Philos Trans A Math Phys Eng Sci*, 2014, **372**, 20120476.
- 121 S. Grimme, *WIREs Comput Mol Sci*, 2011, **1**, 211–228.
- 122 J. Hermann, R. A. DiStasio and A. Tkatchenko, *Chem Rev*, 2017, **117**, 4714–4758.

- 123 F. Tran, P. Blaha and K. Schwarz, *J. Phys. Condens. Matter*, 2007, **19**, 196208.
- 124 S. Grimme, *J Comput Chem*, 2004, **25**, 1463–1473.
- 125 S. Grimme, J. Antony, S. Ehrlich and H. Krieg, *J Chem Phys*, 2010, **132**, 154104.
- 126 P. R. Surján, *Second quantized approach to quantum chemistry: an elementary introduction*, Springer Science & Business Media, 2012.
- 127 Y. Shao, M. Head-Gordon and A. I. Krylov, *J Chem Phys*, 2003, **118**, 4807–4818.
- 128 M. J. Frisch, G. W. Trucks, H. B. Schlegel, G. E. Scuseria, M. A. Robb, J. R. Cheeseman, G. Scalmani, V. Barone, B. Mennucci, G. A. Petersson, H. Nakatsuji, M. Caricato, X. Li, H. P. Hratchian, A. F. Izmaylov, J. Bloino, G. Zheng, J. L. Sonnenberg, M. Hada, M. Ehara, K. Toyota, R. Fukuda, J. Hasegawa, M. Ishida, T. Nakajima, Y. Honda, O. Kitao, H. Nakai, T. Vreven, J. A. Montgomery Jr., J. E. Peralta, F. Ogliaro, M. Bearpark, J. J. Heyd, E. Brothers, K. N. Kudin, V. N. Staroverov, R. Kobayashi, J. Normand, K. Raghavachari, A. Rendell, J. C. Burant, S. S. Iyengar, J. Tomasi, M. Cossi, N. Rega, J. M. Millam, M. Klene, J. E. Knox, J. B. Cross, V. Bakken, C. Adamo, J. Jaramillo, R. Gomperts, R. E. Stratmann, O. Yazyev, A. J. Austin, R. Cammi, C. Pomelli, J. W. Ochterski, R. L. Martin, K. Morokuma, V. G. Zakrzewski, G. A. Voth, P. Salvador, J. J. Dannenberg, S. Dapprich, A. D. Daniels, Ö. Farkas, J. B. Foresman, J. V. Ortiz, J. Cioslowski and D. J. Fox, *Gaussian 16, Revision C.01*, Gaussian, Inc., Wallingford CT, 2016.
- 129 G. D. Purvis and R. J. Bartlett, *J Chem Phys*, 1982, **76**, 1910–1918.
- 130 K. Raghavachari, G. W. Trucks, J. A. Pople and M. Head-Gordon, *Chem Phys Lett*, 1989, **157**, 479–483.
- 131 T. Van Voorhis and M. Head-Gordon, *J Chem Phys*, 2001, **115**, 5033–5040.



- 132 Chr. Møller and M. S. Plesset, *Phys Rev*, 1934, **46**, 618–622.
- 133 E. Schrödinger, *Ann Phys*, 1926, **384**, 489–527.
- 134 P. E. M. Siegbahn, J. Almlöf, A. Heiberg and B. O. Roos, *J Chem Phys*, 1981, **74**, 2384–2396.
- 135 D.-K. Dang and P. M. Zimmerman, *J Chem Phys*, 2021, **154**, 014105.
- 136 Y. Guo, K. Sivalingam and F. Neese, *J Chem Phys*, 2021, **154**, 214111.
- 137 F. Neese, *WIREs Comput Mol Sci*, 2012, **2**, 73–78.
- 138 F. Neese, *WIREs Comput Mol Sci*, 2022, **12**, e1606.
- 139 Y. Guo, K. Sivalingam, E. F. Valeev and F. Neese, *J Chem Phys*, 2016, **144**, 094111.
- 140 F. Neese, *J Comput Chem*, 2003, **24**, 1740–1747.
- 141 F. Neese, F. Wennmohs, A. Hansen and U. Becker, *Chem Phys*, 2009, **356**, 98–109.
- 142 A. V. Marenich, C. J. Cramer and D. G. Truhlar, *J Phys Chem B*, 2009, **113**, 6378–6396.
- 143 E. Cancès, B. Mennucci and J. Tomasi, *J Chem Phys*, 1997, **107**, 3032–3041.
- 144 Chemcraft team, Chemcraft – Graphical software for visualization of quantum chemistry computations.
- 145 S. bin Uzayr, *Mastering Visual Studio Code*, CRC Press, Boca Raton, 2022.
- 146 Y. Zhao and D. G. Truhlar, *J Phys Chem A*, 2005, **109**, 5656–5667.
- 147 Y. Zhao and D. G. Truhlar, *Theor Chem Acc*, 2008, **120**, 215–241.
- 148 R. Beiranvand, *Mater Sci Semicond Process*, 2021, **135**, 106092.
- 149 C. Adamo and V. Barone, *J Chem Phys*, 1999, **110**, 6158–6170.

- 150 V. Tognetti and C. Adamo, *J Phys Chem A*, 2009, **113**, 14415–14419.
- 151 A. J. Cohen and N. C. Handy, *Mol Phys*, 2001, **99**, 607–615.
- 152 J.-D. Chai and M. Head-Gordon, *Phys Chem Chem Phys*, 2008, **10**, 6615.
- 153 Y. Zhao and D. G. Truhlar, *J Phys Chem A*, 2006, **110**, 5121–5129.
- 154 H. S. Yu, X. He, S. L. Li and D. G. Truhlar, *Chem Sci*, 2016, **7**, 5032–5051.
- 155 J. Tao, J. P. Perdew, V. N. Staroverov and G. E. Scuseria, *Phys Rev Lett*, 2003, **91**, 146401.
- 156 H. S. Yu, X. He, S. L. Li and D. G. Truhlar, *Chem Sci*, 2016, **7**, 5032–5051.
- 157 C. Lee, W. Yang and R. G. Parr, *Phys Rev B*, 1988, **37**, 785–789.
- 158 J.-D. Chai and M. Head-Gordon, *Phys Chem Chem Phys*, 2008, **10**, 6615.
- 159 J. P. Perdew, J. Tao, V. N. Staroverov and G. E. Scuseria, *J Chem Phys*, 2004, **120**, 6898–6911.
- 160 V. N. Staroverov, G. E. Scuseria, J. Tao and J. P. Perdew, *J Chem Phys*, 2003, **119**, 12129–12137.
- 161 J. Tao, J. P. Perdew, V. N. Staroverov and G. E. Scuseria, *Phys Rev Lett*, 2003, **91**, 146401.
- 162 F. Weigend and R. Ahlrichs, *Phys Chem Chem Phys*, 2005, **7**, 3297.
- 163 F. Weigend, *Phys Chem Chem Phys*, 2006, **8**, 1057.
- 164 B. P. Pritchard, D. Altarawy, B. Didier, T. D. Gibson and T. L. Windus, *J Chem Inf Model*, 2019, **59**, 4814–4820.
- 165 C. R. Groom, I. J. Bruno, M. P. Lightfoot and S. C. Ward, *Acta Crystallogr B Struct Sci Cryst Eng Mater*, 2016, **72**, 171–179.